The Effect of Hub Configuration on the Performance of an Air-Cooled Steam Condenser Fan

by

Zander Meiring

Thesis presented in partial fulfilment of the requirements for the degree of Master of Engineering (Mechanical) in the Faculty of Engineering at Stellenbosch University

Supervisor: Prof. S.J. Van der Spuy
Co-supervisor: Prof. C.J. Meyer

March 2020

Stellenbosch University https://scholar.sun.ac.za

Declaration

By submitting this thesis electronically, I declare that the entirety of the work contained therein is my own, original work, that I am the sole author thereof (save to the extent explicitly otherwise stated), that reproduction and publication thereof by Stellenbosch University will not infringe any third party rights and that I have not previously in its entirety or in part submitted it for obtaining any qualification.

Date: March 2020

Copyright © 2020 Stellenbosch University
All rights reserved.

Stellenbosch University https://scholar.sun.ac.za

Abstract

The Effect of Hub Configuration on the Performance of an Air-Cooled Steam Condenser Fan

Z. Meiring

Department of Mechanical and Mechatronic Engineering,
University of Stellenbosch,
Private Bag X1, 7602 Matieland, South Africa.

Thesis: MEng (Mech)

March 2020

Axial flow fans used in air-cooled condensers are typically analysed with smooth rounded hubs due to their superior performance. However, such a hub increases the manufacturing and installation costs of air-cooled condensers. As such, it is desirable to use a simpler hub geometry to reduce the total installation cost.

This thesis assesses the impact that a simpler hub configuration may have on the performance of an axial flow fan. This is done through a comparison of four hub configurations: a round hub, a square hub, and two disk hubs. Computational fluid dynamics modelling utilizing the open-source software code, OpenFOAM, is used to simulate each hub configuration. BlockMesh is used to generate the computational mesh required.

It is found that the impact on performance due to hub geometry is dependent on the volumetric flow rate through the fan. At above design point flow rates, the square hub configuration has the best performance, providing a 9.5 % increase in total-to-static pressure rise and a 5.1 % point improvement in total-to-static efficiency compared to the round hub. On the other hand, a centre disk hub provides a 8.4 % improvement in total-to-static pressure rise and a 5.7 % point improvement in total-to-static efficiency when compared to the round hub at 62.5 % of the design flow rate. At the design point flow rate the round and square hubs result in a very similar performance, and superior to the disk hub configurations.

Stellenbosch University https://scholar.sun.ac.za

Uittreksel

Die Effek van Naafkonfigurasie op die Werkverrigting van 'n Lugverkoelde Stoom-Kondensor Verkoelingswaaier

Z. Meiring

Departement Meganiese en Megatroniese Ingenieurswese,
Universiteit van Stellenbosch,
Privaatsak X1, 7602 Matieland, Suid Afrika.

Tesis: MIng (Meg)

Maart 2020

Aksialvloeiwaaiers wat gebruik word in lugverkoelde stoom-kondensors word tipies ontleed met 'n gladde geronde naaf weens beter werkverrigting van hierdie konfigurasie. So 'n naaf verhoog egter die koste van vervaardiging en installasie van die verkoelingswaaier. As sulks, is dit wenslik om 'n meer eenvoudige naaf konfigurasie te gebruik om die totale prys van installasie te verminder.

Hierdie tesis evalueer die impak op werkverrigting van 'n verkoelingswaaier met 'n meer eenvoudige naafkonfigurasie. Dit is gedoen deur 'n vergelyking van vier naafkonfigurasies: 'n ronde naaf, 'n boks naaf, en twee skyf nawe. Berekenings vloeimeganika modellering, met behulp van die oopbronsagteware OpenFOAM, word gebruik om elke naaf te simuleer. BlockMesh word gebruik om die rooster te bou.

Daar word gevind dat die impak op die werkverrigting as gevolg van die naafkonfigurasie afhanklik is van die volumetriese vloeitempo deur die waaier. By bo-ontwerp punt volumetriese vloeitempo besorg die boks naaf die beste werksverrigting met 'n styging van 9.5 % in totale-tot-statiese drukverhoging en 'n 5.1 % punt vehoging in totale-tot-statiese doeltreffendheid, in vergelyking met die ronde naaf. In kontras, bied die sentrale skyf naaf 'n 8.4 % verbetering in totale-tot-statiese drukverhooging en 'n 5.7 % punt verbetering in die totale-tot-statiese doeltreffendheid in vergelyking met die ronde naaf, by 62.5 % van

Stellenbosch University https://scholar.sun.ac.za

die ontwerpsvloeitempo. By die ontwerpsvloeitempo toon die ronde en boks naaf soortgelyk aan, en doen beter as die skyf nawe.

Stellenbosch University https://scholar.sun.ac.za

Acknowledgements

Firstly I would like to thank my parents, whom without I would not be here. It is their support that allows me to be where I am today, and I am very appreciative.

I would like to thank Lauren Palmer for her endless support. For listening to my unstructured thoughts about work, for proof reading multiple drafts, for taking care of food when a project deadline loomed in, and for her unconditional care.

To my colleagues and good friends T^2, Meyer and Ochabski. Even if our Neelsie missions are nearing the end, I am sure the banter will never stop. Their insightful advice and constant competitiveness kept me driven throughout this thesis.

Finally, to Prof. Van der Spuy and Prof. Meyer. For their constant support and advice throughout my thesis, even when things seemed to not be working out. I appreciate that not only did they support me with my technical work, but also with organisation of my bursary and access to the CHPC.

Stellenbosch University https://scholar.sun.ac.za

Contents

Stellenbosch University https://scholar.sun.ac.za

Stellenbosch University https://scholar.sun.ac.za

Stellenbosch University https://scholar.sun.ac.za

List of Figures

Stellenbosch University https://scholar.sun.ac.za

Stellenbosch University https://scholar.sun.ac.za

Stellenbosch University https://scholar.sun.ac.za

Stellenbosch University https://scholar.sun.ac.za

List of Tables

Stellenbosch University https://scholar.sun.ac.za

Nomenclature

Variables

A	Area	$[\mathrm{m}^2]$
C	Coefficient	$[-]$
ch	Chord length	$[\mathrm{m}]$
E	Extruded point	$[-]$
F	Force	$[\mathrm{N}]$
f	Force per unit length	$[\mathrm{N/m}]$
k	Turbulence kinetic energy per unit mass	$[\mathrm{J/kg}]$
l	Length	$[\mathrm{m}]$
N	Rotational speed, Normal	$[\mathrm{rev/min}, -]$
n	Number	$[-]$
P	Power, point	$[\mathrm{W}, -]$
p	Pressure	$[\mathrm{N/m}^2]$
R	Ratio of maximum and minimum cell sizes	$[-]$
R_p	Pearson correlation factor	$[-]$
r	Radius, ratio of adjacent cell sizes	$[\mathrm{m}, -]$
s	Span, entropy per unit mass	$[-, \mathrm{J/kg \cdot K}]$
T	Torque, temperature	$[\mathrm{N \cdot m}, \mathrm{K}]$
u	Blade tangential velocity	$[\mathrm{m/s}]$

Stellenbosch University https://scholar.sun.ac.za

$\dot{V}$	Volumetric flow rate	$[\mathrm{m}^3/\mathrm{s}]$
V	Absolute velocity	$[\mathrm{m/s}]$
W	Relative velocity	$[\mathrm{m/s}]$
x	Length along chord	$[\mathrm{m}]$
δx_s	Smallest cell size	$[-]$
δx_l	Largest cell size	$[-]$
y_1	First cell height	$[\mathrm{m}]$

Greek Symbols

α	Angle of attack, Constant of geometric progression	$[^\circ, -]$
β	Relative velocity angle	$[^\circ]$
ϵ	Turbulence dissipation rate	$[\mathrm{J/kg \cdot s}]$
η	Efficiency	$[-]$
θ	Angle	$[^\circ]$
μ	Dynamic viscosity	$[\mathrm{kg/m \cdot s}]$
ζ	Stagger angle	$[^\circ]$
ρ	Density	$[\mathrm{kg/m}^3]$
ν	Kinematic viscosity	$[\mathrm{Pa \cdot s}]$
ω	Rotational speed, Specific turbulence dissipation rate	$[\mathrm{rad/s}, 1/\mathrm{s}]$

Subscripts

avg	Average
b	Blade
d	Drag
f	Fan
h	Hub

Stellenbosch University https://scholar.sun.ac.za

i	Current number
$i+1$	Next number
$i-1$	Previous number
l	Lift
r	Polar coordinate r
s	Static
t	Total, tip
$R\ Hub$	Round hub
r	Rotor, relative
x	Cartesian coordinate x
y	Cartesian coordinate y
z	Cartesian, Polar coordinate z
θ	Polar coordinate θ
∞	Averaged through rotor region
1	Upstream
2	Downstream

Abbreviations

ACC Air-cooled condenser

ACHE Air-cooled heat exchanger

BSP Blade surface pressure

CFD Computational Fluid Dynamics

CSV Comma separated values

DNS Direct numerical simulation

DPIV Digital particle image velocimetry

FVI-ZGO Fixed value inflow, zero gradient outflow

Stellenbosch University https://scholar.sun.ac.za

LES Large eddy simulation

P3DM Periodic three-dimensional model

PISO Pressure implicit with splitting of operator

RANS Reynolds averaged Navier-Stokes

RMSD Root-mean-square difference

SIMPLE Semi-implicit method for pressure linked equations

Stellenbosch University https://scholar.sun.ac.za

Chapter 1

Introduction

1.1 Background

Air-cooled heat exchangers (ACHEs) are used to provide process cooling in a range of industries, including chemical processing and power generation. ACHEs offer advantages over alternative cooling methods, such as wet cooling and once-through cooling, by providing a significant reduction in water consumption (Kröger, 1998; Kohli and Frenken, 2011). This is, therefore, an attractive cooling method for technologies such as solar thermal power generation, as these facilities are often located in arid regions where lack of water is a significant factor.

The drawback of ACHEs is the reduction they cause in overall cycle efficiency. This is due to the poor thermal capacity of air, decreasing the cooling capacity of the condensation phase. To mitigate this, many large diameter axial flow fans are used to motivate the air over the heat exchangers. An example of this is Matimba power station, which makes use of 288 fan units with 9 m diameter fans powered by 270 kW electric motors (Kröger, 1998). Due to their number and scale, improvements to the efficiency of these axial flow fans will have a significant, positive impact on the efficiency of the entire cycle.

Figure 1.1b shows the composition of an ACHE fan. The fan consists of a set of fan blades attached to a hub. This hub is rotated by an electric motor via a gearbox. The fan and hub unit is encased in a shroud which is connected upstream to a rounded bellmouth. The bellmouth and hub both act to direct the flow smoothly to the fan blades, where the work on the fluid is imparted.

Stellenbosch University https://scholar.sun.ac.za

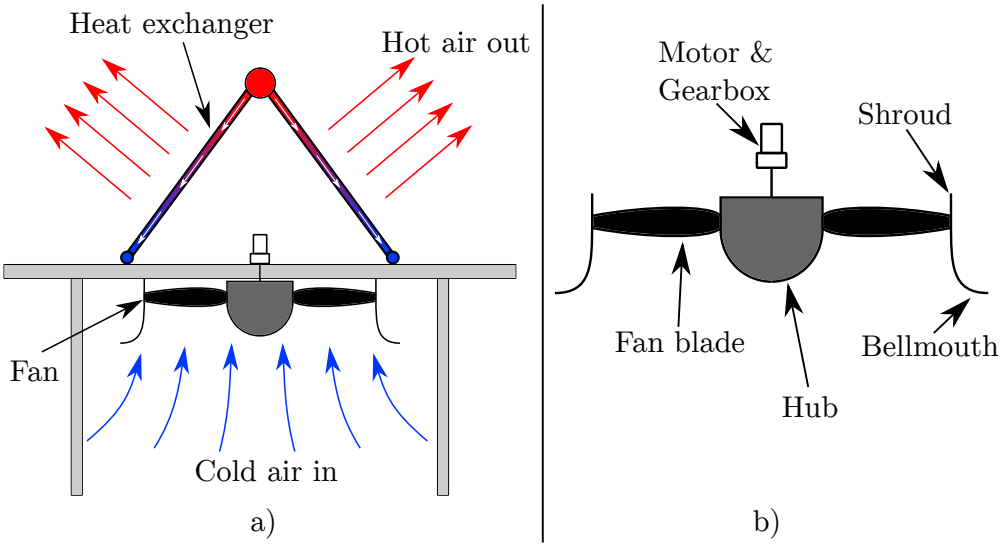

Figure 1.1: ACHE a) unit, b) fan

The hub is a much overlooked aspect of the fan assembly. Smooth, bulb-shaped hubs are often analysed due to the superior performance of fans using these hubs. These hubs are, however, difficult to manufacture and install on the scale of a typical ACHE unit (with fan diameters over 9 m). The aim of this thesis is to research the effect of using a simplified hub geometry that could reduce the capital cost and complexity of an ACHE fan unit. Simpler geometries would be preferred from both an economical and an ergonomic point of view. However, it is difficult to recommend simpler hub geometries without a proper understanding of the physics underlying their performance. As such, this thesis sets out to construct a computational fluid dynamics (CFD) model to investigate the associated fluid structures and the effect on performance that different hub configurations have on an axial flow fan.

1.2 Research Objectives

The objectives of this thesis are as follows:

1. **Investigate the effect of hub configuration on the performance of an ACHE fan.** Four different hub configurations are compared through assessment of their characteristic curves, flow visualisation, and averaged distribution of flow variables. This aims to present a clear and concise relationship between hub configuration and fan performance in order to provide additional information for ACHE fan design.

Stellenbosch University https://scholar.sun.ac.za

2. **Perform fluid simulation of an ACHE fan through use of open-source numerical modelling**. Open-source software allows for lower costs of flow simulations. By making use of and validating an open-source generated model, the prospect of using open-source software for numerical modelling is determined. As such, this thesis describes the generation of the fan numerical model in detail in order to aid future research.

1.3 Thesis Overview

An overview of the contents of this thesis is as follows:

- Chapter 2 identifies existing literature that gives insight to axial fan hubs and performance. An investigation of computational methods is performed in order to understand the needs to successfully model an axial flow fan.
- Chapter 3 discusses the shape and dimensions of the domain used. Based on this, a mesh is constructed. The construction of this mesh is described in detail.
- Chapter 4 describes the required setup in order to solve the Navier-Stokes equations. This composes of the boundary conditions, choice of solver, and discretization schemes. Lastly, a convergence criteria is set to define a solved simulation.
- Chapter 5 validates the model against existing experimental data. This is done through a comparison of the fan characteristic curves and blade surface pressure data.
- Chapter 6 discusses the results of all simulations performed between different hub configurations. This is accomplished by making use of characteristic curves, streamlines and contour plots, flow variable evaluation in and around the rotor region, and blade force and pressure distributions.
- Chapter 7 concludes the work by summarising the results discussed in Chapter 6 and identifying a link between axial flow fan performance and hub configuration. Recommendations are made for future work following from this research.

Stellenbosch University https://scholar.sun.ac.za

Chapter 2

Literature Study

Existing literature that relates to the thesis objectives are discussed below. First, the background of the fan to be modelled is presented. Then existing research into axial fan hubs is considered and their findings briefly discussed. Important phenomena at off-design conditions are considered. The literature study concludes with assessing modelling techniques for axial flow fans.

2.1 B2a Axial Flow Fan

Venter (1990) investigated the effects of flow distortion elements and design considerations for an air-cooled condenser (ACC) fan. Venter found that an increase in hub to tip ratio (from 0.15 to 0.289) lead to significant improvements in fan efficiency due to a reduction of reverse flow near the hub region. This lead to Bruneau (1994) designing the B1- and B2-fans in order to improve ACC fan performance. The B1-fan made use of the Clark-Y aerofoil while the B2-fan used the NASA LS series profile. Other than this, both fans were developed for the same low pressure rise and high flow rate requirements typical for a fan used in ACC applications, using a free-vortex design. Following from its introduction, the B2-fan was used in numerous academic investigations at Stellenbosch University.

Louw *et al.* (2012) improved the B2-fan by the design of the B2a-fan. The B2a-fan used the same basic profile, chord, and stagger values as the B2-fan. The profiles where changed to be wrapped around the hub as constant cylindrical cross-sections. This difference is highlighted in Figure 2.1.

Stellenbosch University https://scholar.sun.ac.za

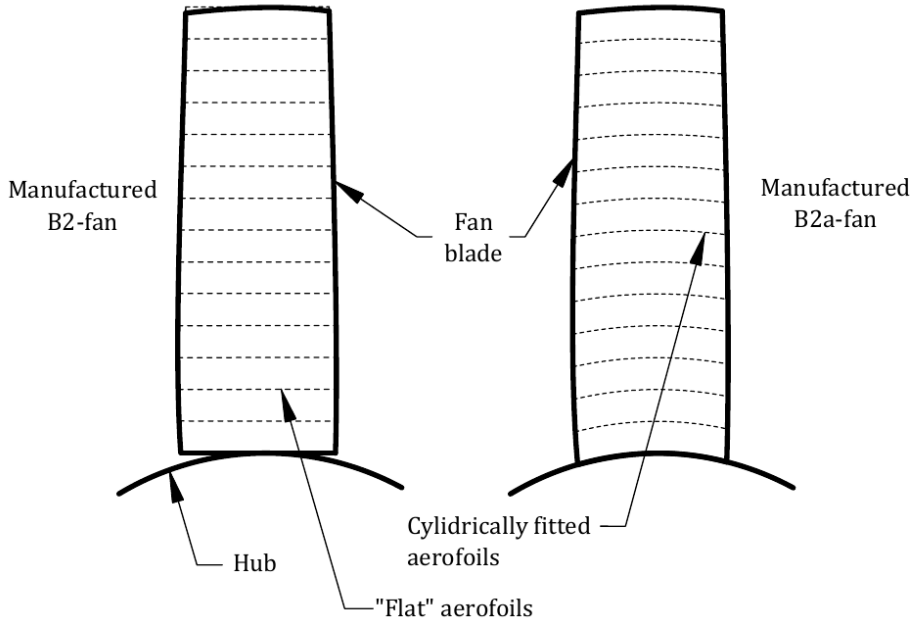

Figure 2.1: Difference between the B2- and B2a-fan as provided by Louw (2015)

Louw (2015) performed both experimental and numerical testing on the B2a-fan. The experimental study included total-to-static pressure rise, shaft torque, rotational speed, and blade surface pressure measurements at a wide range of flow rates. The numerical results contain the same data, as well as velocity and pressure profiles at the inlet and outlet of the rotor region. The near free-vortex design of the fan was confirmed by assessing the velocity profiles.

2.2 Hub Effects on Axial Flow Fans

No published research could be found that focused primarily on hub effects of axial flow fans. Despite this, many observations of hub effects have been made due to its influence on fan performance.

Longhouse (1977) investigated the effects of adding serrations to an axial flow fan blade to mitigate vortex shedding noise. He observed that fan stall occurs locally at the hub and is induced by the leading edge of the blade. By adding serrations to the leading edge, the boundary layer is energised and delays the onset of stall.

Wallis (1983) covers detailed design procedures for axial flow fans. In these procedures, a recommendation is made to make use of a 'streamlined' body as

Stellenbosch University https://scholar.sun.ac.za

a hub. Such a streamlined body is shaped like a teardrop, with its maximum radius at 40 % of its length. The fan blades would then be placed on this maximum point, resulting in a slightly more oblique upstream shape and a smooth reduction downstream of the fan. Wallis (1983) states that the nose fairing can be shortened into a hemispherical shape (round hub), where the tail should rather be stretched to discourage flow separation. Such a streamlined body would negate flow separation occurring downstream of the fan. The implementation of this would, however, be impractical, given the space restrictions inside of an ACC.

Venter (1990) showed that hub geometry has a large impact on axial flow fan performance. He noted that dramatic reversed flow was seen at the fan hub with the blade stems exposed, and the severity scaled with an increase in static pressure. With a thin disk installed over the blade roots, an increase in efficiency was noted at lower flow rates at the cost of a decrease in efficiency at higher flow rates. The crossing point was observed to occur at a much higher flow rate when the disk was installed downstream compared to upstream of the blade.

Downie *et al.* (1993) measured the spanwise flow profiles downstream of three different axial flow fans. These measurements were done over a range of flow rates, with particular attention paid to flow rates below the design point value. A trend was found that showed that reverse flow originates at the hub at lower flow rates, but that the flow remains attached at higher flow rates. Furthermore, due to recirculation, a large increase in radial velocity was observed at lower flow rates.

Estevadeordal *et al.* (2000) compared results from a panel code to digital particle image velocimetry (DPIV) data for a low-speed axial flow fan with a square hub. Differences were found between the two methods due to boundary layer growth on the surface of the hub. This thick boundary layer caused flow stagnation on the pressure side of the blade. It was further suggested that separation over the square shaped hub causes flow acceleration through the rest of the rotor domain.

Duesimi (2015) investigated the effect of different hub configurations on the static pressure and static efficiency of the B2a-fan. Amongst the hub configurations tested was a square hub, a thin disk placed over the root of the blades, and a rounded nose hub. These hubs are shown in Figure 2.2, as provided by Duesimi (2015).

Stellenbosch University https://scholar.sun.ac.za

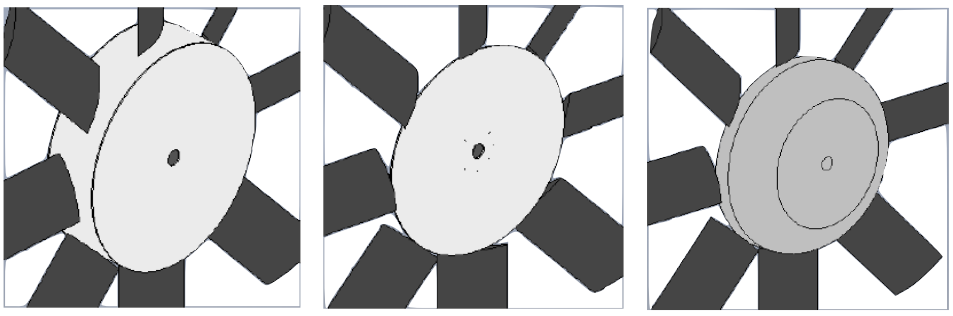

(a) Square hub (b) Disk hub (c) Round hub

Figure 2.2: Hub configurations used by Duesimi (2015)

It was found that at design point and higher volumetric flow rates, the square hub provided the highest total-to-static pressure rise and efficiency, while the disk hub performed worst in both measures. The difference at design point between the square hub and the disk hub is about 5 Pa and 5 % (absolute value) for total-to-static pressure rise and efficiency, respectively. At 62.5 % of design flow rate, the disk hub provided the highest total-to-static pressure rise. At this flow rate, the total-to-static pressure rise is 20 Pa higher than that of the worst performing square hub. The difference in efficiency between the three geometries is negligible at this flow rate, with the round hub performing marginally better than the other two configurations.

Wilkinson *et al.* (2019) found similar results when comparing the performance of a disk hub and square hub on the M-fan. Once again, the disk hub resulted in superior efficiency at low flow rates, while the square hub's performance was better at higher flow rates. Furthermore, the difference in pressure rise between the two hub configurations are minimal and dependent on blade setting angle. Wilkinson *et al.* (2019) fails to make any conclusions on the reasons for the difference in performance for the two hub configurations, which suggests research into this has yet to be performed.

2.3 Off-design Operation of an Axial Flow Fan

After reviewing literature on different hub configurations and their relevant performance effects, it is noted that many of these effects are functions of the operational flow rate relative to the design flow rate of the fan.

Axial flow fans are designed to operate at a single design point. However, distorted inlet conditions and fan position within an ACC array leads to a higher than designed for pressure duty (Van Der Spuy and Von Backström,

Stellenbosch University https://scholar.sun.ac.za

2015). This leads to a reduction in the volume flow rate passing through the fan.

Himmelskamp (1947) investigated a twin-bladed propeller using blade surface pressure measurements. It was found that the high angle of attacks experienced by the blades due to low flow rates produced significantly more lift than a two-dimensional aerofoil could achieve. This was thought to be due to delayed stall occurring in the rotating blade. This was investigated further by Gur and Aviv (2005) who confirmed that high radial flow at low flow rates causes delayed boundary layer separation due to the Coriolis effect. Gur and Aviv (2005) conclude that the linear region of lift against angle of attack for a rotating blade extends past that of an equivalent two-dimensional blade.

Meissner (2018) showed that at lower flow rates, recirculation occurs at the hub. This recirculation causes blockage and results in the fan outlet containing a high radial flow component.

2.4 Axial Flow Fan Modelling

A review of literature discussing the numerical modelling of an axial flow fan is performed.

2.4.1 Typical Flow Domain

ISO 5801 (2007) specifies four different test categories for axial flow fans, shown in Figure 2.3. These can be summarised as:

- Type-A: Open inlet and open outlet
- Type-B: Open inlet and ducted outlet
- Type-C: Ducted inlet and open outlet
- Type-D: Ducted inlet and ducted outlet

Stellenbosch University https://scholar.sun.ac.za

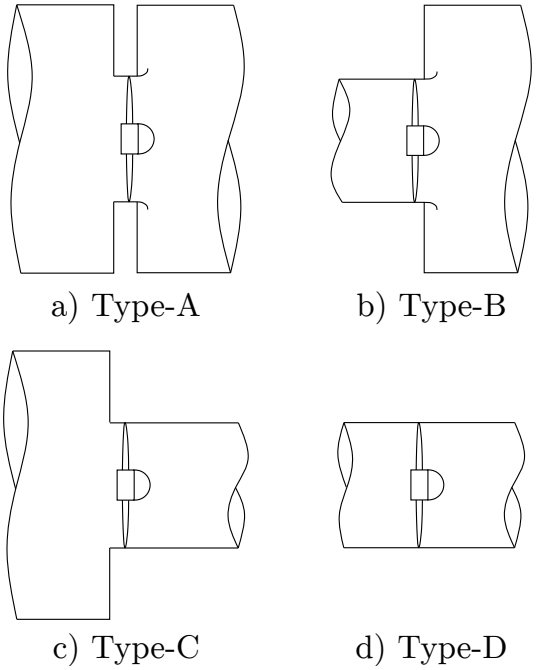

Figure 2.3: ISO 5801 fan testing facility types

The Type-D setup was used by Angelini *et al.* (2017), Beiler and Carolus (1999), Corsini and Rispoli (2004), Wilkinson (2017), Sahili *et al.* (2013) and Zuzul (2017) in order to model the performance of axial flow fans. The computational domain consists of an annulus that effectively extends the shroud and hub zones axially. This allows for a reduction in the size of the computational domain while still maintaining an accurate solution (Louw, 2015). As such this would be the model of choice for studies that do not consider hub effects.

Le Roux (2010) made use of a Type-A domain to model the B2-fan. This was done to include the effects of the hub and more closely relate to the experimental testing of the fan. A square shaped hub was analysed due to easier mesh construction with a hexahedral cell meshing strategy. Le Roux (2010) had difficulty in modelling the outlet of the domain due to reverse flow occurring at the domain exit. To prevent this, he employed a pinch at the outlet of the domain, shown in Figure 2.4, to accelerate the flow and avoid recirculation. This was found to help stability at low flow rates, but a domain without a pinch produced better results when converged.

Stellenbosch University https://scholar.sun.ac.za

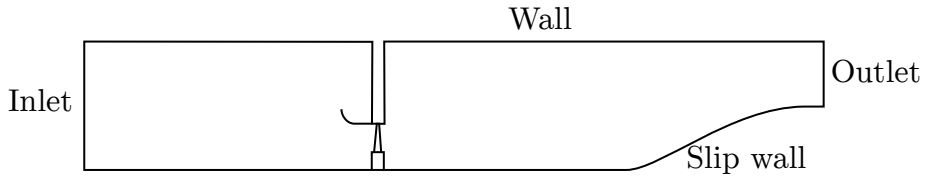

Figure 2.4: Domain used by and adapted from Le Roux (2010)

Augustyn (2013) implemented the same domain as Le Roux (2010), but did not make use of a pinch at the outlet and overcame the backflow issue by specifying the top wall on the outlet region to be an outlet boundary that allows reverse flow. This improved stability and allowed a domain without a pinched outlet to converge at flow rates down to 0 m^3/s.

Louw (2015) also made use of the Type-A setup, as it is believed that the hub and settling chambers may affect the flow field around the fan. Rather than a square hub as used by Le Roux (2010) and Augustyn (2013), a round nosed hub was modelled. This was due to the equivalent ease of meshing when using polyhedral cells and the smoother flow occurring over the round hub leading to a more stable solution. Louw (2015) made use of the same boundary conditions as Augustyn (2013) and was able to accurately model fan performance down to 25 % of the design volumetric flow rate. This setup has since been used successfully by Meissner (2018) and is the preferred method of modelling when there is an interest in hub effects.

2.4.2 Periodic Boundaries

A simplifying assumption often made when modelling turbomachinery is the use of periodicity. This allows for simplification of the domain, in order to consider only one blade passage, as shown in Figure 2.5. To accomplish this, a periodic boundary is assigned to the tangential planes where the flow is translated rotationally from one face to the other. The validity of this method was tested by Louw (2015), who found that a fair correlation was obtained between a fan tested using a periodic section and experimental result. Corsini *et al.* (2013) concluded that the use of a periodic boundary condition is valid for modelling fans in a steady-state solution. The use of a periodic domain is however limited in transient simulation or fans with high blade solidity. This is due to the onset of rotating stall, which is not necessarily a phenomenon that is periodic between single blade passages. Transient simulations may, however, be required at lower flow rates (Louw, 2015).

Stellenbosch University https://scholar.sun.ac.za

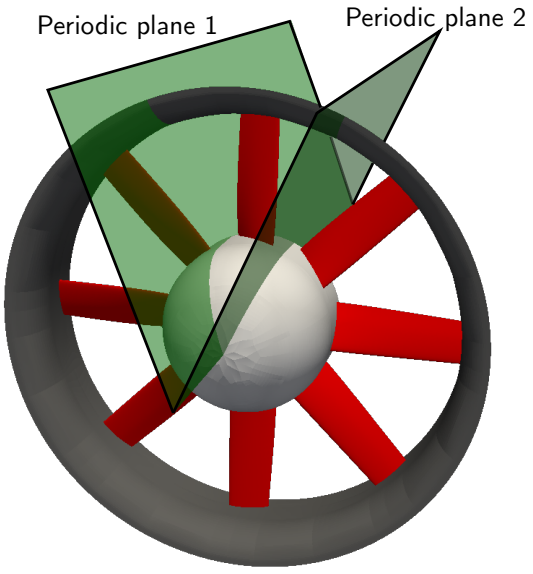

Figure 2.5: Fan periodic planes

2.4.3 Turbulence Modelling

As with the majority of engineering flows, the flow in an ACC fan is turbulent. Turbulence can be solved directly through the use of a method known as direct numerical simulation (DNS). Here, the turbulent eddies are directly resolved using the Navier-Stokes equations. These eddies may occur at a very wide range of temporal and spatial lengths and contain high vorticity, dissipative and diffusive effects (Ferziger, 2002). As a result, this method requires excessive computational resources.

Large eddy simulation (LES) fully resolves large, anisotropic eddies whilst only modelling the smaller isotropic eddies. This provides the advantage of not needing as fine a mesh to resolve turbulence effects compared to DNS, but still fully resolving the larger eddies that interact with the mean flow energy (Versteeg and Malalasekera, 2007). LES is mostly reserved for noise modelling due to a still very high computational requirement (Winkler *et al.*, 2012).

In the Reynolds averaged Navier-Stokes (RANS) formulation, unsteady eddies are not directly resolved, which relaxes the fine mesh and temporal requirements. Instead, the eddies are modelled using further transport equations. The most common RANS turbulence models used in assessed literature is the Spalart-Allmaras one equation model (Spalart and Allmaras, 1994), the k-ϵ family of models, and the k-ω family of models.

Le Roux (2010) made use of the Spalart-Allmaras turbulence model to model

Stellenbosch University https://scholar.sun.ac.za

the B2-fan, however, recommended that a k-ϵ model be investigated for future fan modelling.

Augustyn (2013) investigated three two equation k-ϵ turbulence models: the standard model (Launder and Sharma, 1974), the RNG model (Yakhot *et al.*, 1992), and the realizable model (Shih *et al.*, 1993). He found that the standard model deviated significantly from the experimental data, the RNG model only matched experimental data at low flow rates, and the realizable model correlated well with experimental data at and below the design point volumetric flow rate.

Louw (2015) also considered multiple turbulence models for modelling the B2a-fan. Comparisons were drawn based on the deviation from experimental value of the total-to-static pressure raise. At the design point, the realizable k-ϵ model deviated from the experimental result by 7.5 % compared to both the three equation k-kl-ω (Walters and Cokljat, 2008) and the four equation SST transitional (Langtry and Menter, 2009) deviating by 1.5 %. At low volumetric flow rate, the realizable k-ϵ deviation was 5.7 % and the k-kl-ω 3.5 %. Despite the larger discrepancy, the realizable k-ϵ model was preferred due to faster solution times.

Angelini *et al.* (2017) made use of the two equation low-Reynolds cubic k-ϵ turbulence model (Lien and Leschziner, 1994) to simulate an axial flow fan. Angelini *et al.* achieved an error of 3.3 % on pressure rise and 1.8 % points on efficiency.

Wilkinson (2017) compared the standard and the realizable k-ϵ turbulence models to that of the SST transitional model. No experimental data was available for validation, and a large discrepancy was seen in the k-ϵ models and the SST transitional model. The realizable k-ϵ model was used due to reduced convergence times and correlating better with the standard k-ϵ model.

Zuzul (2017) made use of the two equation k-ω SST (Menter, 1993) turbulence model to simulate the performance curve of the transonic NASA Rotor 67 turbofan. A discrepancy in the pressure ratio of about 4 % and 1 % in choke mass flow rate was found when compared to experimental data.

Meissner (2018) assessed the use of different turbulence models by simulating the aerofoil profile that the B2a-fan's blade is comprised of. He found that the realizable k-ϵ model compared poorly to experimental data, with the SST transitional model fairing better, and the Spalart-Allmaras turbulence model comparing best with the experimental data. Despite this, the k-ϵ model performed favourably compared to the Spalart-Allmaras model when a three-dimensional analysis of the fan is assessed.

Araujo *et al.* (2017) studied the difference between the k-ϵ and k-ω models

Stellenbosch University https://scholar.sun.ac.za

in a backwards facing step simulation and compared the results to a DNS simulation done by Kopera (2011). This is a good benchmark due to the similarity of flow over the back of the hub. Their results show that the k-ω SST model performed the best of the RANS models and that the k-ϵ model performed poorly in regions of adverse pressure gradients.

The turbulence modelling assessment is summarised in 2.1.

Table 2.1: Summary of turbulence modelling found in literature

Author	**Turbulence model**	**Comments**
Le Roux (2010)	Spalart-Allmaras	Recommends k-ϵ
Augustyn (2013)	Standard k-ϵ	Significant deviation from experimental
	k-ϵ RNG	Successful at low flow rates
	k-ϵ realizable	Successful at design and lower flow rates
Louw (2015)	k-ϵ realizable	Deviation of 5.7 % - 7.5 %
	k-kl-ω	Deviation of 1.5 % - 3.5 %. Long solve time
	SST transitional	Deviation of 1.5 %. Long solve time
Angelini *et al.* (2017)	k-ϵ cubic	Deviation of 1.8 % in efficiency. 3.3 % pressure rise
Wilkinson (2017)	Standard k-ϵ	Similar to k-ϵ realizable
	k-ϵ realizable	Similar to standard k-ϵ
	SST transitional	Large deviation to standard and realizable k-ϵ
Zuzul (2017)	k-ω SST	Deviation of 4 % to pressure ratio and 1 % to choke flow rate
Meissner (2018)	Spalart-Allmaras	Good correlation for 2-D, poor correlation for 3-D
	SST transitional	Fair correlation for 2-D
	k-ϵ realizable	Poor correlation for 2-D, Good correlation for 3-D
Araujo *et al.* (2017)	Standard k-ϵ	Poor correlation
	k-ω SST	Good correlation

Stellenbosch University https://scholar.sun.ac.za

2.5 Concluding Remarks

Axial flow fans such as those used in mechanical draught air-cooled condensers generate large recirculatory flow in their wake close to the hub region. Inclusion of different hub designs can mitigate this recirculation, but the choice of hub geometry also affects the pressure rise and efficiency. Literature suggests that a thin disk hub yields superior performance below design volumetric flow rate and that placing the disk downstream seems favourable when compared to placing it upstream of the blade centre. A larger box hub excels in the region above the design volumetric flow rate when compared to a thin disk. No research was found that considers the effects of shortening/lengthening the hub. Overall, trends are seen in terms of total-to-static pressure rise and efficiency for different hub configurations but the differences are relatively small. These effects are found to be strongly linked to the operating point of the fan relative to its design point.

Published CFD research modelling axial flow fans made use of one of two different domain types. Of these two, only the type-A domain is used when modelling fan hubs. The use of a periodic domain is acceptable for axial flow fans, where only a single blade passage is modelled, with the exception of low flow rates and high solidity fans. The majority of surveyed research that model axial flow fans make use of a two equation turbulence model, due to their faster solution times and acceptable accuracy. All but one making use of the k-ϵ family of turbulence models, although it has been found that the k-ω SST model may perform better.

Stellenbosch University https://scholar.sun.ac.za

Chapter 3

Domain and Mesh

This chapter describes the geometry of the domain and the construction of its computational mesh. One of the aims of this thesis is to make use of open-source software. As such blockMesh, a standard meshing utility that is packaged with OpenFOAM, is used to construct the mesh. In order to create a high quality mesh, mesh performance metrics are considered throughout the construction of the mesh. This chapter describes the fan and domain used, mesh quality metrics, a brief overview of the blockMesh utility, and how the mesh was constructed for the different geometries.

3.1 B2a-Fan

The ACC fan used in this study is the B2a-fan. The fan was developed by Bruneau (1994) and modified by Louw *et al.* (2012). It was designed for the low pressure rise, high flow rate required for ACCs and is based on a free-vortex design methodology.

The design specification of the B2a-fan is summarised in Table 3.1 and the fan itself is shown in Figure 3.1.

Stellenbosch University https://scholar.sun.ac.za

Table 3.1: B2a-fan specifications

Number of blades	8
Casing diameter	1.54 m
Hub-to-tip ratio	0.4
Blade stagger angle at hub	59^o
Design speed	750 rpm
Design volumetric flow rate	16 m^3/s

Figure 3.1: B2a-fan (Louw, 2015)

The blade profile varies linearly from the NASA LS 0413 aerofoil at the hub to the NASA LS 0409 at the tip. The two profiles are the same with exception to thickness, with the maximum thickness varying from 13 % at the hub to 9 % at the tip. This allows for a stronger blade at the hub and a lighter blade at the tip.

The blade profiles are wrapped around the hub such that the profile is described in a cylindrical rather than cartesian coordinate system. Both the chord and stagger angle varies from hub to tip, and these are expressed in Equations 3.1 and 3.2, respectively, as a function of blade radius (Louw, 2015).

$$ch = -67.013r + 204.667 \text{ [mm]} \tag{3.1}$$

$$\xi = 121.22r^3 - 277.87r^2 + 229.15r + 12.22 \text{ [°]} \tag{3.2}$$

The resultant blade profile is shown in a stacked view in Figure 3.2

Stellenbosch University https://scholar.sun.ac.za

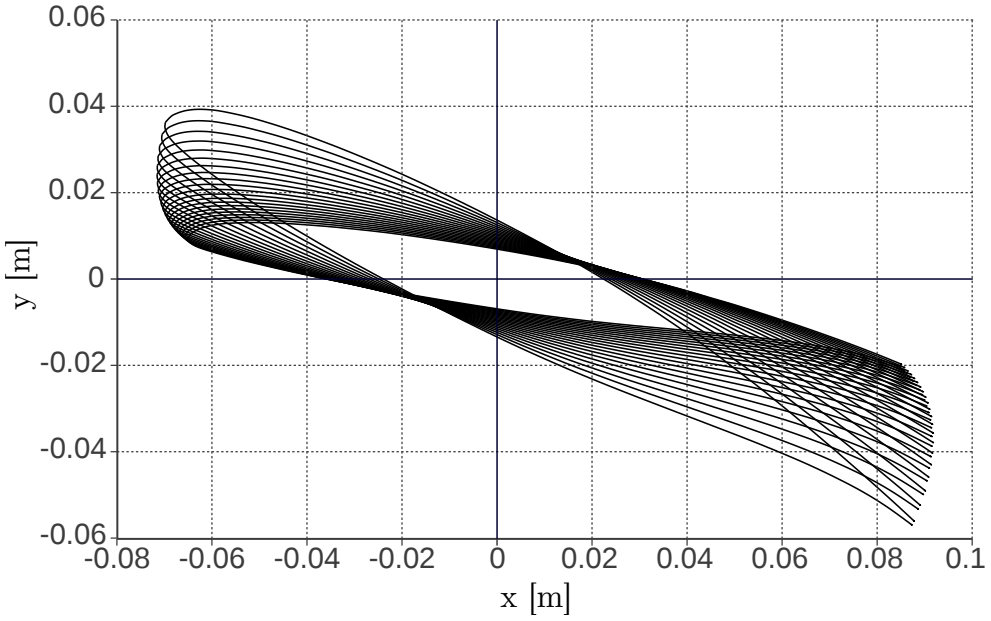

Figure 3.2: Stacked blade profile

3.2 Domain

The literature study concluded that two domains are primarily used for modelling of axial flow fans. The first simulates the fan inside a duct (similarly to a type-D setup), where the second is that of an open inlet and open outlet (similar to a type-A setup). As no evidence has been found of successful modelling of the hub region in a ducted setup, it was concluded that an open inlet open outlet setup is preferable.

Literature also suggests that a periodic method may be employed, simplifying the domain to a single blade passage. In the case of the eight bladed B2a-fan, a 45° ($1/8^{th}$ revolution) wedge with periodic sides can be used. This method is referred to as the periodic three-dimensional model (P3DM) and was verified to be valid for the B2a-fan by Louw (2015).

A meridional section of the domain is shown in Figure 3.3, along with most major dimensions. Louw (2015) conducted a domain sensitivity analyses for the B2a-fan using an open inlet and open outlet domain such as this, and confirmed that these dimensions place the rotor region suitably far from the inlet and outlet boundaries to not force unrealistic flow in order to conform to the boundary conditions.

Stellenbosch University https://scholar.sun.ac.za

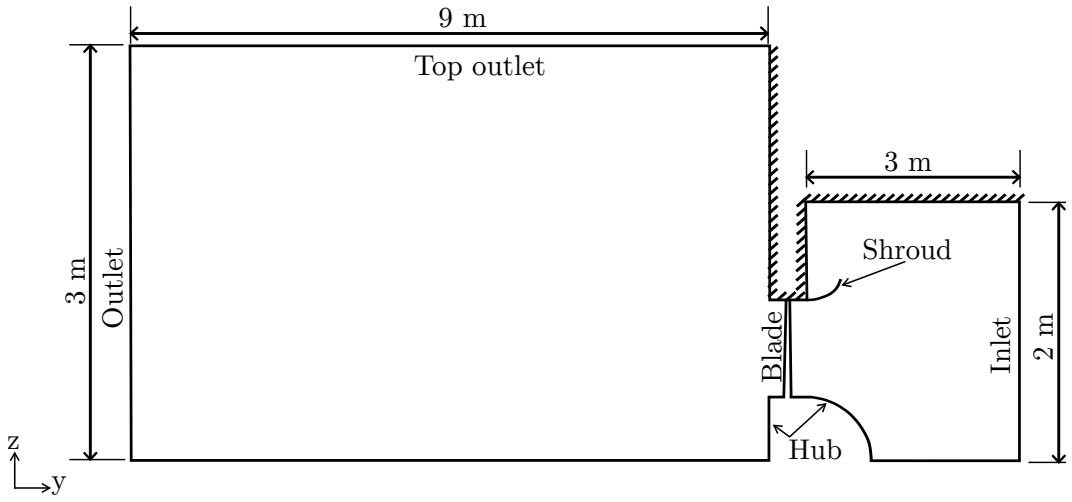

Figure 3.3: Computational domain

3.3 Mesh

3.3.1 Mesh Quality Considerations

The discretization of the Navier-Stokes equations used in CFD relies on a high quality mesh to accurately solve the resulting equations. It is generally accepted that a hexahedral mesh provides the most accurate results when aligned to the flow direction (Bern and Plassmann, 1999). These cells are assumed to consist of equal length sides with edges being orthogonal to one another. However, non-perfect cells are commonly used due to curvature present in most objects being modelled. As such, mesh quality is an important consideration for any CFD study. For this thesis, the major mesh quality concerns are that of orthogonality and skewness.

Figure 3.4a shows an example of a pair of non-orthogonal cells. Cell orthogonality is defined as the angle between two cell centres and the perpendicular bisection of the common face of those two cells (OpenFoamWiki). In the case of Figure 3.4a, this angle is represented as θ.

An example of skewness is shown in Figure 3.4b. The skewness value can be calculated as d/c. Here, the length c is the distance between two cell centres and the length d is the distance from the centre of the common face of the two cells and the point at which the line between the two cell centres intercepts the shared face.

Stellenbosch University https://scholar.sun.ac.za

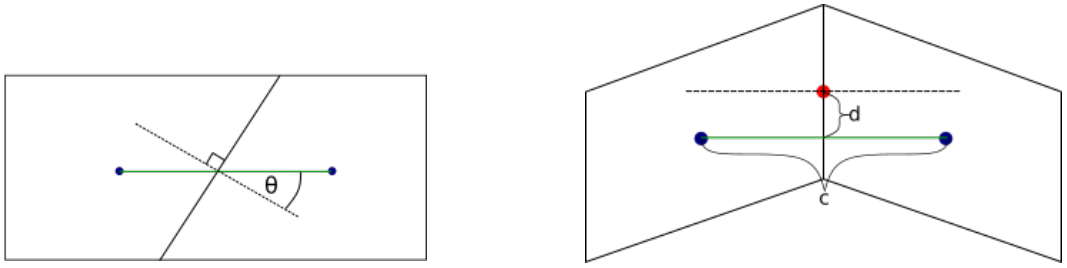

(a) Orthogonality (b) Skewness

Figure 3.4: Mesh quality considerations

OpenFOAM is packaged with a utility known as *checkMesh* that evaluates the mesh quality and statistics. It will issue a warning for any mesh that contains any cell exceeding an orthogonality of 70° or a skewness of 4. This acts as a guideline for the upper limit of these mesh parameters.

3.3.2 BlockMesh

BlockMesh is a meshing utility packaged within OpenFOAM that is used to construct structured, hexahedral meshes. BlockMesh makes use of vertices that define the position of a block's 8 corners as shown in Figure 3.5. Within each block, the number of cells in each principal axis direction is specified along with a cell grading in each direction. The faces of two blocks that overlap are automatically merged, while the faces of blocks with no neighbouring face require a boundary name. Once blocks are formed, it is possible to alter the topology of a face by specifying points that each block edge must pass through. All of this information is specified in a user-defined file named *blockMeshDict*.

BlockMesh is able to generate good quality meshes, at a sacrifice of a large setup time (Wolf Dynamics, 2017). It is possible to construct this file by hand, however for the purpose of this thesis, manually creating the dictionary file would be too tedious and time-consuming. As a result, a Python script is created that reads in a comma separated values (CSV) file containing the blade profiles at different radial locations. The blade profiles are then used to generate the mesh.

Stellenbosch University https://scholar.sun.ac.za

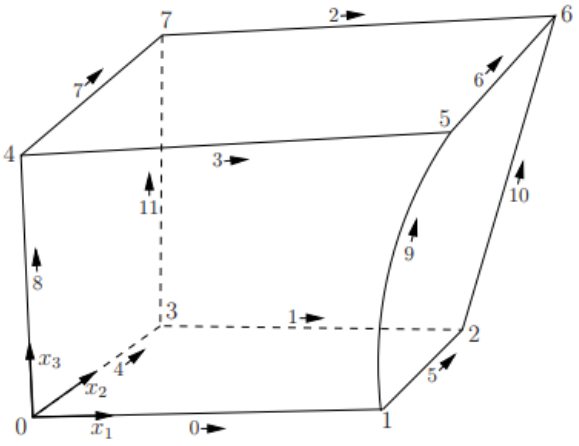

Figure 3.5: Block formation in blockMesh (OpenFOAM Guide)

Cell Grading

BlockMesh makes use of a geometric progression to define cell grading within a block in each of the three axis directions. The cell grading is specified through a ratio of the smallest and largest cells, R, and calculated using the equations given in the OpenFOAM Guide.

$$\begin{aligned} R &= r^{n-1} \\ r &= \frac{\delta x_s - l}{\delta x_s \cdot \alpha - l} \\ \alpha &= \begin{cases} R & R > 1 \\ 1 - r^{-n} + r^{-1} & R < 1 \end{cases} \\ \delta x_l &= R \cdot \delta x_s \end{aligned} \tag{3.3}$$

Here l represents the length of the block, n the number of cells in the block, r the ratio of adjacent cells' size, R the ratio of largest and smallest cell lengths, and δx_s and δx_l the length of the smallest and largest cells in the block. Figure 3.6 shows the physical meaning of some of these variables.

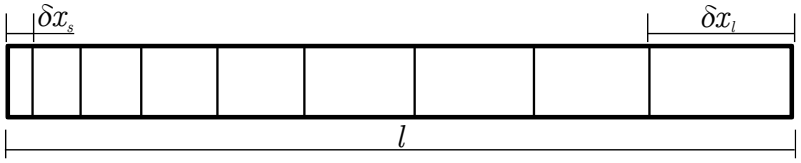

Figure 3.6: Cell grading

Stellenbosch University https://scholar.sun.ac.za

Throughout the meshing of the domain, cell grading is used to either satisfy first layer height requirements for wall turbulence modelling, or for minimisation of cell volume ratios between adjacent blocks. This is done by making use of an iterative bisection method root finding algorithm (Kearfott, 1979) to find the cell grading, specified through R, given a set of constraints. This algorithm is shown in flow chart format in Figure 3.7, where a cell grading is determined given a length, number of cells, and a target first cell height. Subscripts u, m, and l represent an upper, middle and lower estimate, respectively.

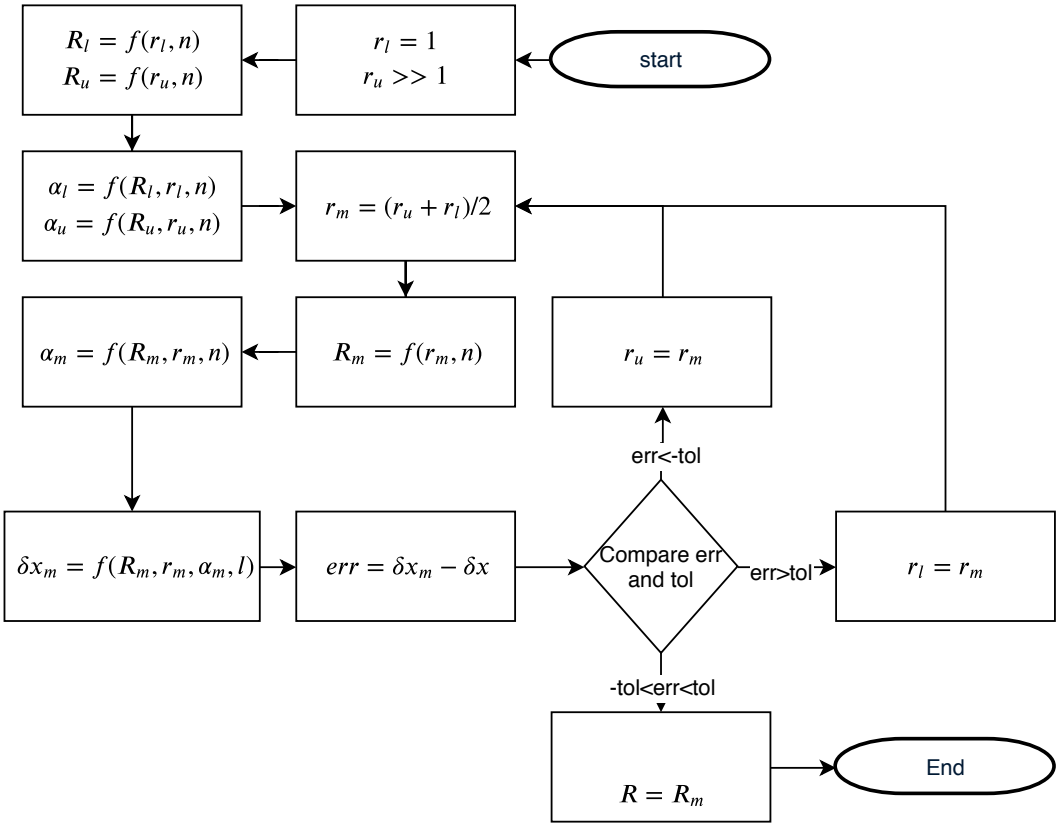

Figure 3.7: Bisection method flowchart

3.3.3 Methodology

The mesh consists of 4 regions, which are highlighted in Figure 3.8. The rotor region is constructed first, followed by the inlet region, then the outlet region, and lastly the hub region. The rotor region is constructed first since the only geometric input to the meshing process is the CSV file containing the three-dimensional point locations of the blade at different radial locations. The

Stellenbosch University https://scholar.sun.ac.za

remaining regions are then constructed based on the block vertices defined in the rotor region.

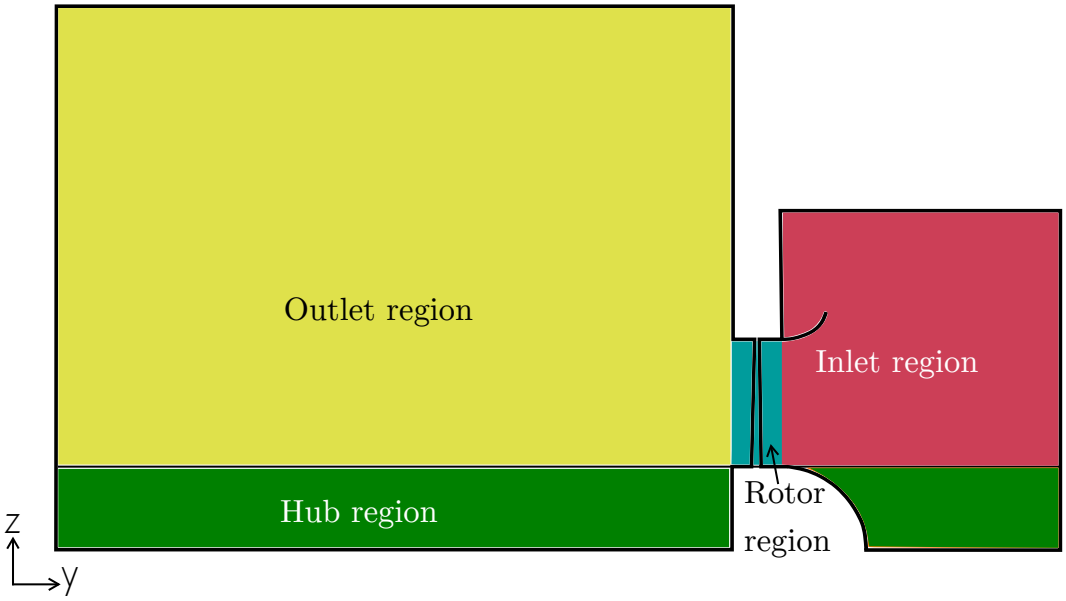

Figure 3.8: Mesh regions

3.3.4 Rotor Region

The rotor region is built up in a two-dimensional manner at distinct radial locations. Once constructed, these two-dimensional planes are 'bent' into a cylindrical plane based on their radial location. The plane is therefore located in the axial-theta directions. Figure 3.9 shows the mesh structure of this two-dimensional plane, built using sixteen individual blocks. This is a fairly universal mesh that takes into account a blunt trailing edge to mimic a realistic blade profile. It also contains thin blocks around the blade that would allow for high control of the cell density close to the blade surface and aligning the cells with the main flow direction.

Stellenbosch University https://scholar.sun.ac.za

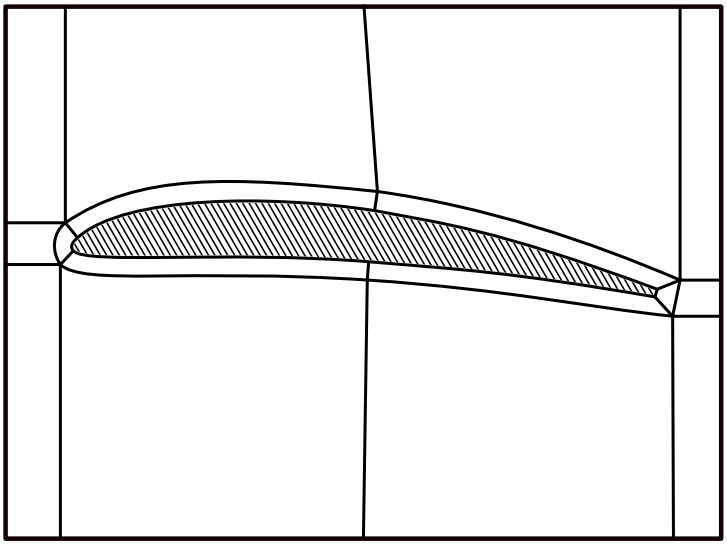

Figure 3.9: BlockMesh structure

In order to create the thin zone surrounding the blade, an extrusion algorithm was executed on the blade surface. For each point along the blade surface, the points before and after are used to estimate the gradient of the curve at the currently assessed point. The normal of this gradient is then used to extrude a curve at the distance that is required to create the desired wall region. Figure 3.10 shows this method.

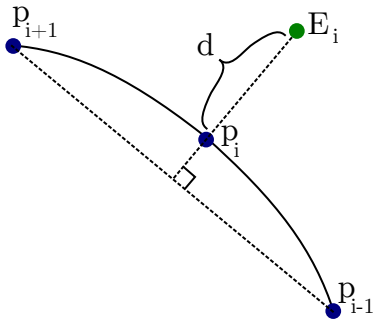

Figure 3.10: Extrusion method

As part of the algorithm, the two leading edge points must be captured such that the tangent to the blade profile is roughly 45° to the x-axis. This minimises the skewness of the cells in this area. This is demonstrated in Figure 3.11, which shows a block intersection at 45° (left) and at a larger angle (right).

Stellenbosch University https://scholar.sun.ac.za

This illustrates the significantly greater skewness and non-orthogonality that occurs at such a large angle. The same would be observed for an angle much shallower than 45°, and so 45° offers the best compromise.

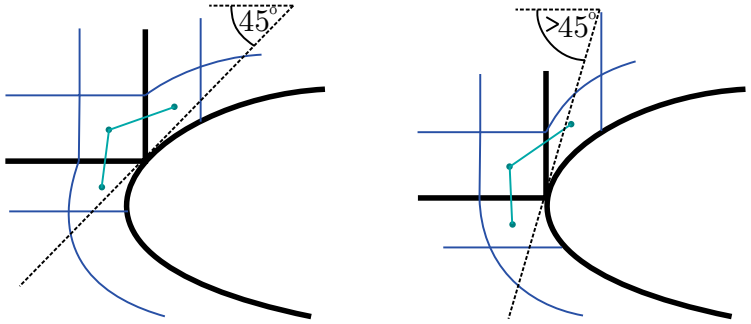

Figure 3.11: Mesh quality at 45° (left) versus a larger angle (right)

Figures 3.12 and 3.13 show coarse example meshes on the hub and shroud surface for the B2a-fan. The mesh was able to accurately capture the geometry, but at higher setting angles some issues emerged. Figure 3.12 highlights one such difficulty at the high setting angle of the hub. It can be seen that the same number of divisions need to be maintained in the axial direction for the section upstream of the blade, as well as the section downstream of the blade. This means that for the section upstream of the blade, the leading edge cells are much more compact compared to the trailing edge cells, and the opposite is true for the section downstream of the blade. This leads to overly coarse cells on the upstream trailing edge and the downstream leading edge, and overly fine cells on the remaining two corners.

This issue is not as prevalent at lower setting angles, such as at the shroud shown in Figure 3.13. A different problem that does however occur is that the areas ahead of the leading edge and behind the trailing edge expand due to the higher radial location. This causes the cells to coarsen as radial distance increases.

Stellenbosch University https://scholar.sun.ac.za

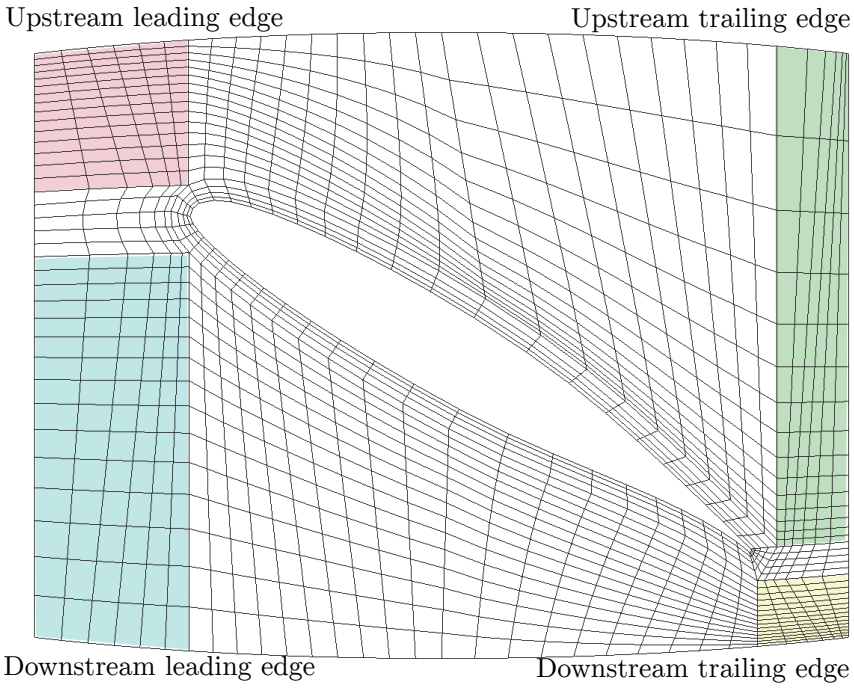

Figure 3.12: Coarse rotor section mesh at hub

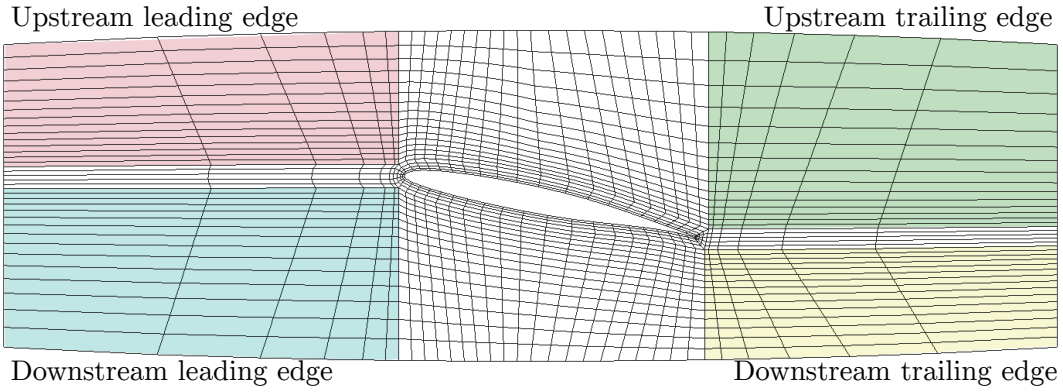

Figure 3.13: Coarse rotor section mesh at shroud

This effect can be seen in Figure 3.14, showing the front view of the rotor region. It is caused by the hexahedral cells' inability to grow from a small volume at the hub to a large volume at the shroud without some compromise.

Stellenbosch University https://scholar.sun.ac.za

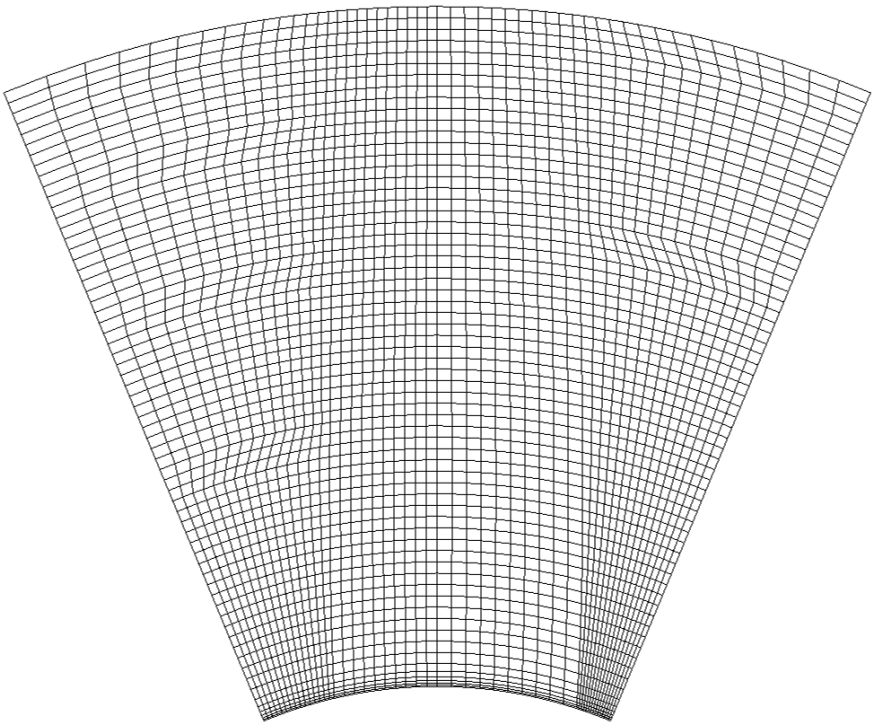

Figure 3.14: Coarse rotor section mesh front view

Cell Size Control

The cell size in the rotor region is controlled in all three axis directions.

The number of cells in the circumferential direction is specified for three different sections; in front of the leading edge, along the blade, and behind the trailing edge. The cell grading in the circumferential direction is specified such to create a minimal volume ratio jump in-between the blade section and leading or trailing edge sections respectively.

The cell size in the radial direction is specified by the number of cells in-between each radial blade profile height. The first layer cell height can be specified for both the hub and shroud surfaces by changing the cell grading in the first and last blocks, and using the root finding method illustrated in Figure 3.7.

Lastly, the cell size in the axial direction is controlled by specifying the number of cells upstream of the blade, along the leading or trailing edge of the blade, and downstream of the blade.

Stellenbosch University https://scholar.sun.ac.za

3.3.5 Inlet Region

Both the inlet and outlet regions are initially constructed in the two-dimension axial-radial plane. A radial stacking method is used to interface with the rotor region. Once meshed in two-dimensions, all the vertices are rotated to match up with the vertices in the circumferential direction defined in the rotor region.

Figure 3.15 shows this region on a coarse mesh, and how it connects to the rotor and hub regions. The bellmouth is first constructed using a splined elliptical shape. It is then cut at 45° to ensure reasonable cell orthogonality (see Figure 3.11). This region is then meshed from the rotor region to this 45° cut as highlighted in section 1. A smoothing function is also defined for this section to smooth the edges from the hub region to the bellmouth by making use of arcs. Section 2 then simply acts to extend the length of the inlet domain, whilst section 3 extends the mesh in the radial direction to create the open inlet. Lastly, section 4 meshes the back of the bellmouth. This region is expected to have low velocity flow and so is coarser than the regions upstream of the bellmouth.

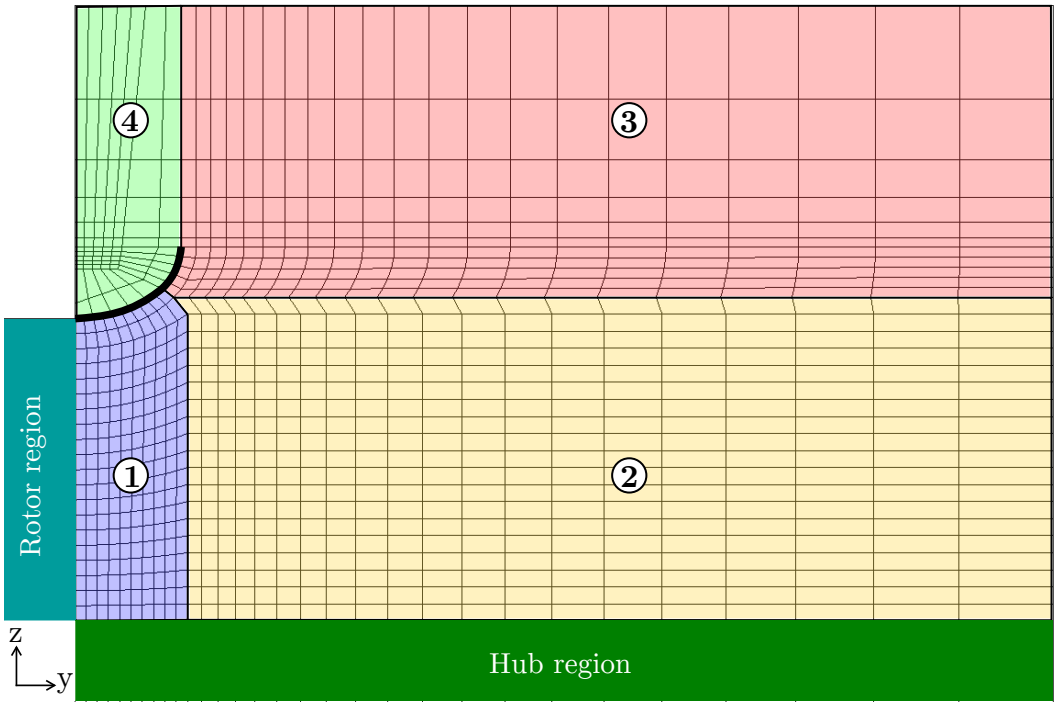

Figure 3.15: Coarse inlet region mesh

Stellenbosch University https://scholar.sun.ac.za

Cell Size Control

The cell size in the inlet region is defined by two parameters. The first is the number of cells on the surface of the bellmouth. This constrains the number of cells in the axial direction of section 1 as well as the number of cells in the radial direction of the lower half of section 3. The cell grading in the axial direction of section 1 is set to minimise the volume ratio between the section and the rotor region.

The second parameter is the maximum cell length, which constrains the axial length of the cells at the inlet boundary and the radial length of the cells on the very top boundary. The number of cells and their grading in the axial direction for sections 2 and 3 is then determined by setting δx_l to the maximum cell length and δx_s to the largest cell length of section 1 and performing the grading calculation algorithm shown in Figure 3.7.

The radial cell density for sections 1 and 2 is controlled by the radial cell count given in the rotor region. The same is true for the tangential cell density of all sections. The number of cells on the surface above the bellmouth is half the number on the bottom surface (section 4 and section 1 respectively). Once again, this is both due to the low velocities in this region and the fact that the area is smaller than below the bellmouth.

3.3.6 Outlet Region

The outlet region mesh is similar to that of the inlet region. The major difference is the exclusion of the bellmouth, which dramatically simplifies the mesh in this region.

The outlet region mesh is broken up into two sections, as shown in Figure 3.16. The first section is a simple axial expansion of the rotor region, while the second section expands radially in order to conform to the open outlet condition.

Stellenbosch University https://scholar.sun.ac.za

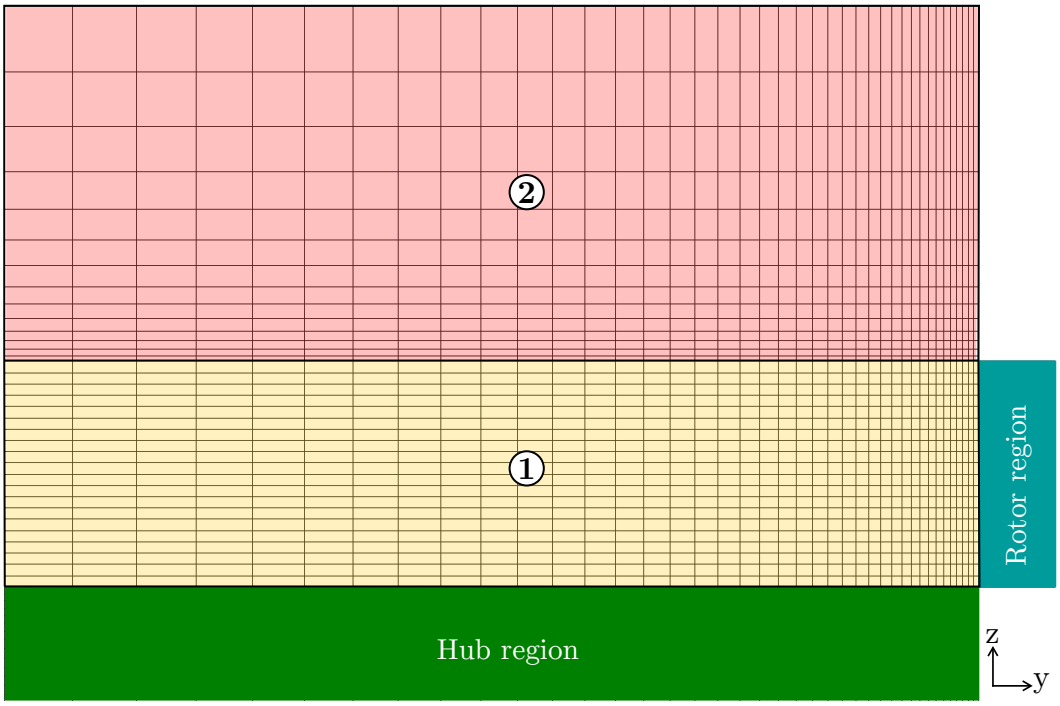

Figure 3.16: Coarse outlet region mesh

Cell Size Control

The cell size of this region is controlled through a single parameter; the maximum cell length. For section 1, δx_l is set to this maximum length while δx_s is set to the hub surface first layer height. From this, the number of cells and its grading can be determined in the axial direction.

The radial cell density of section 2 is defined by once again setting δx_l to the maximum cell length and δx_s to the first layer height at the shroud surface. The axial density is controlled by section 1, and both sections' circumferential density is controlled by the rotor region circumferential cell density.

3.3.7 Hub Region

The hub region connects the inlet and outlet regions to the axis of rotation. It spans from the inlet boundary to the outlet boundary, with a void where the hub is located. Three different hub geometries are investigated: a square hub, a round hub, and a disk hub. These three hub geometries are shown in Figures 3.17 to 3.19, respectively. It can be seen that the domain for each hub

Stellenbosch University https://scholar.sun.ac.za

geometry differs and, as a result, different meshing strategies are employed for each.

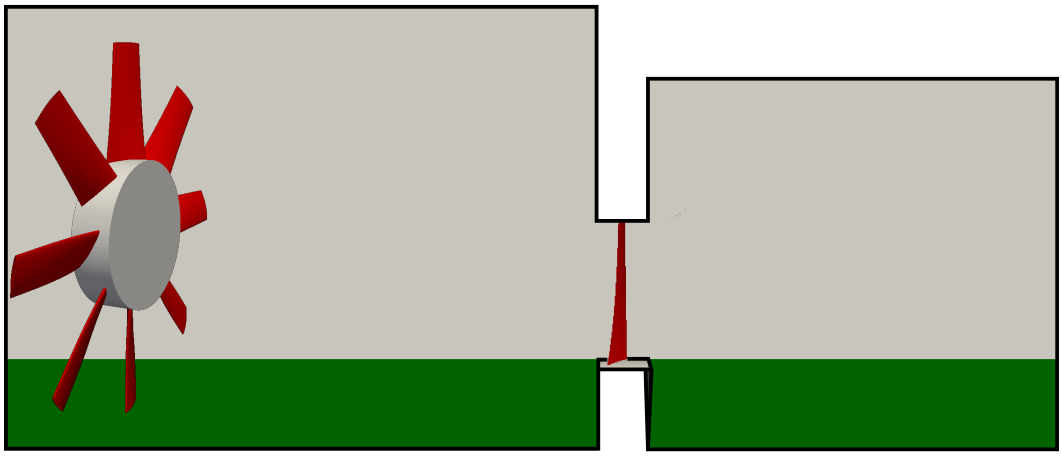

Figure 3.17: Square hub configuration

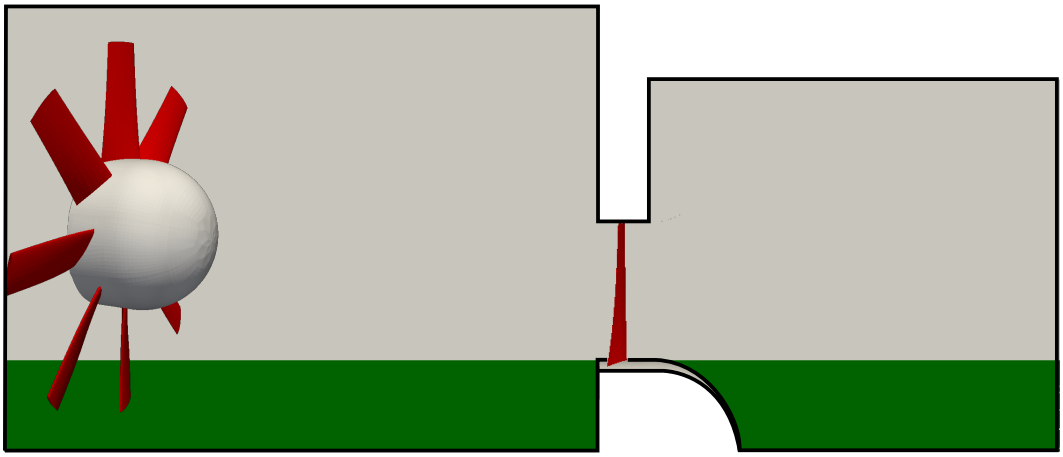

Figure 3.18: Round hub configuration

Stellenbosch University https://scholar.sun.ac.za

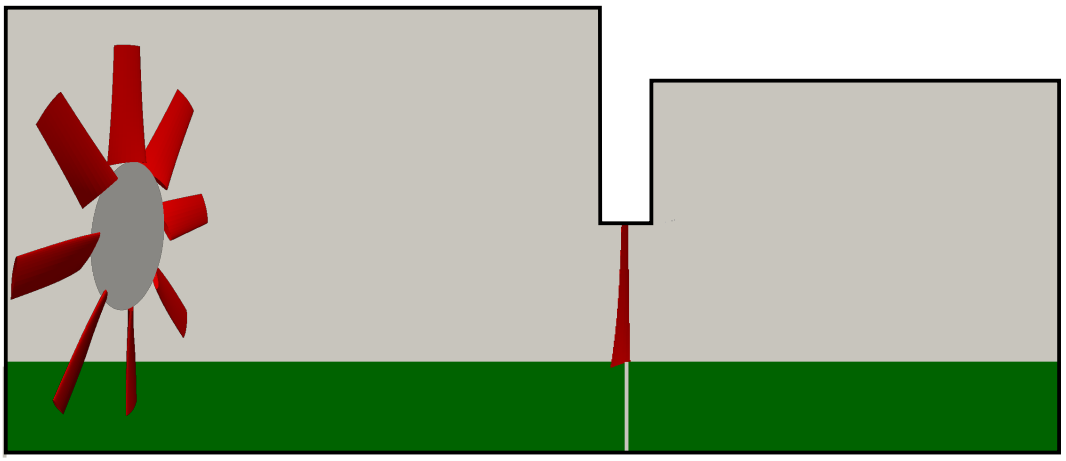

Figure 3.19: Disk hub configuration

Square Hub

The square hub is the simplest of the hub geometries to mesh, as the problem is once again only two-dimensional. The two-dimensions considered are the radial and circumferential directions.

The hub region is described as a cylindrical volume that has been cut into a 45° wedge, as demonstrated in Figure 3.20. The main challenge is meshing this wedge using a quadrilateral mesh, as the wedge only contains three sides. Furthermore, the mesh needs to conform to the location of the five vertices already defined in the circumferential direction in the rotor region as shown in Figure 3.9.

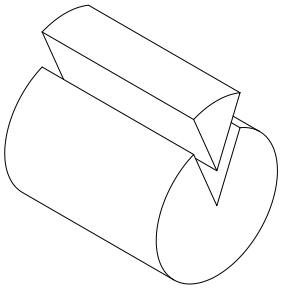

Figure 3.20: Wedge shape

Figure 3.21 shows how this mesh structure is accomplished. A variation of a standard structured mesh inside a pipe is used to accommodate the constraints

Stellenbosch University https://scholar.sun.ac.za

of the rotor region.

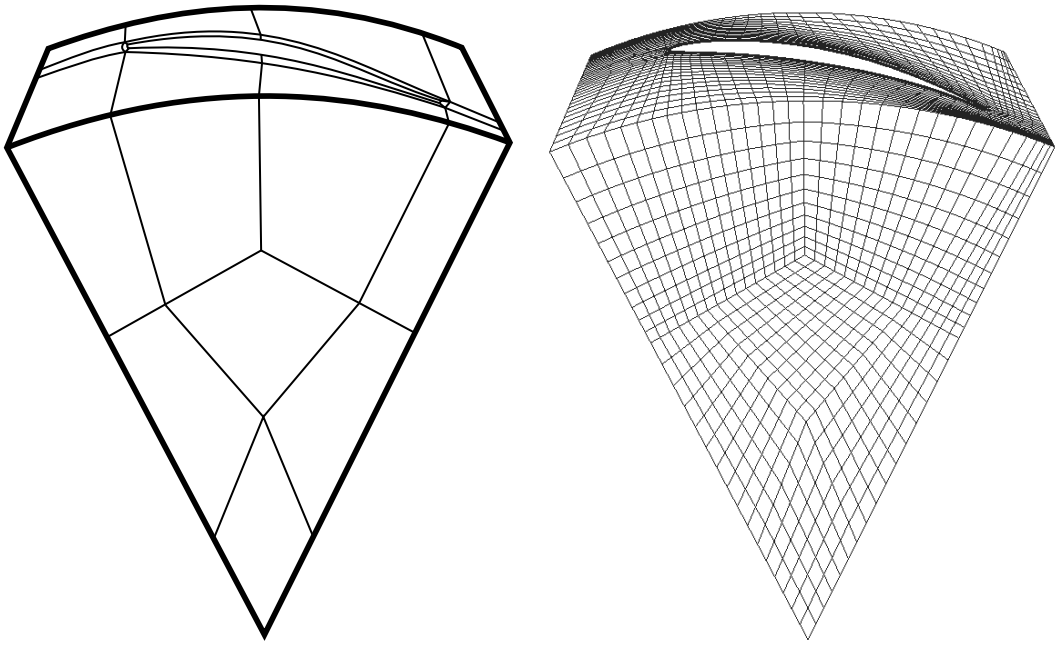

Figure 3.21: Mesh structure on square hub surface

This two-dimensional mesh is extended from the inlet to the upstream hub wall and then again from the downstream hub wall to the outlet. This creates a continuous hub region mesh from inlet to outlet with a gap for where the hub is located.

Round Hub

The round hub is meshed similarly to the square hub. The only difference is that at the upstream hub interface, the meshing becomes a fully three-dimensional problem.

The same structure is used as that of the square hub, except that the vertex points at the upstream hub wall are offset in the axial direction to follow a hemispherical shape. The edges are then specified to follow an arc so that the entire boundary forms a smooth round shape as shown in Figure 3.22. The rest of the hub region is treated the same as that of the square hub.

Stellenbosch University https://scholar.sun.ac.za

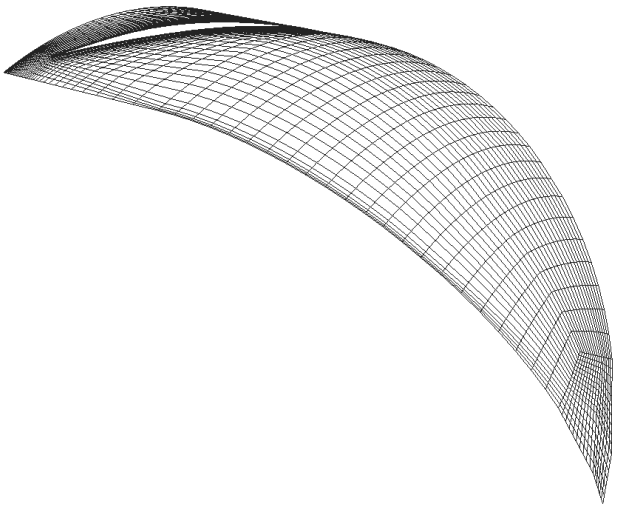

Figure 3.22: Mesh structure on round hub

Disk Hub

The third hub geometry, the disk hub, makes use of the same mesh as the square hub. There is, however, no gap underneath the rotor region. Instead, this region is meshed from the start of the rotor region to the end, creating a nonconformal mesh between it and the rotor region.

Figure 3.23 shows this nonconformity. In order to allow for the transfer of information between the rotor region and this hub region, a *cyclicAMI* boundary condition is used. For this, a master and slave rotor-hub interface is generated as shown in Figure 3.24. This is a trivial task for the hub region, however, the rotor region has a hole in the mesh where the blade is placed, as can be seen in Figure 3.9.

Stellenbosch University https://scholar.sun.ac.za

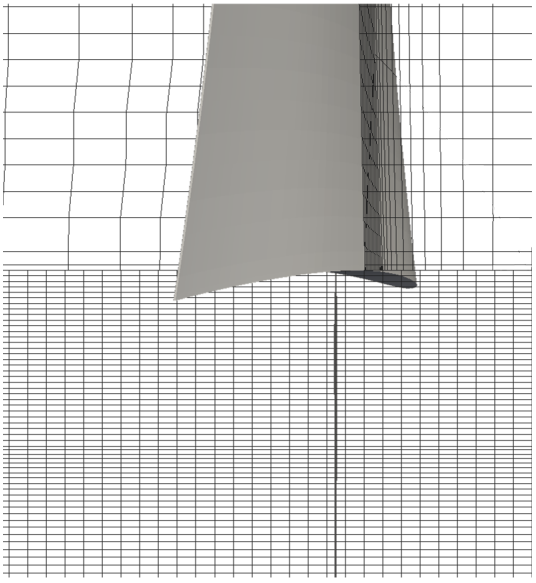

Figure 3.23: Nonconforming mesh between rotor and hub regions

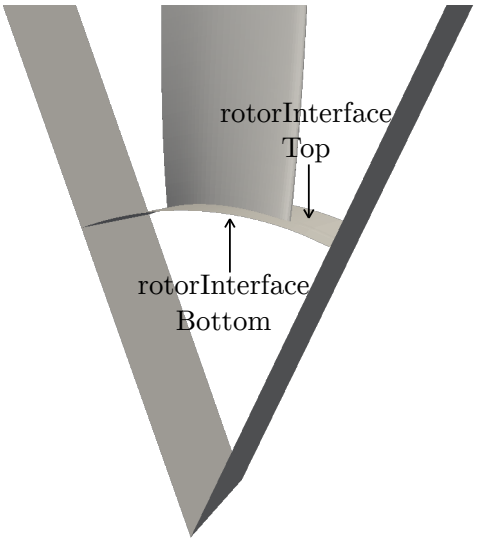

Figure 3.24: Hub-rotor interface

To remedy the hole in the rotor region mesh, a mesh is generated for the internal region of the blade. As no leakage through the inside of the blade is desired, this region is made thin. Figure 3.25 shows this thin internal mesh. The single cell thickness allows for a completely sealed rotor region interface, which can then successfully transfer information across to the same interface located in the hub region.

Stellenbosch University https://scholar.sun.ac.za

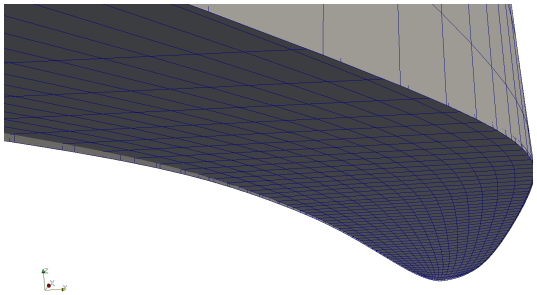

Figure 3.25: Blade internal mesh

Due to the axially uniform mesh generated in the hub region underneath the rotor region, it is trivial to implement an infinitesimally thin plate. This is done by specifying a baffle using the *createBaffles* utility, which simply creates a patch in between cells, and therefore does not make any changes to the mesh.

Figure 3.26 shows the surface mesh of the blade and thin disk. A further advantage of making use of baffles to define the disk location, is the ability to move the disk to any axial point in the domain.

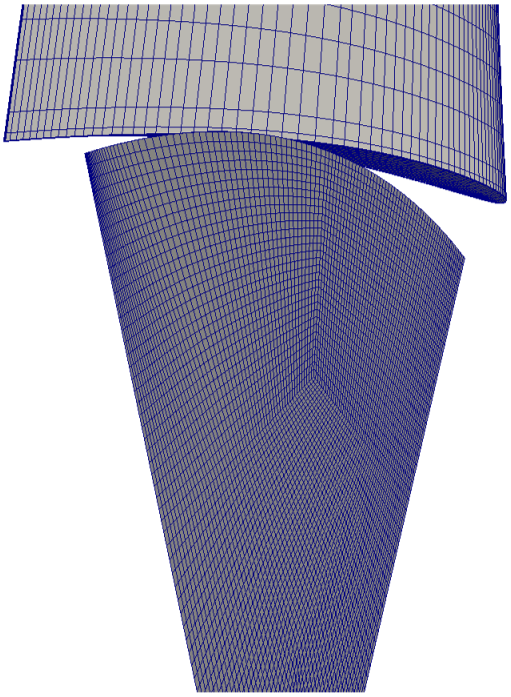

Figure 3.26: Disk hub mesh

Stellenbosch University https://scholar.sun.ac.za

Chapter 4

Boundary Conditions and Solver Settings

With the domain and mesh constructed, the requirements for solving the Navier-Stokes equations are discussed in this chapter. A requirement for solving any set of partial differential equations is that each variable is described by either its value (Dirichlet boundary) or gradient normal to the boundary (Neumann boundary). These boundary conditions are described herewith. Furthermore, the methods used to link pressure and velocity and the interpolation methods are described. Lastly, a convergence criterion is set which would define the requirements to consider a solution suitably converged.

4.1 Boundary Conditions

The flow variables of interest are those of the velocity vector ($\vec{U}$), pressure (p), turbulent kinetic energy (k), and dissipation rate (ϵ) or specific dissipation rate (ω) where applicable. These are specified at each boundary shown in Figure 4.1, with the boundary types being split up into three main categories: inlet, outlet, and wall.

Stellenbosch University https://scholar.sun.ac.za

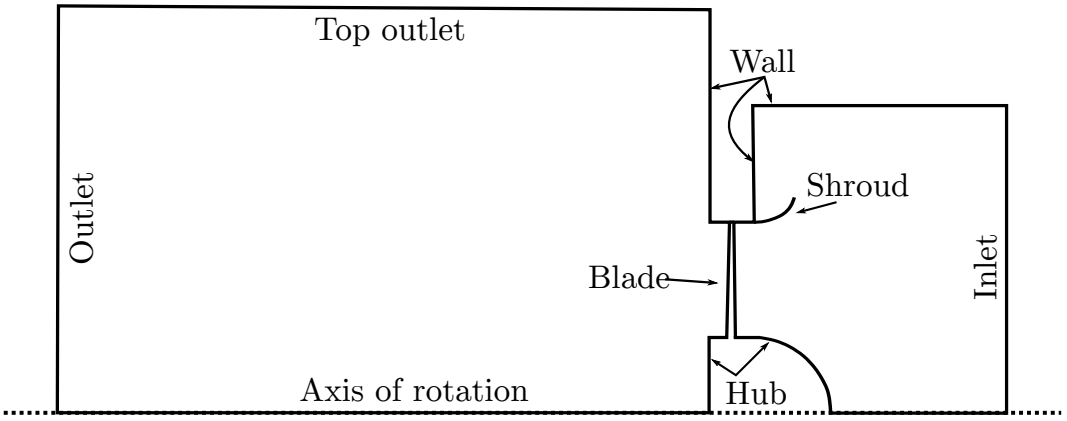

Figure 4.1: Computational domain

4.1.1 Rotating Reference Frame

A rotating reference frame is employed over the entire domain. However, the only boundaries that are rotating are the blade and hub. As a result, all other boundaries are specified as being non-rotating. This means that all boundary values are given in an absolute reference frame, whereas the hub and blade's boundary values are given in the rotating reference frame.

4.1.2 Inlet

The inlet boundary is set to a known velocity value, U_{inlet}, that is determined based on the required volumetric flow rate. It is specified as a constant fixed velocity profile with only an axial component. The pressure is specified as a Neumann boundary with a zero gradient.

The turbulence properties k, ω, and ϵ are set based on a mixing length and turbulence intensity values. The intensity chosen is 1 % as recommended by Louw (2015). The length scale employed is 0.23 m as this is half of the rotor region channel height.

4.1.3 Outlet

Both the outlet and top outlet boundaries described in Figure 4.1 are treated the same as they both represent an atmospheric free-stream outlet. The treatment of the top outlet as an atmospheric outlet was found to improve solution stability by Augustyn (2013). The static pressure at these boundaries is fixed

Stellenbosch University https://scholar.sun.ac.za

in order to set a reference pressure for the solution. The exact value of this is not important as for an incompressible solver only the pressure difference is considered. In this case, a value of 0 Pa is used to minimise the size of pressure values used and thereby minimise round-off errors.

The boundary condition for velocity must be able to handle both inflow and outflow. In the case of a cell with outflow, a zero gradient condition is applied. In the alternative case of inflow, the velocity is computed based on the normal component of the next internal cell. This is known as a *pressureInletOutletVelocity* in OpenFOAM.

A similar boundary condition to that used for the velocity field is employed for the turbulence properties. Once again, outflow is treated with a zero gradient boundary, whereas inflow sets a fixed value equal to that used at the inlet.

4.1.4 Walls

All the walls are treated the same. These include the hub, shroud, bellmouth, blade, and the settling chamber walls. To conform with the no slip condition, the velocity on the walls is set to 0 m/s and the pressure is set to have a zero gradient. The boundaries of the blade and hub are in the rotating reference frame and so their actual velocities will be a function of the radial distance away from the axis of rotation and the rotational speed of the fan. The turbulence properties are calculated using a wall function approach. For k, a zero gradient is adopted, and ω or ϵ is calculated as shown in equation 4.1, where $C_\mu = 0.09$ and $\kappa = 0.41$.

$$\omega = \frac{\sqrt{k}}{C_\mu^{0.25}\ \kappa\ y_1} \qquad \epsilon = \frac{C_\mu^{0.75}\ k^{1.5}}{\kappa\ y_1} \tag{4.1}$$

The boundary conditions discussed are summerised in Table 4.1.

Table 4.1: Boundary conditions

Property	Inlet	Outlets	Walls
$\vec{U}$	fixed value	FVI-ZGO[1]	no slip
p	zero gradient	fixed value	zero gradient
k	1 % intensity	FVI-ZGO[1]	wall function
ϵ or ω	0.23 m mixing length	FVI-ZGO[1]	wall function

[1] Fixed value for inflow, zero gradient for outflow

Stellenbosch University https://scholar.sun.ac.za

4.1.5 Periodic Planes

The implementation of periodic boundaries in OpenFOAM is done through an option of two boundary conditions: *cyclic* and *cyclicAMI*. Both are able to transform flow variables from one patch to another by specifying a rotation axis. The cyclic boundary condition maps information across the two boundaries using a simple cell to cell connection. As such, the periodic planes require a conformal mesh in order to work. The cyclicAMI boundary, on the other hand, makes use of an artificial mesh interface algorithm to interpolate between cells on the neighbouring periodic boundary. This allows for non-conformity between the neighbouring patches but may introduce numerical errors due to interpolation. An investigation done by Chandar and Gopalan (2016) confirmed OpenFOAM's ability to model periodicity by using a simple geometry that made use of a cyclicAMI boundary condition. It was found to achieve good accuracy at mapping field data between cells with inconsistent cell centres.

Due to the difficulty of meshing the rotor region in such a way that the periodic planes have a conformal mesh; the cyclicAMI boundary condition is used.

4.2 Solution Schemes

The SIMPLE (Semi-Implicit Method for Pressure Linked Equations) algorithm of Patankar and Spalding (1972) is used to calculate the pressure and velocity field.

To aid with convergence, under relaxation parameters are specified. These values were found through trial and error, as a compromise between stability and quick solution time, and are specified in Table 4.2.

Table 4.2: Relaxation factors and divergence schemes

Variable	Divergence scheme	Relaxation factor
p	-	0.4
U	linearUpwind	0.7
k	upwind	0.6
ϵ or ω	upwind	0.6

Table 4.2 also shows the divergence schemes used. The linearUpwind scheme is used for the velocity terms as a second order scheme provides for an increase in accuracy compared to first order schemes. Furthermore, the upwind biasing

Stellenbosch University https://scholar.sun.ac.za

contributes to the transportive nature of the flow. The turbulence properties k, ω, and ϵ are solved with an upwind differencing scheme.

4.3 Convergence Criteria

In order to assess convergence, the total-to-static pressure rise across the domain, as well as the power consumption of the fan rotor is considered. These parameters are chosen since they define the fan's performance at a given volumetric flow rate.

For the simulation to be considered converged, the pressure rise must have less than 0.5 Pa change over 5000 iterations, and the power consumption must have less than a 50 W change over those same 5000 iterations. These criteria were chosen since various trial runs showed that no simulations experienced any noteworthy changes after such a period. An example of a converged solution is shown in Figure 4.2 for the round hub at a design point flow rate of 16 m^3/s.

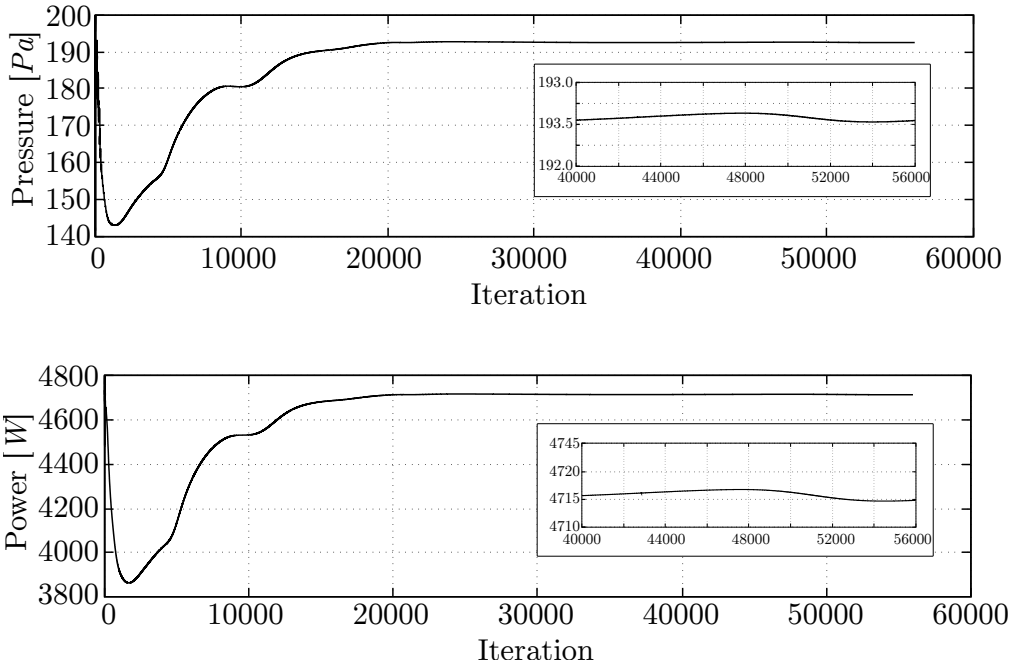

Figure 4.2: Convergence of round hub at design point

Residuals were also monitored to ensure that the partial differential equations have been reasonably solved. These are shown in Figure 4.3 for the same round hub at $\dot{V} = 16$ m^3/s.

Stellenbosch University https://scholar.sun.ac.za

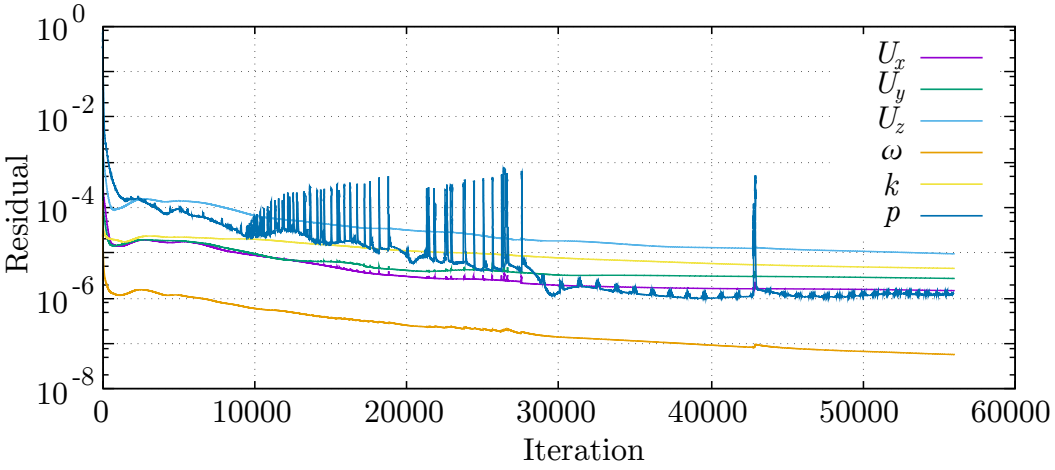

Figure 4.3: Residuals of round hub at design point

4.4 Transient Modelling

Transient modelling was found to be required for the round and square hub configurations at $\dot{V} = 10$ m$^3/s$. The PIMPLE algorithm is used for transient simulations, which is a combination of the SIMPLE and PISO (Pressure Implicit with Splitting of Operator) algorithms. The PIMPLE algorithm makes use of the PISO algorithm's ability to solve transient simulations but uses the SIMPLE algorithm at each time step to get a converged solution. This allows for more stability and larger time steps than the standard PISO algorithm.

The time step size is set by specifying a maximum Courant number. Due to the higher stability of the PIMPLE algorithm, a Courant number larger than unity may still provide a stable solution. However, a too large Courant number would result in diffusive errors. It was found through trial and error that a Courant number of 4 still provided a converging solution, and as such allows for time steps in the order of four times larger than what would be possible with the PISO algorithm.

Stellenbosch University https://scholar.sun.ac.za

Chapter 5

Validation

This chapter aims to validate the numerical modelling done in this thesis. This is done to build confidence in the model through a study of different turbulence models and comparison with experimental results.

5.1 Performance Metrics

In order to evaluate the performance of the modelled fan, performance metrics must be defined. The two main fan performance metrics are total-to-static pressure rise and efficiency. Total-to-static pressure rise is defined by ISO 5801 as the difference between the total pressure upstream of the fan and the static pressure downstream of the fan, such that

$$\begin{aligned} \Delta p_{f,s} &= p_{s,out} - p_{t,in} \\ &= p_{s,out} - \left(p_{s,in} + \frac{1}{2}\rho V_{in,avg}^2 \right). \end{aligned} \tag{5.1}$$

The fan static efficiency is defined as the ratio of the fan air power to the fan shaft power:

$$\begin{aligned} \eta &= \frac{\Delta p_{f,s}\dot{V}}{P} \\ P &= T\omega \end{aligned} \tag{5.2}$$

where torque (T) can be calculated numerically by considering the pressure and viscous forces acting on the blade and hub.

Stellenbosch University https://scholar.sun.ac.za

5.2 Turbulence Modelling

Based on the literature surveyed, the k-ω and k-ϵ turbulence model families are often used to model axial flow fans. The accuracies of these models are herewith evaluated. Another factor to consider with turbulence modelling is whether the use of wall functions is adequate, or if the boundary layer needs to be solved. The former is known as a high Reynolds approach, whereas the latter is referred to as a low Reynolds approach. As a result, three models are tested; k-ω SST with wall functions, k-ω SST solved through the boundary layer, and realizable k-ϵ with wall functions. The k-ω SST and realizable k-ϵ models are chosen due to being the most successfully used turbulence models of their respective families in literature. The models are tested for the round hub at the design point flow rate of 16 m^3/s. Details of the first layer cell height requirements for the three turbulence models can be seen in Appendix A.

Large aspect ratios that occur in cells on the hub, and extending downstream of the hub, for the low Reynolds case caused simulations to diverge. To compromise, only the blade wall's boundary layer was solved, and the rest of the walls were treated with wall functions. Despite this, the solution was still fairly unstable and small oscillations were observed in the converged solution.

Table 5.1 shows the results of the three different turbulence models. The k-ϵ model performed poorly, whereas the two k-ω models perform similarly well. Due to its simplicity and faster solution times, the k-ω SST model with wall functions was selected for use in all further models.

Table 5.1: Turbulence models studied

Turbulence model	$\Delta p_{f,s}$ [Pa] (error)	η (error)
k-ω SST high Re	189 (5.5 %)	65.3 % (5.2 %)
k-ω SST low Re	184 (8.0 %)	64.5 % (3.9 %)
Realizable k-ϵ	159 (20.5 %)	53.0 % (14.7 %)
Experimental (Louw, 2015)	200	62.1 %

5.3 Mesh Sensitivity

A full mesh sensitivity study was performed, as shown in Appendix B. Each geometry was tested on three meshes with various levels of refinement.

Total-to-static pressure rise and efficiency was monitored over the different mesh densities, and a deviation was estimated for each successive refinement.

Stellenbosch University https://scholar.sun.ac.za

A mesh with approximately six million cells was found to be sufficiently fine, without excessively increasing computational time.

5.4 Comparison to Existing Data

To ensure the accuracy of the numerical model, the simulated results are assessed against experimental results. For this, the experimental work of Louw (2015) will be used. Louw (2015) made use of the B2a-fan at the same scale as used in the current thesis. One notable difference, however, is that while Louw's work involved a 3 mm tip gap, this thesis does not model the tip gap.

5.4.1 Performance Evaluation

Figures 5.1 and 5.2 show the performance of the B2a-fan across a range of volumetric flow rates. At the design point flow rate, a deviation of 6.0 % and 3.6 % points is seen for the total-to-static pressure rise and efficiency when compared to the experimental data.

At a volumetric flow rate above the design point, both the total-to-static pressure rise as well as the efficiency is underpredicted when compared to that of the experimental results. Louw (2015) and Augustyn (2013) also noted the difficulty in obtaining accurate simulation results at higher volumetric flow rates.

At volumetric flow rates below the design point, the numerical results over predict both the total-to-static pressure rise as well as efficiency. It is suspected that a large contributor to this difference may be the lack of tip gap modelled in this thesis. The lack of tip gap would inflate the performance of the fan, and this effect would be more pronounced at lower flow rates (Downie *et al.*, 1993).

The combination of these two factors shows a curve that is steeper than the experimental results found by Louw (2015).

Stellenbosch University https://scholar.sun.ac.za

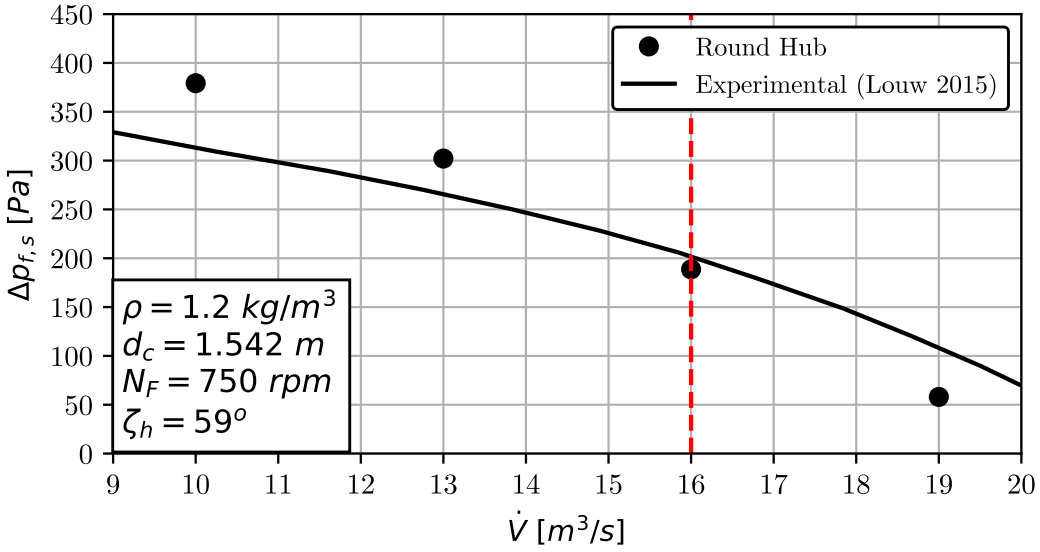

Figure 5.1: Total-to-static pressure rise comparison between the round hub and experimental data

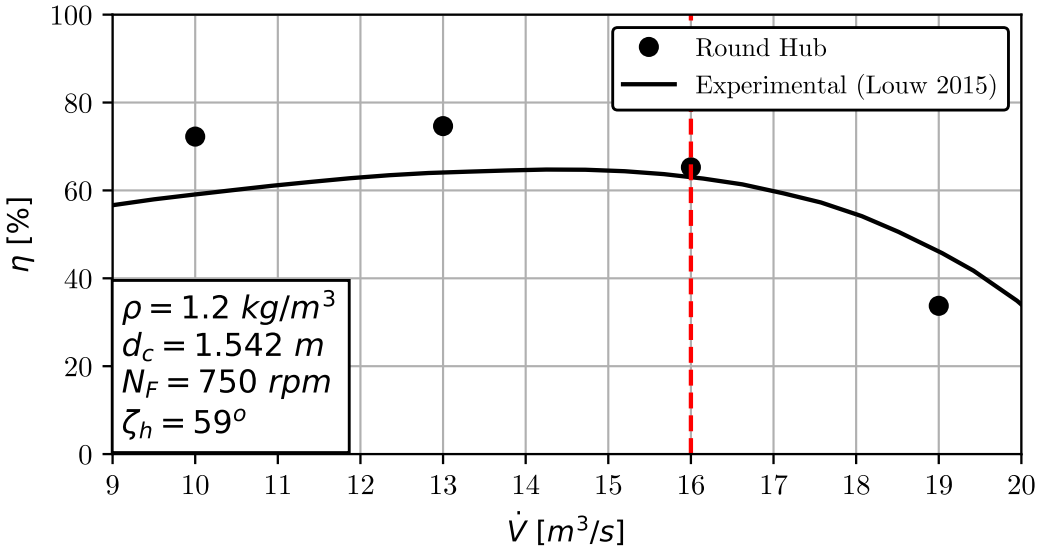

Figure 5.2: Efficiency comparison between the round hub and experimental data

Stellenbosch University https://scholar.sun.ac.za

5.4.2 Blade Surface Pressure

Louw (2015) performed blade surface pressure (BSP) measurements during testing of the B2a-fan. Seven pressure taps were placed on the pressure and suction sides each, at five different radial locations.

The pressure is nondimensionalized with the coefficient of pressure, defined as

$$Cp_u = \frac{p_s}{\frac{1}{2}\rho u^2} \tag{5.3}$$

where p_s is the static pressure on the blade, u is the blade tangential speed at that height, and ρ is the atmospheric density.

Figure 5.3 shows the BSP results at the five different radial locations, and compared against experimental results at the design point flow rate of $\dot{V} = 16\ \mathrm{m}^3/\mathrm{s}$. The x-axis is nondimensionalized to the blade chord at each radial station. Also included in each figure is a Pearson correlation factor (Pearson, 1895), R_p, and the root-mean-square difference (RMSD). The details of how the Pearson correlation and RMSD is calculated is described in Appendix C.

A good correlation between numerical and experimental data is found, as shown by each radial station's high Pearson correlation. Appendix D compares the BSP data for numerical and experimental data at off-design flow rates. It is noted that, once again, poorer agreement is obtained at above design flow rates between the numerical and experimental results, most notably near the hub.

Stellenbosch University https://scholar.sun.ac.za

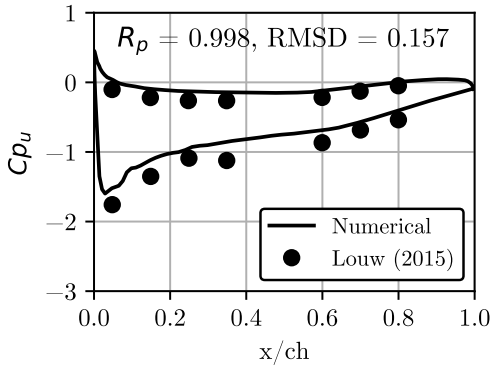

(a) 10 % blade span

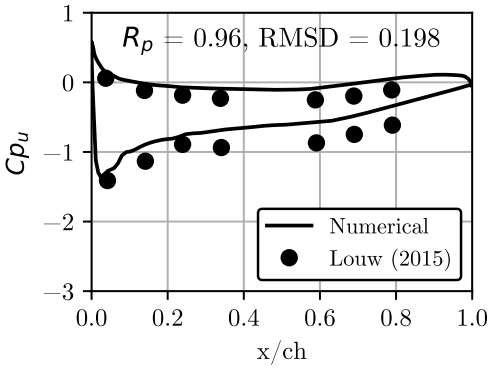

(b) 30 % blade span

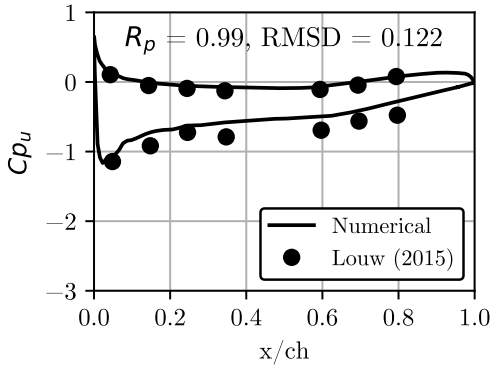

(c) 50 % blade span

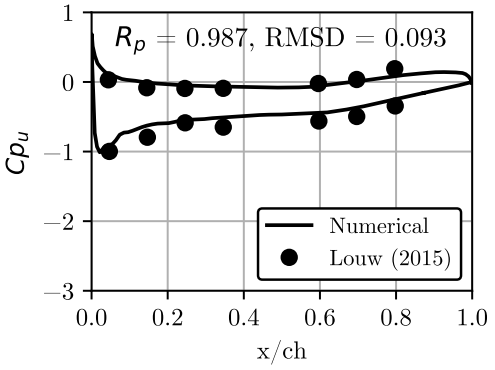

(d) 70 % blade span

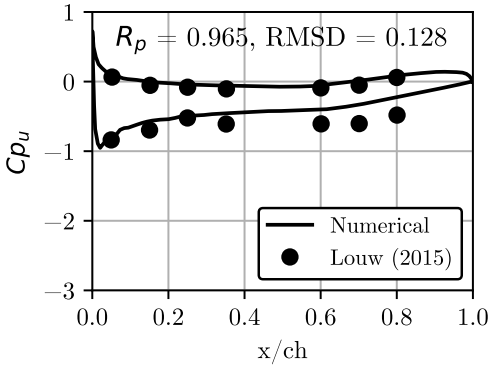

(e) 90 % blade span

Figure 5.3: Blade surface pressure at $\dot{V} = 16$ m^3/s at $sb =$ (a) 10 %, (b) 30 %, (c) 50 %, (d) 70 %, (e) 90 %

Stellenbosch University https://scholar.sun.ac.za

Chapter 6

Results

This chapter conveys the outcome of the simulations performed by comparing the results obtained from the different hub configurations evaluated in this thesis. Firstly, the global effect of hub configuration is assessed by comparing the characteristic fan curves for the different hub configurations. To understand what causes the differences, a qualitative analysis is performed and then quantified by analysing velocity fields and blade loading.

6.1 Hub Configurations

Four different hub configurations were evaluated in this thesis. These are the: round hub, square hub, centre disk, and forward disk, as shown in Figure 6.1. These are abbreviated to R Hub, S hub, CD hub, and FD hub, respectively. The square hub is 170 mm long and centred about the centre of mass of the blade. The round hub uses the same geometry as the square hub but with the inclusion of a ball nose on the upstream side. The centre disk consists of an infinitely thin disk placed perpendicular to the flow direction, under the centre of mass of the blade, whereas the forward disk is placed underneath the leading edge of the blade.

Stellenbosch University https://scholar.sun.ac.za

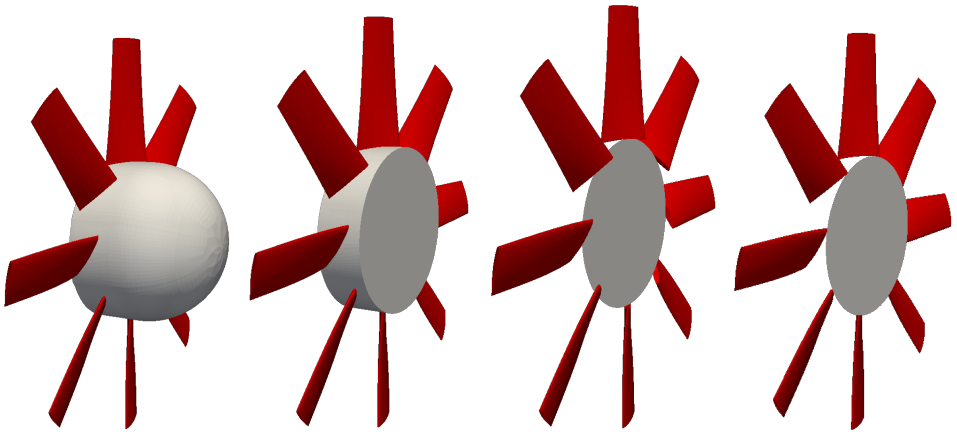

(a) R hub (b) S hub (c) CD hub (d) FD hub

Figure 6.1: Hub geometries

6.2 Fan Performance Comparison

Simulations were performed for volumetric flow rates of 10, 13, 16, and 19 m^3/s. At each flow rate, fan performance is measured using the total-to-static pressure rise, power consumption, and efficiency, as defined in Section 5.1

Curves of total-to-static pressure rise, shaft power, and efficiency over the chosen flow rates for the four different hub geometries are used to evaluate the effect of hub configuration on the performance of the B2a-fan. To quantify the differences between the hubs, the round hub is used as the datum and the difference between the remaining hubs and the round hub is plotted. This is so that the difference in performance of alternative hub configurations can be shown more clearly. These plots are shown in Figures 6.2 to 6.4. The full characteristic curve of each hub is shown in Appendix E along with numerical values for the performance at each operating point.

Stellenbosch University https://scholar.sun.ac.za

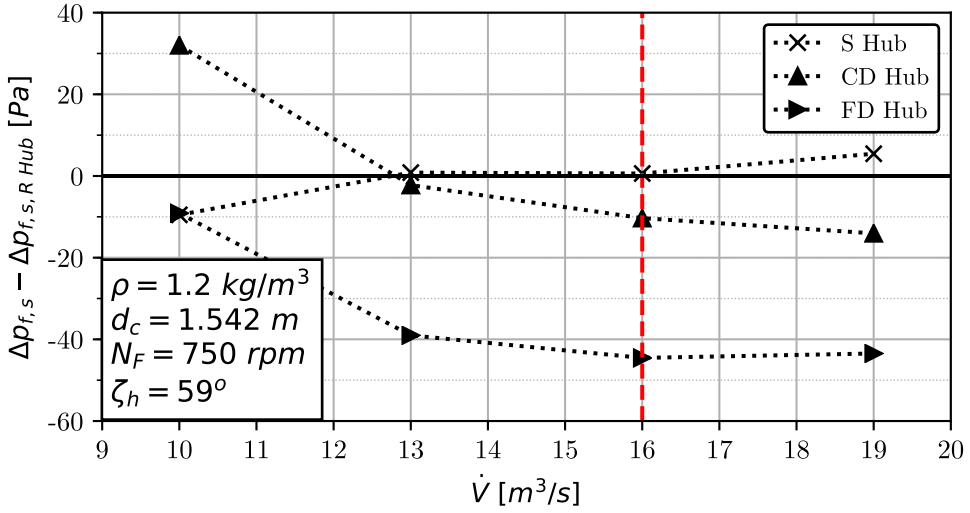

Figure 6.2: Hub comparison of total-to-static pressure rise

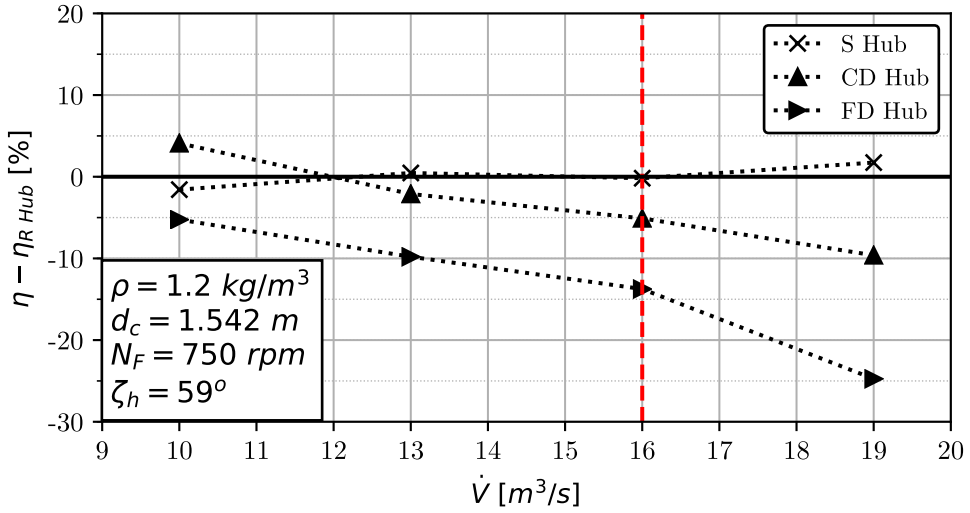

Figure 6.3: Hub comparison of total-to-static efficiency

Stellenbosch University https://scholar.sun.ac.za

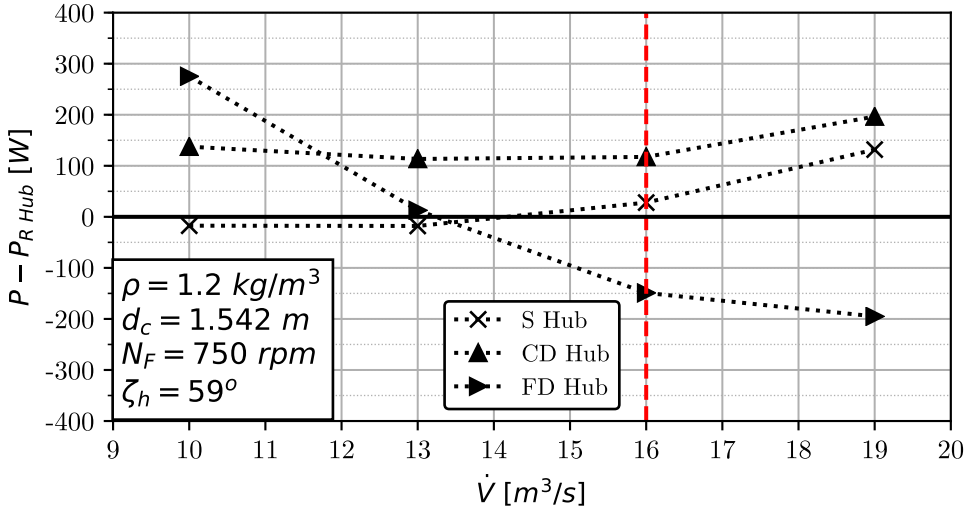

Figure 6.4: Hub comparison of power consumption

It is seen that at 13 and 16 m^3/s the total-to-static pressure rise and shaft power are comparable between the round and square hub. At $\dot{V} = 19\ m^3/s$, however, the square hub outperforms the round hub's total-to-static pressure rise by 5.4 Pa (9.5 %), resulting in a 1.8 % (5.1 % point) increase in efficiency as well. The inverse is true at $\dot{V} = 10\ m^3/s$, where lower total-to-static pressure rise and higher shaft power results in significantly lower efficiency.

The centre disk hub shows the opposite trend to the square hub in terms of total-to-static pressure rise. When compared to the round hub, an increase in pressure rise is seen as flow rate decreases. At $\dot{V} = 10\ m^3/s$, the total-to-static pressure rise improves by 32.0 Pa (8.4 %) while efficiency increases by 4.1 % (5.7 % point). As flow rate increases, the total-to-static pressure rise decreases, and the relative power consumption increases, leading to significantly lower efficiency at high flow rates. This trend matches up with the results obtained by Duesimi (2015).

When the disk is moved to the blade leading edge, the same trend is observed. The total-to-static pressure rise, however, is dramatically lower than with the centre disk hub throughout the entire range of flow rates. The decrease in total-to-static pressure rise ranges from 29.4 Pa to 41.1 Pa (10.0 % to 67.0 %) as the volumetric flow rate increases from 10 to 19 m^3/s. Instead of an increase in relative power consumption at higher flow rates, a decrease in relative power consumption is observed for the forward disk hub. Despite this, the efficiency overall is worse, due to its sensitivity to total-to-static pressure rise.

Stellenbosch University https://scholar.sun.ac.za

6.3 Qualitative Flow Analysis

To understand what is happening to the flow through the different configurations, a qualitative analysis is performed to investigate the flow structures around the hub. This is done by considering streamlines and contour plots to visualise the flow field.

Figures 6.5 to 6.8 show the meridional streamlines near the rotor region for the design point flow rate. Appendix F shows these streamlines at all four evaluated flow rates.

Figure 6.5 illustrates the ability of the bellmouth and round hub to effectively redirect the air from the open inlet into the rotor domain. This differs from the square hub of Figure 6.6 which exhibits a separation zone on the leading edge of the hub. Both the round and square hubs exhibit a downstream recirculation zone, which is blocked by the hub from entering the rotor region at $\dot{V} > 10$ m^3/s.

This is not the case for Figure 6.7 and Figure 6.8 which shows the downstream recirculating flow interacting with the blade in the disk hub geometries. This is more prominent for the forward disk hub, which has a larger downstream recirculation vortex and the vortex core is closer to the blade root. This effect, paired with the high radial flow in front of the disk, results in these configurations redirecting more of the flow towards the tip region.

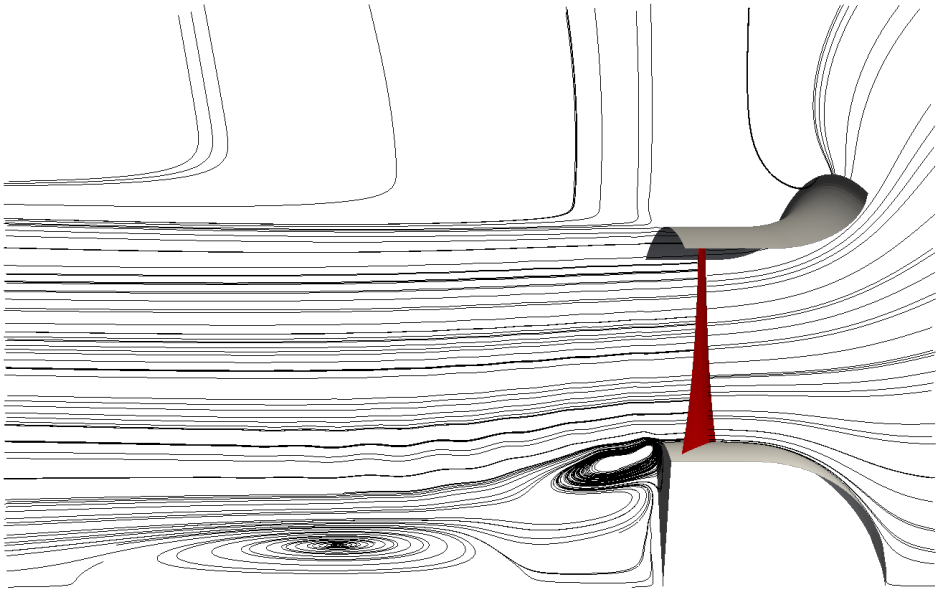

Figure 6.5: Meridional streamlines of the round hub at $\dot{V} = 16$ m^3/s

Stellenbosch University https://scholar.sun.ac.za

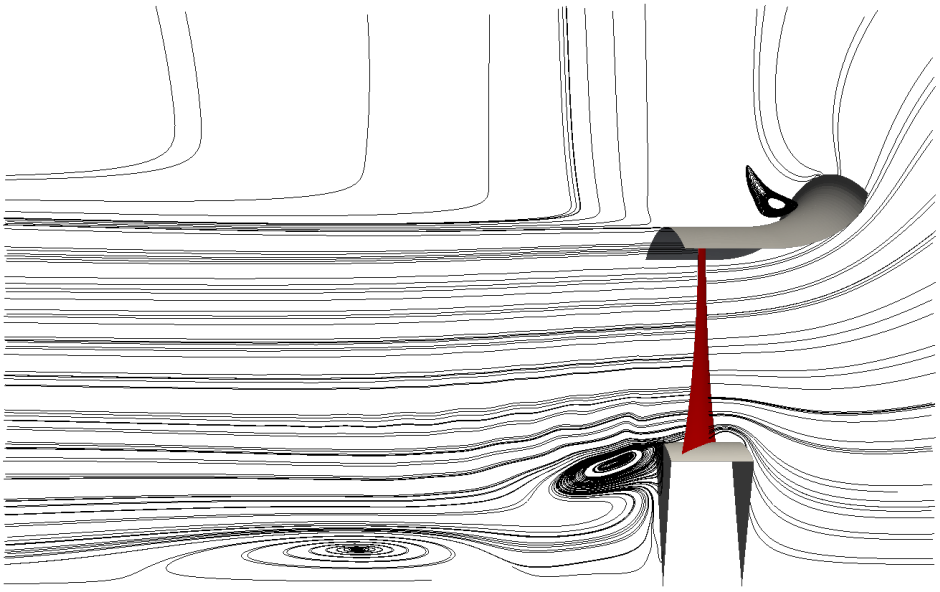

Figure 6.6: Meridional streamlines of the square hub at $\dot{V} = 16$ m^3/s

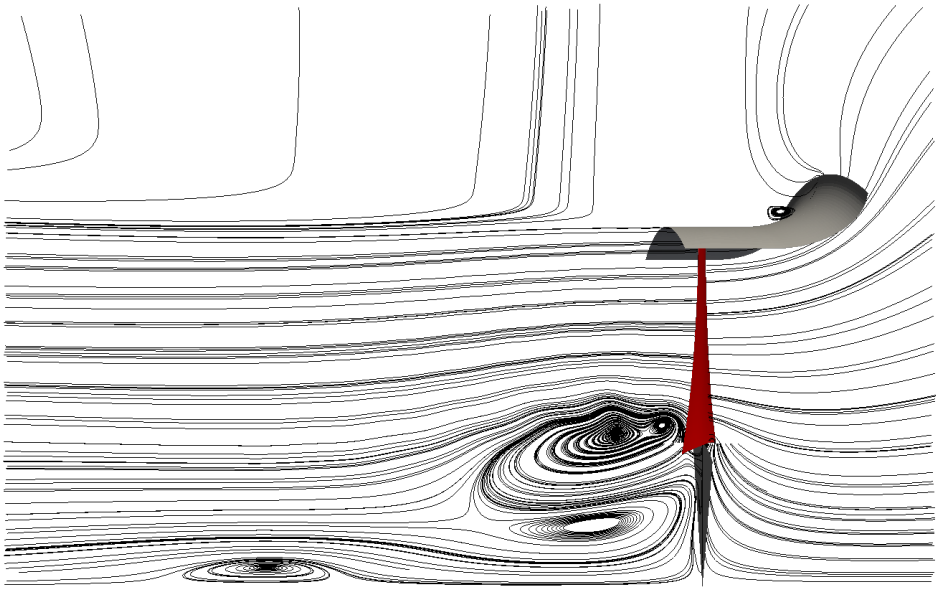

Figure 6.7: Meridional streamlines of the centre disk hub at $\dot{V} = 16$ m^3/s

Stellenbosch University https://scholar.sun.ac.za

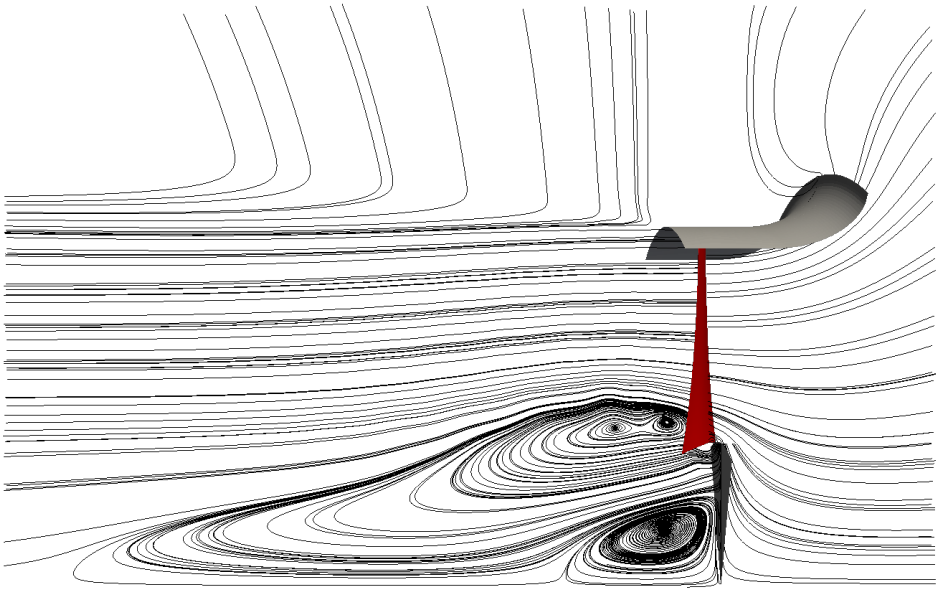

Figure 6.8: Meridional streamlines of the forward disk hub at $\dot{V} = 16$ m^3/s

The sharp corner of the square hub's leading edge forms a separation vortex. This is identifiable in Figure 6.6. In order to visualise the vortex, the λ_2 criterion is used. The λ_2 criteria uses the eigenvalues of the velocity gradient tensor to determine a vortex core (Jeong and Hussain, 1995). An isosurface of this is used in Figure 6.9 to show the vortex forming over the square hub leading edge at the design flow rate.

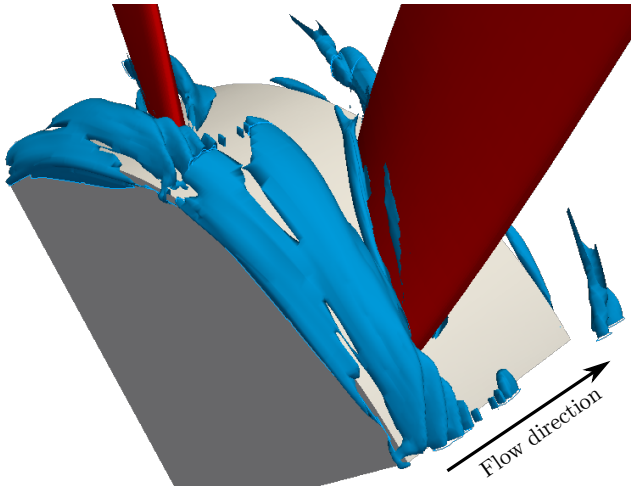

Figure 6.9: Vortex formation over square hub ($\lambda_2 = -6 \times 10^4$ isosurface)

Stellenbosch University https://scholar.sun.ac.za

The vortex spans less than 10 % of the blade span, and directly interacts with the leading edge on the blade suction side. The low pressure induced by the blade turns the vortex core in the axial direction near the trailing edge, resulting in the vortex interacting with the next blade's pressure side. The magnitude of the vortex and its interaction with the next blade row's pressure side grows as the volumetric flow rate increases.

A similar vortex is generated for the disk hub geometries. The vortex forms and rolls over the disk. Without a hub to reattach to, this vortex is stronger and interacts to a greater extent with the next blade's pressure side. This vortex is shown for the forward disk hub configurations at the design flow rate in Figure 6.10. Note: a larger λ_2 isosurface value is needed to present a legible image due to the stronger vortex.

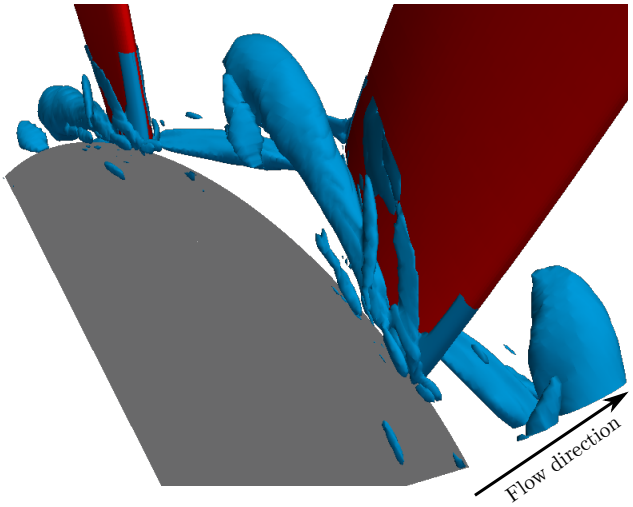

Figure 6.10: Vortex formation over forward-flat hub ($\lambda_2 = -2 \times 10^5$ isosurface)

6.4 Quantitative Flow Analysis

In order to quantify the flow structures in the rotor region, a quantitative analysis is performed. Up- and downstream evaluation planes are used in order to evaluate the flow and forces over the blade.

6.4.1 Evaluation Planes

Evaluation planes are placed a distance of 0.46 $ch_h = 0.085$ m from the blade centre, where ch_h is the blade chord length at the hub. This marks the inlet and

Stellenbosch University https://scholar.sun.ac.za

outlet of the rotor region and is shown in Figure 6.11. Subscripts 1 and 2 are used to denote a variable being considered on the upstream and downstream planes, respectively.

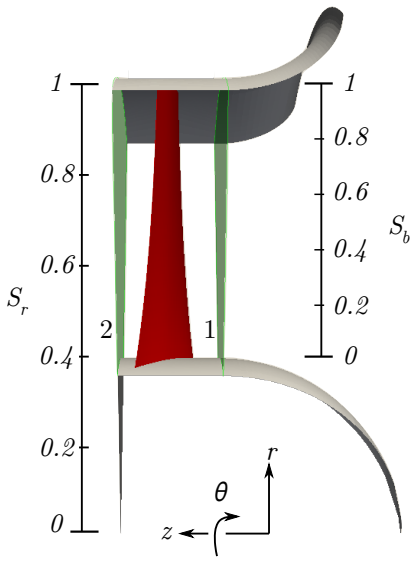

Figure 6.11: Flow characteristics evaluation planes

The flow characteristics are averaged in the circumferential direction. This represents the two-dimensional evaluation planes into one-dimensional lines in the spanwise direction. The spanwise direction is nondimensionalized by two means, shown in Equation 6.1. S_r represents the span fraction from the axis of rotation to the blade tip radius, while S_b represents the span fraction from the hub to tip.

$$\begin{aligned} S_r(r) &= \frac{r}{r_t} \\ S_b(r) &= \frac{r - r_h}{r_t - r_h}. \end{aligned} \tag{6.1}$$

6.4.2 Velocity Profiles

Figure 6.12 shows the velocity vectors considered in the results. Here, $\vec{V}$ represent the absolute velocity, $\vec{W}$ the relative velocity, and u the tangential blade speed. The blade speed can be defined at any radial location as $u = \omega r$, where ω is the rotational speed of the fan in rad/s.

Stellenbosch University https://scholar.sun.ac.za

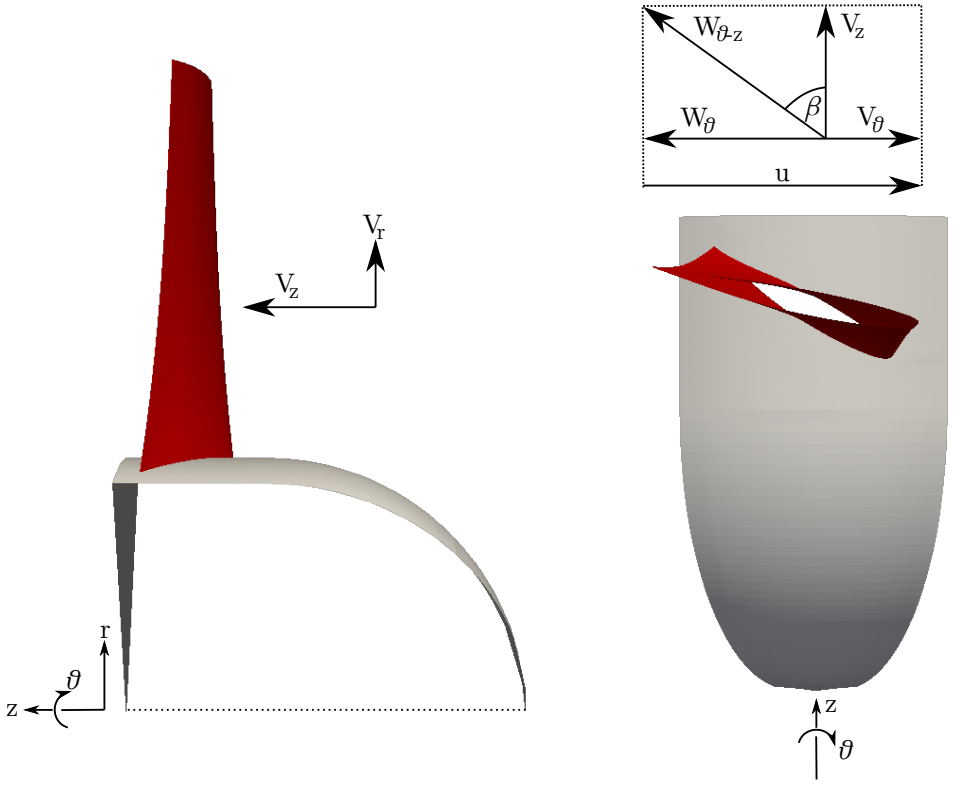

Figure 6.12: Velocity Vectors

Figures 6.13 to 6.16 shows the axial velocity profiles for all flow rates. The upstream axial velocity shows that the disk based geometries have a notable amount of flow passing below the blade root height. This effect is not as prominent in the forward disk hub configuration due to the disk restricting the flow from passing under the blade leading edge. This causes the axial velocity on the lower half of the blade span to be much less than that of the round and square hubs.

The velocity distribution for the round and square hubs on the upstream side appear very similar on the upper half of the blade span. However, the square hub displays reduced axial velocity very near the hub due to the vortex (shown in Figure 6.9) causing a low velocity zone. The axial velocity then spikes at the top of the vortex. This effect becomes more severe as the flow rate increases.

The downstream axial velocity distribution highlights the large amount of recirculation occurring for the disk hub configurations and is slightly more pronounced for the forward mounted configuration. This recirculating flow on the lower portion of the blade span causes higher axial velocity over the remainder of the blade span. The round and square hubs have very similar exit axial velocity profiles. This is likely due to the similarity in hub geometry

Stellenbosch University https://scholar.sun.ac.za

on the downstream half of the rotor region. Both demonstrate a uniform axial velocity over the blade span, with a slightly lower axial velocity on the lower half of the blade span at lower flow rates.

The up- and downstream axial velocity profiles for the round and square hubs are relatively constant (above $\dot{V} = 10\ \mathrm{m}^3/s$), which is expected from a fan based on a free-vortex design. When the disk hub configurations are used, a large discrepancy in the flow pattern is seen, demonstrating the impact that hub configurations could have on the expected flow field of the fan.

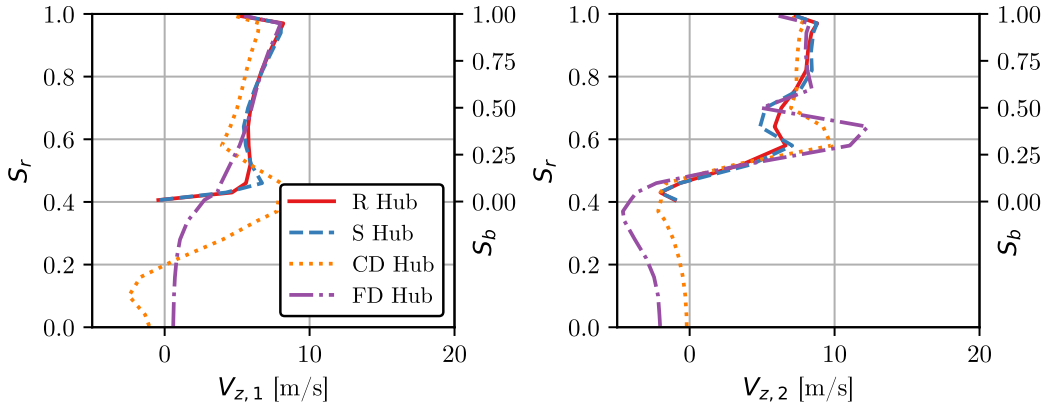

Figure 6.13: Circumferentially averaged axial velocity at $\dot{V} = 10\ \mathrm{m}^3/s$ Upstream (left) and downstream (right)

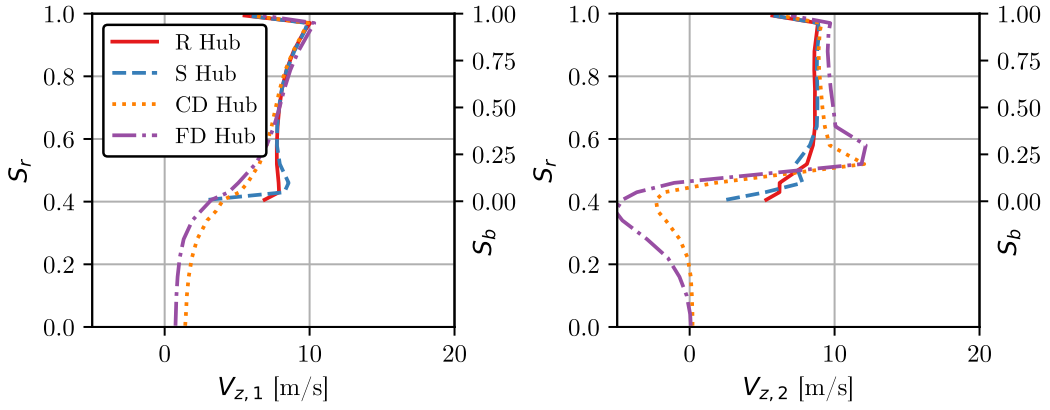

Figure 6.14: Circumferentially averaged axial velocity at $\dot{V} = 13\ \mathrm{m}^3/s$ Upstream (left) and downstream (right)

Stellenbosch University https://scholar.sun.ac.za

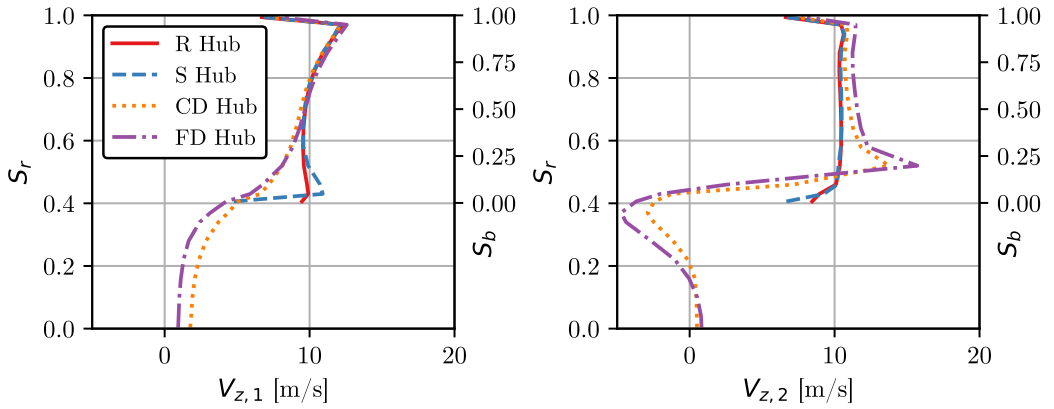

Figure 6.15: Circumferentially averaged axial velocity at $\dot{V} = 16$ m$^3/s$ Upstream (left) and downstream (right)

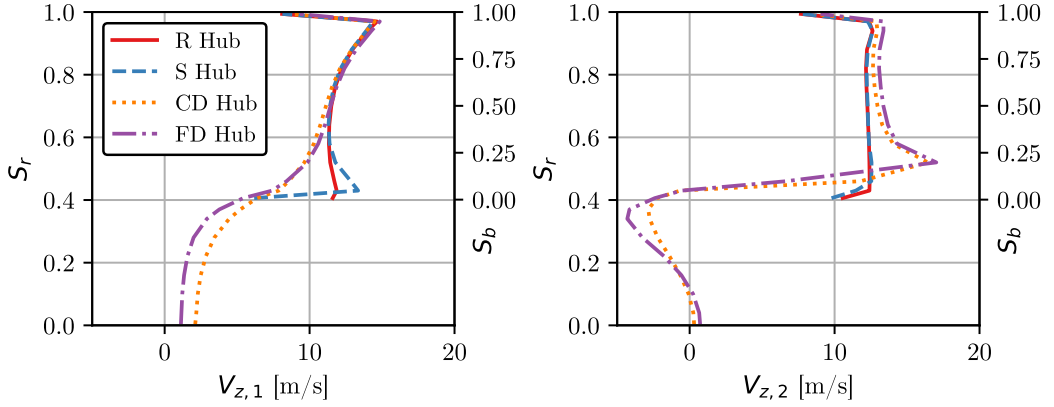

Figure 6.16: Circumferentially averaged axial velocity at $\dot{V} = 19$ m$^3/s$ Upstream (left) and downstream (right)

Figures 6.17 to 6.20 shows the tangential velocity profiles. The tangential component of velocity upstream of the blade is negligible for all the hub geometries. This is expected, as the incoming flow is modelled as being free from any swirling or crossflow effects.

At $\dot{V} = 10$ m$^3/s$, the inclusion of the recirculation vortex into the rotor region of the round and square hub become evident. Up to $S_b = 0.3$, a reduced tangential velocity component is observed for these geometries. This is due to the vortex removing the swirling component on the downstream flow.

Stellenbosch University https://scholar.sun.ac.za

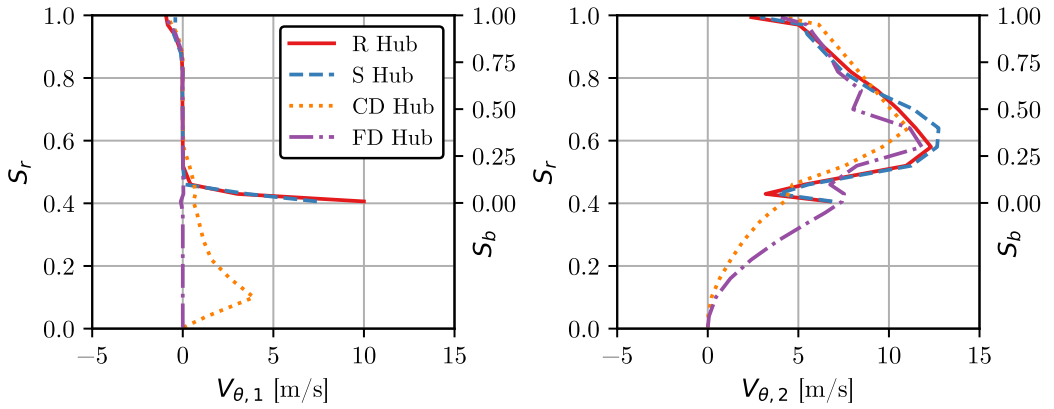

Figure 6.17: Circumferentially averaged tangential velocity at $\dot{V} = 10$ m$^3/s$. Upstream (left) and downstream (right)

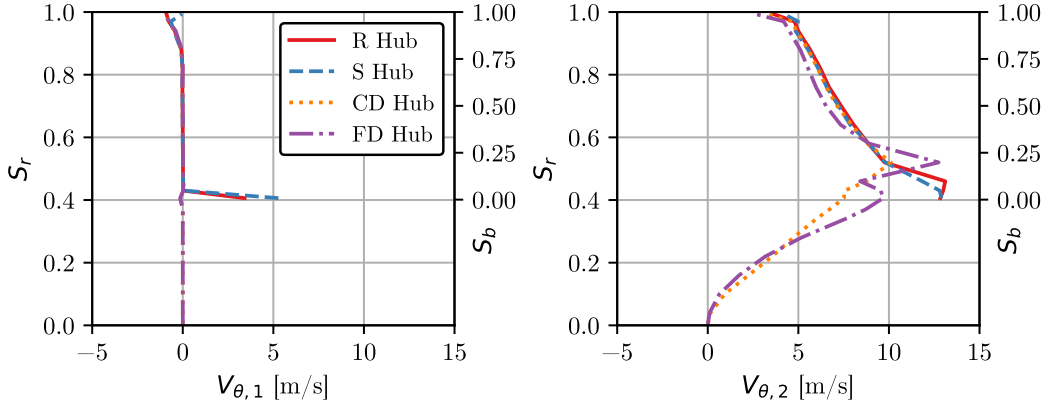

Figure 6.18: Circumferentially averaged tangential velocity at $\dot{V} = 13$ m$^3/s$. Upstream (left) and downstream (right)

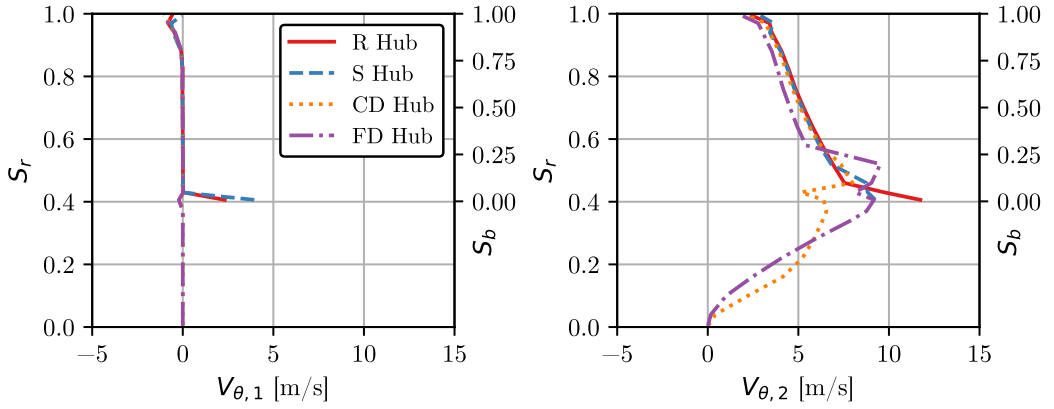

Figure 6.19: Circumferentially averaged tangential velocity at $\dot{V} = 16$ m$^3/s$. Upstream (left) and downstream (right)

Stellenbosch University https://scholar.sun.ac.za

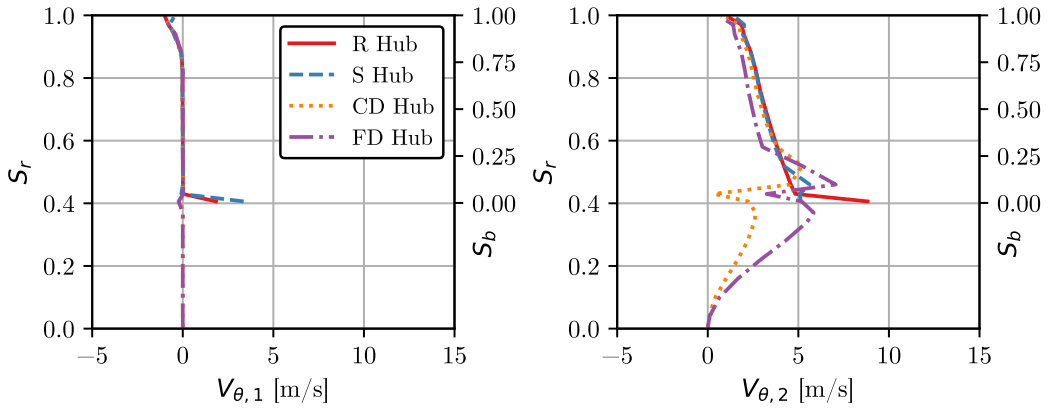

Figure 6.20: Circumferentially averaged tangential velocity at $\dot{V} = 19$ m$^3/s$. Upstream (left) and downstream (right)

Lewis (1996) outlines the use of Euler's turbomachinery equation. In the case of axial flow turbomachinery, this equation creates a direct correlation between pressure rise and the change in tangential velocity component. This correlation can be seen by the increase in the tangential velocity component as flow rate decreases. Furthermore, in the cases of the round and square hubs, the reduced tangential velocity component at $\dot{V} = 10$ m$^3/s$ corresponds with a reduction in fan performance.

Figures 6.21 to 6.24 shows the circumferentially averaged radial velocity profiles. The radial velocity component is often overlooked when analysing axial flow fans. However, radial flow has been seen to impact the performance of axial flow turbomachinery, as demonstrated by Himmelskamp (1947).

All hub configurations see a relatively small negative radial flow component on the upper half of the blade span at the inlet of the rotor region. This is due to the fan 'pulling' air from the open inlet via the bellmouth. Similarly, a positive radial flow component is seen at the inlet near the blade root. This is due to the redirection of flow from the hub region to the rotor region by the solid hub.

It can be seen that with the round hub, the negative radial component at the tip is larger than the positive radial velocity at the hub on the upstream evaluation plane above $\dot{V} = 10$ m$^3/s$. This coincides with Figures 6.13 to 6.16 which showed that the axial velocity at the tip is also higher than at the hub, implying preferential flow to the tip of the blade. Both the bellmouth and round hub turn the incoming air evenly, compared to the large radial flow spikes observed with other hub configurations. The square hub has a significantly greater radial velocity component at the inlet of the rotor region,

Stellenbosch University https://scholar.sun.ac.za

demonstrating the result of the air not being guided by the geometry. This is more pronounced at higher flow rates, where the sharp inlet causes an increase in radial flow velocity over the majority of the fan radius and generates a separation vortex as a result (shown in Figure 6.9).

This same effect is seen with the disk hub configurations. The largest radial flow is still seen at the root of the blade, however, the magnitude is much less than for the square hub.

The radial flow distribution at the exit of the rotor region is similar for the round and square hub configurations. Both exhibit a uniform profile for $\dot{V} = 13\ \mathrm{m}^3/s$ to $\dot{V} = 19\ \mathrm{m}^3/s$ with an average that shifts from positive to negative as the volumetric flow rate is increased, and is bounded by the no slip conditions on the shroud and hub. The reason for increased radial flow at lower flow rates is due to the recirculation zone behind the hub increasing in size. This deflects the air exiting the rotor region upwards. Due to the larger recirculation zone, the disk hub geometries have larger radial flow velocities. This is clearly shown in Figures 6.7 and 6.8 where the downstream streamlines are deflected towards the upper portion of the blade span. Furthermore, the evaluation plane intersects the vortex, causing a large sinusoidal pattern to develop on the lower half of the span. This is also the case for the round and square hub configurations at $\dot{V} = 10\ \mathrm{m}^3/s$.

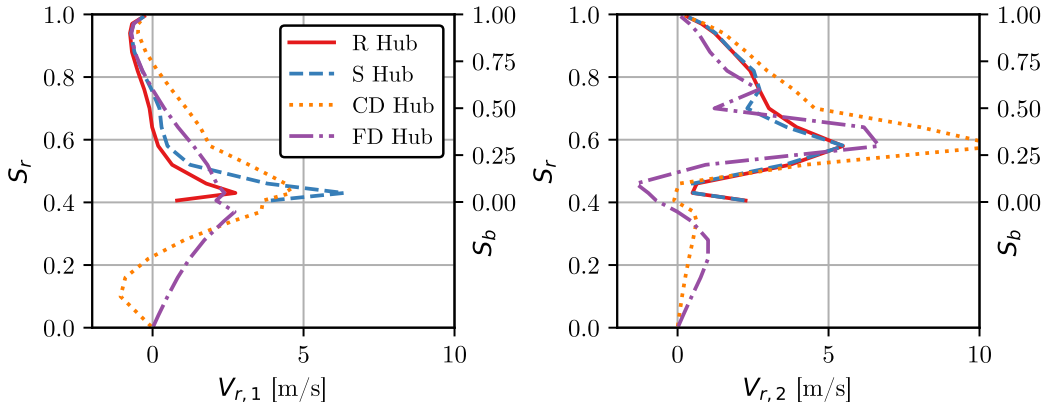

Figure 6.21: Circumferentially averaged radial velocity at $\dot{V} = 10\ \mathrm{m}^3/s$. Upstream (left) and downstream (right)

Stellenbosch University https://scholar.sun.ac.za

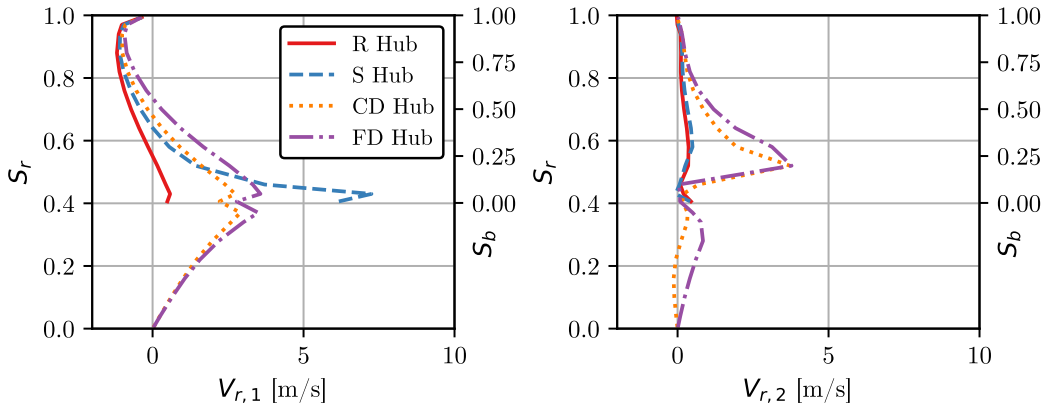

Figure 6.22: Circumferentially averaged radial velocity at $\dot{V} = 13$ m$^3/s$. Upstream (left) and downstream (right)

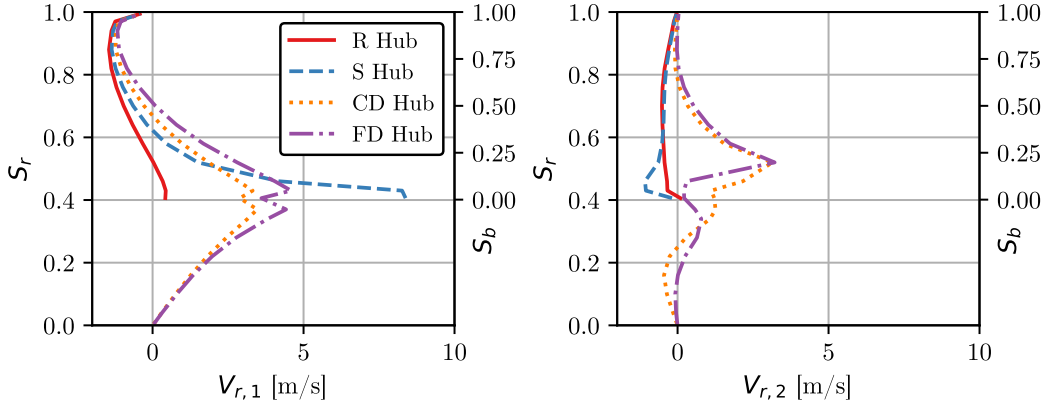

Figure 6.23: Circumferentially averaged radial velocity at $\dot{V} = 16$ m$^3/s$. Upstream (left) and downstream (right)

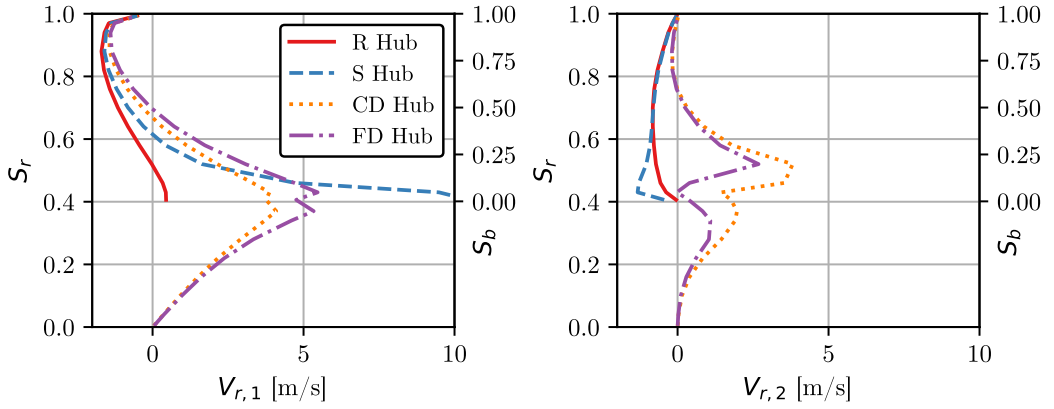

Figure 6.24: Circumferentially averaged radial velocity at $\dot{V} = 19$ m$^3/s$. Upstream (left) and downstream (right)

Stellenbosch University https://scholar.sun.ac.za

6.5 Blade Force Analysis

With the flow characteristics up- and downstream of the rotor region assessed, the flow over the blade is considered. The lift and drag forces generated by the blade is the primary mechanism for generating pressure rise (Thiart and von Backström, 1993). Consequently, there is an interest in determining the lift and drag forces produced by the blade. Based on two-dimensional aerofoil theory, the force on an aerofoil is nondimensionalized using the velocity crossing over it, the planform area, and the fluid density (ρ). This nondimensional force is broken up into the two components, lift (F_L) and drag (F_D), and corresponding two force coefficients, C_L and C_D. These lift and drag coefficients are generally a function of the fluid Reynolds number and angle of attack.

The three-dimensional blade used for the B2a-fan is considered at radial slices, which simplifies the blade into a two-dimensional aerofoil. The velocity and force vectors for such a blade section are shown in Figure 6.25. It can be seen that the average relative velocity that the blade experiences ($W_{\theta-Z,\infty}$) is a combination of the average axial velocity, and the average relative tangential velocity.

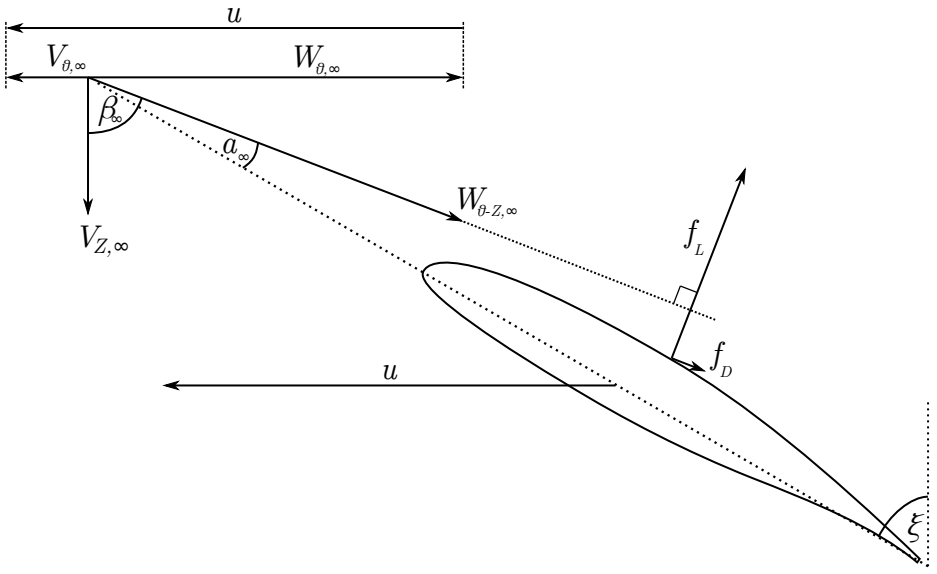

Figure 6.25: Velocity and force vectors on a two-dimensional section of the blade

The crossflow direction is defined from the axial direction using the average relative flow angle β_∞. Similarly, the blade angle is defined from the axial

Stellenbosch University https://scholar.sun.ac.za

direction in Equation 3.2 as ξ. The angle of attack, α_∞, is defined as the angle between the average relative flow angle and the aerofoil chord line:

$$\alpha_\infty = \beta_\infty - \xi. \tag{6.2}$$

The force vector can be determined by calculating the line integral of the pressure multiplied by the normal vector over the blade surface, and adding the wall shear component:

$$\vec{f} = \oint \left[p \cdot \vec{N} + \mu \left(\frac{d\vec{V}}{dy} \right)_{y=0} \right] dl \tag{6.3}$$

where $\vec{N}$ represents the surface normal vector. It is noted that this is not a true force, but a force per unit distance (thus using a lower case f) as it is integrated over length, and not area. This results in a force vector with known components in the r-θ-z directions. A coordinate transformation needs to be done in order to convert these forces into a lift and drag direction:

$$\begin{aligned} f_L &= -f_\theta \ \cos\beta_\infty + f_Z \ \sin\beta_\infty \\ f_D &= -f_\theta \ \sin\beta_\infty - f_Z \ \cos\beta_\infty \end{aligned} \tag{6.4}$$

From this, the lift and drag coefficients can be defined as

$$\begin{aligned} C_L &= \frac{2 \ f_L}{\rho \ ch \ W_{\theta-Z,\infty}^2} \\ C_D &= \frac{2 \ f_D}{\rho \ ch \ W_{\theta-Z,\infty}^2} \end{aligned} \tag{6.5}$$

where the local chord length (ch) is used instead of planform area, as the force is already a per unit thickness quantity.

Given that the analysis is done for a two-dimensional aerofoil section, XFoil may be used for comparison. XFoil is an open-source panel code that is able to solve the boundary layer flow over a two-dimensional aerofoil. Within the current thesis, the analysis done on the blade loading of the B2a-fan is compared to a two-dimensional equivalent case using XFoil. This is done by considering the Reynolds number and angle of attack at various radial locations on the B2a-fan blade and inputting this data into XFoil. An automated Python code written by Erfort *et al.* (2017) is used in order to interface with XFoil. Only the data from the round hub case is considered, as this forms the datum used for comparison.

Since the lift forces expected along an aerofoil is a function of the angle of attack, this angle is assessed across the blade span. This is shown for all four flow rates in Figure 6.26.

Stellenbosch University https://scholar.sun.ac.za

It can be seen how the reduced axial velocity near the blade root causes a very high angle of attack for the disk hub configurations. This is followed by a rapid reduction in angle of attack, to a minimum occurring between 10 and 20 % of the blade span. The location of this minimum increases in span as the flow rate decreases. A similar trend is observed for the square hub geometry, however, the magnitude is more consistent between flow rates. Lastly, the round hub has a fairly linear distribution of the angle of attack along the span, with a slight decrease with an increase in span.

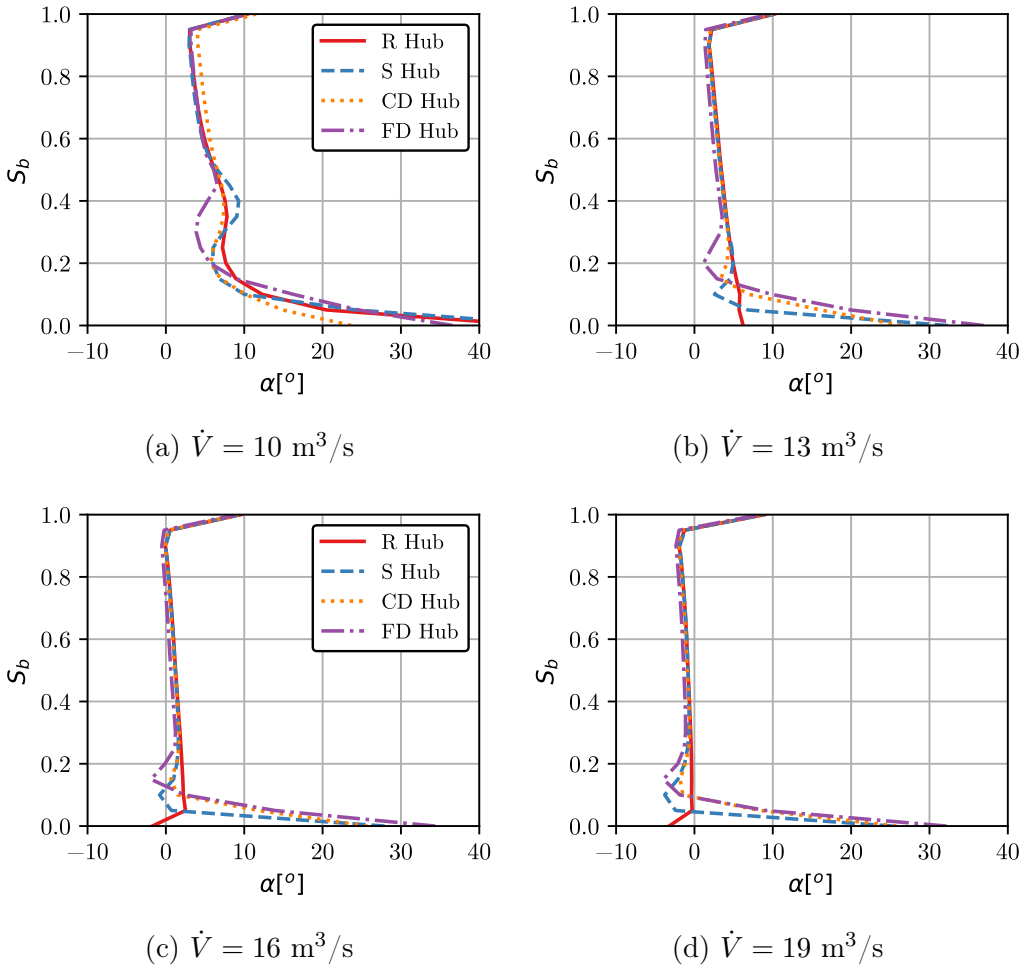

(a) $\dot{V} = 10$ m^3/s (b) $\dot{V} = 13$ m^3/s

(c) $\dot{V} = 16$ m^3/s (d) $\dot{V} = 19$ m^3/s

Figure 6.26: Averaged angle of a attack in rotor region at a) $\dot{V} = 10$ m^3/s, b) $\dot{V} = 13$ m^3/s, c) $\dot{V} = 16$ m^3/s, d) $\dot{V} = 19$ m^3/s

These trends can be seen in the axial velocity plots of Figures 6.13 to 6.16. It is seen that the disk and square hub geometries have a much lower axial velocity at the blade root, which would result in a higher angle of attack. The axial

Stellenbosch University https://scholar.sun.ac.za

velocity rapidly increases radially, causing a decrease in angle of attack. The square hub's axial velocity increases with radius on the upstream side which is due to the separation vortex occurring on the leading edge of the hub. The disk hub configurations' peak axial flow occurs on the downstream side and is due to the downstream recirculation creating a nozzle like effect.

In a similar analysis, Louw (2015) found that the drag force is often an order of magnitude smaller than the lift force. As such, the lift force is the primary factor in both generating pressure rise as well as increasing shaft power. Consequently, only the lift force is assessed in detail.

The spanwise lift coefficient distribution shown in Figure 6.27 correlates to the angle of attack distribution. At all flow rates, the square hub's lift is slightly less than that of the round hub, down to a span of $S_b = 0.1$. Below this span, the lift coefficient distribution is slightly higher than that of the round hub. As the flow rate increases the difference at mid span decreases.

At $\dot{V} > 10$ m^3/s, the disk hub configurations show lift coefficients that are slightly higher than for the square and round hub at $S_b < 0.1$ (except close to $S_b = 0$). For $S_b > 0.1$ however, both the disk hubs produce less lift than the round and square hubs, with the forward disk producing significantly less lift. The opposite is true at $\dot{V} = 10$ m$^3/s$, where the centre disk transitions from a higher to a lower lift coefficient at $S_b = 0.3$. This is identified as being the radial distance that the recirculation vortex formed behind the round and square hub terminates.

Also shown in Figure 6.27 is the lift coefficient data from XFoil. A strong correlation can be seen at higher volumetric flow rates. As flow rate decreases, a discrepancy develops near the hub region. The attained coefficient of lift exceeds that which is predicted by XFoil. This is due to the high angles of attack occurring in the hub region which would result in flow separation of the blade. The Coriolis effects described by Himmelskamp (1947) results in this not occurring as early as predicted with purely two-dimensional theory.

Stellenbosch University https://scholar.sun.ac.za

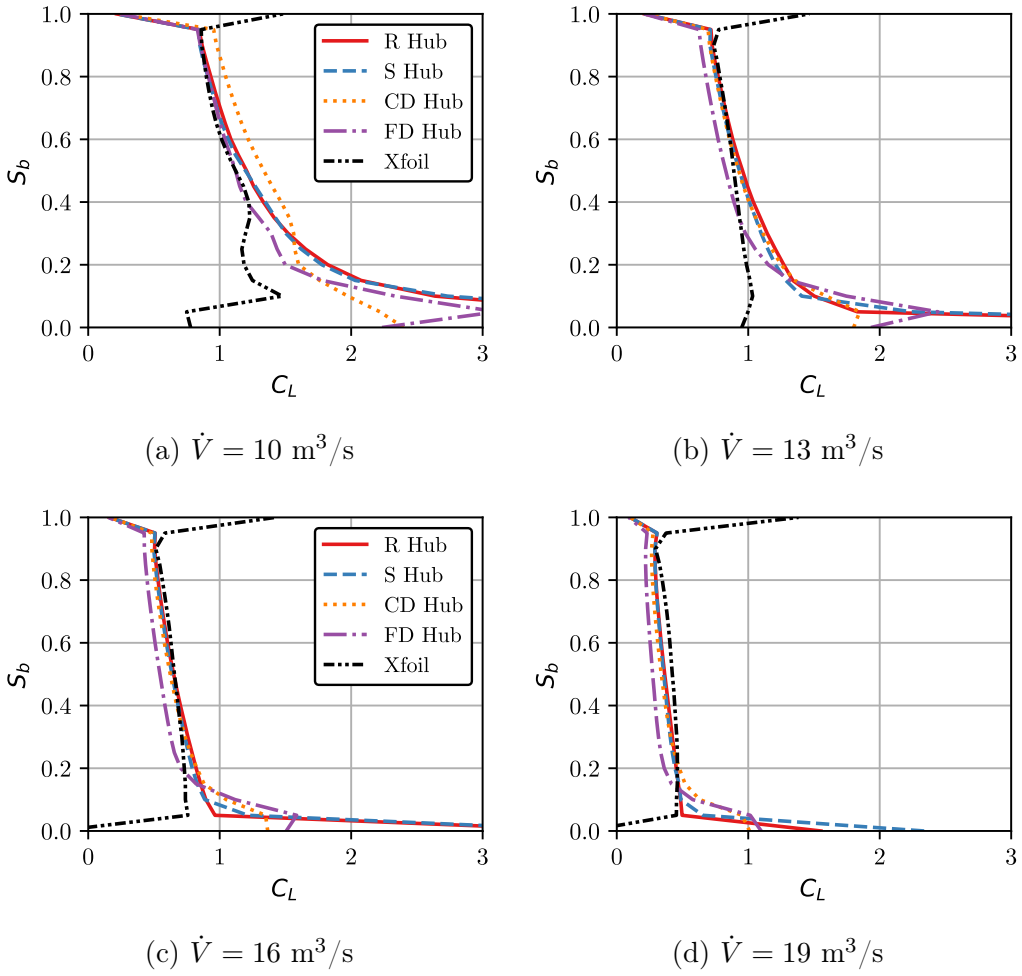

(a) $\dot{V} = 10$ m^3/s

(b) $\dot{V} = 13$ m^3/s

(c) $\dot{V} = 16$ m^3/s

(d) $\dot{V} = 19$ m^3/s

Figure 6.27: Spanwise lift coefficient of blade at a) $\dot{V} = 10$ m$^3/s$, b) $\dot{V} = 13$ m$^3/s$, c) $\dot{V} = 16$ m$^3/s$, d) $\dot{V} = 19$ m$^3/s$

6.6 Blade Surface Pressure

To assess how the lift forces on the blades are generated, the blade surface pressure (BSP) distributions can be evaluated. This shows where the loading is located along the blade chord, allowing for a better understanding of the interaction between the mean flow and blade. Five radial stations were evaluated (from $S_b = 0.1$ to 0.9); however, the difference in pressure distribution between the different hub configurations became negligible away from the hub. As such, only the lower two radial stations are discussed in this chapter, while all radial station results are shown in Appendix D.

Stellenbosch University https://scholar.sun.ac.za

Figures 6.28 to 6.31 show the coefficient of pressure distribution over the blade chord at two radial stations for the four evaluated flow rates. The coefficient of pressure non-dimensionalizes the pressure to the vector-average relative flow velocity, as shown in Equation 6.6. This is used to compare the loading over the different relative blade velocities experienced in the spanwise direction.

$$Cp = \frac{p_s}{\frac{1}{2}\rho W^2_{\theta-Z,\infty}} \tag{6.6}$$

A large change in the suction side distribution can be seen between the different configurations at $S_b = 0.1$. The disk hub configurations exhibit a smaller suction pressure between leading edge and midspan ($x/ch = 0.1$ to 0.5), but a larger suction pressure nearing the trailing edge ($x/ch = 0.6$ to 1.0) forming an 'S' shaped distribution compared to the more linear distribution of the round and square hubs. This effect is most prominent on the forward disk hub and at higher flow rates. The square hub exhibits an almost linear pressure distribution, with exception to $\dot{V} = 10$ m$^3/s$, decreasing from the minimum pressure point to the trailing edge. The increased suction pressure near the leading edge coincides with the location where the separation vortex of Figure 6.9 interacts with the blade. This suggests that the interaction between the vortex and the blade causes the pressure distribution to create a more even blade loading.

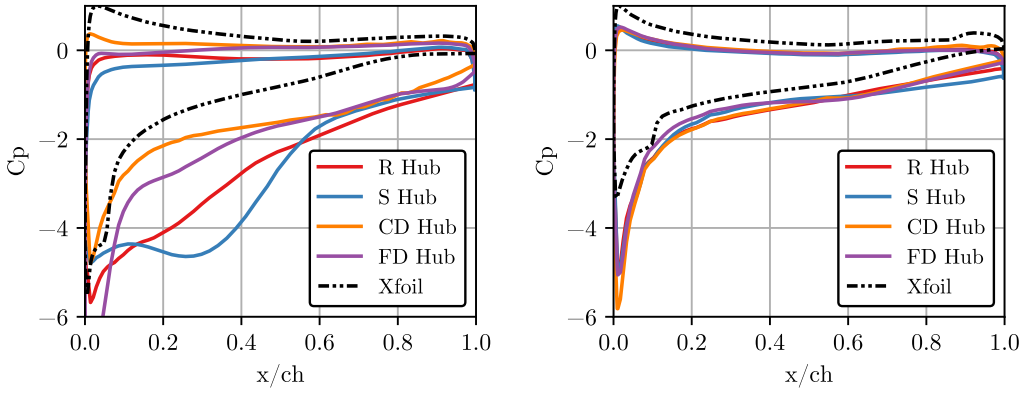

(a) $S_b = 0.1$ (b) $S_b = 0.3$

Figure 6.28: Blade surface pressure at $\dot{V} = 10$ m^3/s at $sb =$ a) 0.1, b) 0.3

Stellenbosch University https://scholar.sun.ac.za

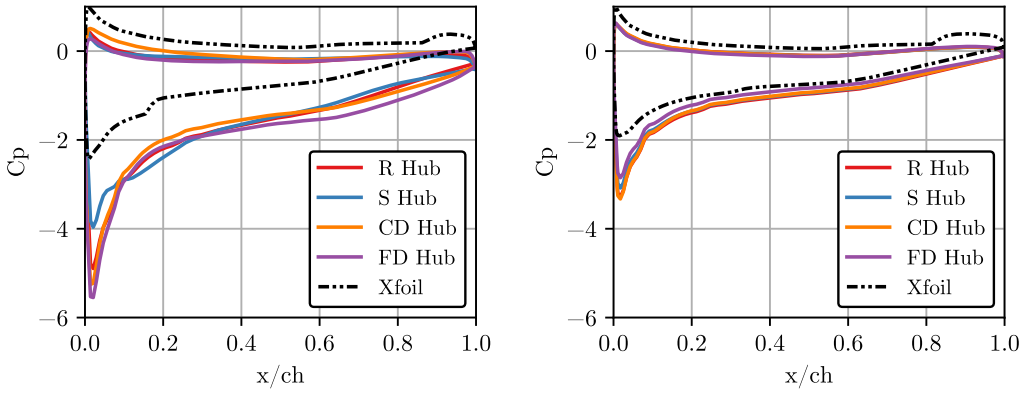

(a) $S_b = 0.1$ (b) $S_b = 0.3$

Figure 6.29: Blade surface pressure at $\dot{V} = 13$ m^3/s at $sb =$ a) 0.1, b) 0.3

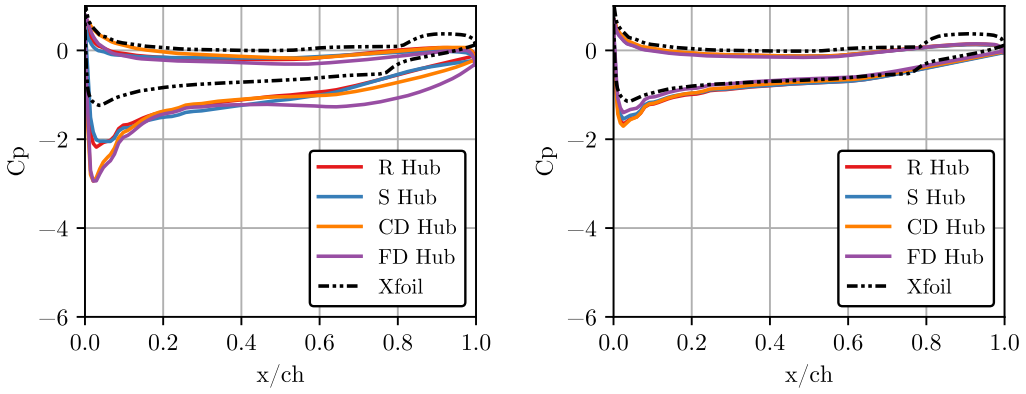

(a) $S_b = 0.1$ (b) $S_b = 0.3$

Figure 6.30: Blade surface pressure at $\dot{V} = 16$ m^3/s at $sb =$ a) 0.1, b) 0.3

Stellenbosch University https://scholar.sun.ac.za

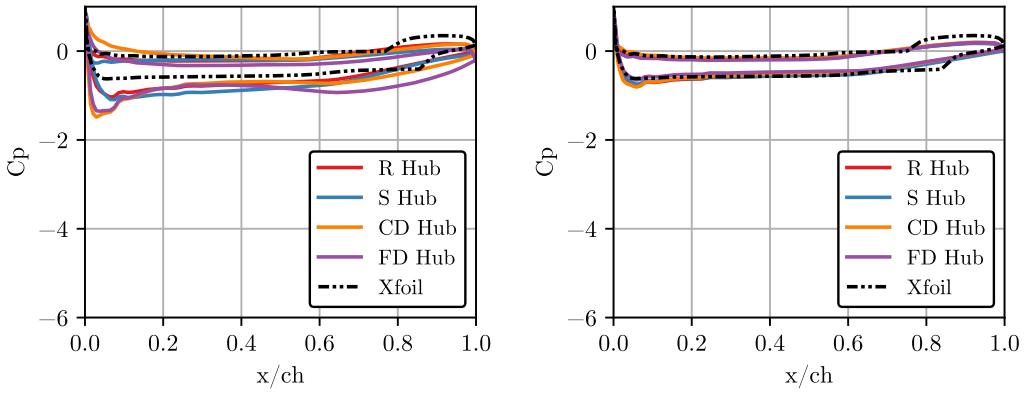

(a) $S_b = 0.1$ (b) $S_b = 0.3$

Figure 6.31: Blade surface pressure at $\dot{V} = 19$ m^3/s at $sb =$ a) 0.1, b) 0.3

At $\dot{V} = 10$ m$^3/s$, a large spike occurs in the BSP for the square and round hubs at $0 > x/ch > 0.6$. This was identified to be due to excessive angles of attack resulting in large blade loading profiles.

Once again, XFoil data found using the round hub's angle of attack and Reynolds number is also compared to assess the difference in BSP. Figures 6.28 to 6.31 support Figure 6.27 in illustrating the difference in prediction and attainment of BSP. The largest difference is seen on the blade suction side, which further supports the notion that the flow around the rotating blade is better able to stay attached than predicted.

6.7 Concluding Remarks

Section 6.2 shows that hub configuration can have a significant impact on fan performance and is a function of the volumetric flow rate. This implies that there are complex interactions between the hub configuration and the fan's operation. A thin disk hub was found to improve the low volumetric flow rate performance when compared to the round hub, but larger losses are associated near the design point. In contrast, a thicker square hub geometry marginally improves performance at above design point flow rates. However, it underperforms compared to the round hub at lower volumetric flow rates.

By analysing the streamlines through the meridional plane in Section 6.3, the impact that hub configuration has on the flow regime became clear. A separation vortex on the leading edge of the square hub can be seen, and

Stellenbosch University https://scholar.sun.ac.za

a large recirculation zone was identified downstream of the blade for the disk hubs. Section 6.4 quantified these effects by assessing the velocity fields, which shows how the recirculation zone behind the disk hub configurations cause a tip preferential in flow, leading to an increase in work done to the flow, illustrated by Figure 6.27a. This resulted in an improved performance at lower volumetric flow rates. It also gives reason to the reduction in performance at higher flow rates, which is due to the poor flow distribution on the lower portion of the blade and the losses associated with the recirculation zone.

The similarity in impact of the round and square hubs imply that the exclusion of the hemispherical nose fairing from the square hub has a very small effect on the flow over the fan. This is due to the changes in flow between the two hub configurations being localised near the blade root. The majority of the work imparted onto the flow is done by the tip section of the blade. This means that small changes near the hub would have a small impact on performance.

The movement of the downstream recirculation zone into the rotor region is seen at $\dot{V} = 10$ m$^3/s$ for the round and square hub. This leads to a reduction in the downstream swirl and an increase in losses, resulting in deleterious performance.

Section 6.5 shows the lift forces resulting from the differing angles of attack, as well as the loading on the blade at two radial locations. This illustrates how the separation vortex forming over the square hub creates a preferable suction side pressure distribution and thereby increases the lift generated in this region.

A comparison to two-dimensional data gathered from XFoil illustrates the difference in predicted blade pressure distribution and attained three-dimensional pressure distribution. The comparison indicates that two-dimensional data is insufficient for accurate prediction of the performance of the three-dimensional blade. This agrees with the work of Himmelskamp (1947) and Gur and Aviv (2005) on the impact of the Coriolis effect in turbomachinery.

It is further noted that due to the low velocities near the hub region, the averaged angle of attack through the rotor region may misrepresent the true angle of attack over the blade. This may gave further reason for the large discrepancy between the XFoil results and the three-dimensional results.

Stellenbosch University https://scholar.sun.ac.za

Chapter 7

Conclusion and Recommendations

This chapter concludes the work done within this thesis. In doing so, the original research objectives that formed the thesis are assessed. The chapter concludes by suggesting further research that could follow from this thesis to further expand the body of knowledge.

7.1 Methodology

One of the objectives of this study was to perform a fluid simulation of an air-cooled condenser (ACC) fan using open-source numerical modelling. This was accomplished by making use of a combination of OpenFOAM and Python. OpenFOAM's blockMesh utility, in combination with Python, was used to construct the computational mesh. The meshing procedure considered primarily skewness and non-orthogonality for mesh quality measurement, and resulted in a mesh with a satisfactory quality. The Python code allowed a choice of three different hub geometries; a round hub, a square hub, and a hubless mesh. The *createBaffles* utility could then be used to generate a thin disk at any axial location within the hubless mesh to create an infinitely thin disk hub.

In order to solve the partial differential equations required for fluid simulation, OpenFOAM was used. A convergence criterion was set, and met by all simulations except for the round, square, and centre disk hubs at $\dot{V} = 10\ \mathrm{m}^3/s$. By using transient simulations, the round and square hubs were successfully modelled. The convergence criteria had to be relaxed for the centre disk hub due to large volume ratios at the nonconforming mesh region.

Validation was performed for the round hub, due to the availability of experimental results for this configuration. Good agreement was found at the design point, but the total-to-static pressure rise and efficiency was found to

Stellenbosch University https://scholar.sun.ac.za

follow a steeper curve than the experimental results. Despite this, a reasonable agreement was found when comparing blade surface pressure measurements.

7.2 Findings

Four hub configurations were compared; a round hub, a square hub, a centre disk hub, and a forward disk hub. The round hub was used as a reference due to the thesis's aim of determining the possibility of an alternative configuration.

It was found that the square hub formed a separation vortex at the leading edge surface of the hub, which interacts with the leading edge of the blade near the hub. The vortex improves the pressure distribution of the suction side of the blade. This manifests as a higher lift generated near the hub. As the flow rate increases, the magnitude of this impact increases. This leads to improved performance at higher flow rates. Losses associated with the vortex decreases the performance at lower flow rates, and as such, this hub configuration is found to be favourable at higher flow rates and comparable to the round hub near the design point flow rate.

The disk hub configurations moves the downstream recirculation vortex closer to the blade. This results in poor airflow on the lower portion of the blade surface and leads to a decrease in performance. This is further impacted by a large vortex rolling over the disk and interacting with the next blade's pressure side. As flow rate decreases, the magnitude of the recirculation increases, causing a tip preferential of the flow. This increases the work imparted on the flow. Furthermore, the round and square hubs formed a large enough recirculation vortex at $\dot{V} = 10\ \mathrm{m}^3/s$ to reduce the swirl on the lower portion of the blade leading to a reduction in performance at this flow rate.

7.3 Recommendations for Future Work

This thesis succeeded in modelling a $\frac{1}{8}^{\mathrm{th}}$ fan rotor using only open-source software. Validation of the simulation could, however, be improved. It was found during initial simulations that even a small number of poor quality cells could have a large impact on the final result. Furthermore, some mesh based anomalies could be identified in the flow, especially for the nonconformal mesh of the disk hub configurations. As such, a more capable meshing software would be recommended for future work to save time and increase the reliability of the results.

Stellenbosch University https://scholar.sun.ac.za

The present work indicates that hub configuration impacts the flow around a fan to a significant extent. This results in a variance of the characteristic curves obtained from the fan. An experimental study of these effects should be carried out to validate these findings.

A comparison between a forward disk and a centre disk hub showed the superior performance of the latter configuration. An investigation into moving the disk hub further downstream should be investigated. Furthermore, the effect of the axial length of the square and round hubs should be investigated to assess the parameter's impact on performance.

The present study only considered the B2a-fan. The effect that hub configuration has on alternative fans could vary significantly. It is suspected that hub-to-tip ratio may alter the importance of various fluid structures. As such, the impact of hub configurations on alternative fans should be investigated.

Stellenbosch University https://scholar.sun.ac.za

List of References

Angelini, G., Bonanni, T., Corsini, A., Delibra, G., Tieghi, L. and Volponi, D. (2017). Optimization of an axial fan for air cooled condensers. *Energy Procedia*, vol. 126, pp. 754–761. ISSN 18766102.

Araujo, P.P., Luiz, A. and Rezende, T. (2017). Comparison of Turbulence Models in the Flow over a Backward-Facing Step. *International Journal of Engineering Research & Science*, vol. 3, no. 11, pp. 88–93.

Augustyn, O.P. (2013). *Experimental and numerical analysis of axial flow fans.* Master's thesis, Stellenbosch University.

Beiler, M.G. and Carolus, T.H. (1999). Computation and Measurement of the Flow in Axial Flow Fans With Skewed Blades. *Journal of Turbomachinery*, vol. 121, no. 1, p. 59. ISSN 0889504X.

Bern, M. and Plassmann, P. (1999). Mesh Generation. *Handbook of Computational Geometry.*

Bruneau, P.R.P. (1994). *The design of a single rotor axial flow fan for a cooling tower application.* Master's thesis, Stellenbosch University.

Chandar, D.D. and Gopalan, H. (2016). Comparative Analysis of the Arbitrary Mesh Interface(AMI) and Overset Methods for Dynamic Body Motions in OpenFOAM. In: *46th AIAA Fluid Dynamics Conference*, June.

Corsini, A., Delibra, G. and Sheard, A.G. (2013). A critical review of computational methods and their application in industrial fan design. *ISRN Mechanical Engineering*, vol. 2013, no. 327. ISSN 20905122.

Corsini, A. and Rispoli, F. (2004). Using sweep to extend the stall-free operational range in axial fan rotors. *Proceedings of the Institution of Mechanical Engineers, Part A: Journal of Power and Energy*, vol. 218, no. 3, pp. 129–140. ISSN 09576509.

Downie, R.J., Thompson, M.C. and Wallis, R.A. (1993). An Engineering Approach to Blade Designs for Low to Medium Pressure Rise Rotor-Only Axial Fans. *Experimental Thermal and Fluid Science*, vol. 6, no. 4, pp. 376–401.

Stellenbosch University https://scholar.sun.ac.za

Duesimi, L. (2015). Determining the Effect of Hub Configuration on Axial Flow Fans. Tech. Rep., Stellenbosch University.

Erfort, G., von Backström, T.W. and Venter, G. (2017). Numerical optimisation of a small-scale wind turbine through the use of surrogate modelling. *Journal of Energy in Southern Africa*, vol. 28, no. 3, pp. 79–91. ISSN 1021447X.

Estevadeordal, J., Gogineni, S., Copenhaver, W., Bloch, G. and Brendel, M. (2000). Flow field in a low-speed axial fan: A DPIV investigation. *Experimental Thermal and Fluid Science*, vol. 23, no. 1-2, pp. 11–21. ISSN 08941777.

Ferziger, J.H. (2002). *Computational methods for fluid dynamics*. 3rd edn. Springer, Berlin. ISBN 3540420746.

Gur, O. and Aviv, R. (2005). Propeller Performance at Low Advance Ratio. *Journal of Aircraft*, vol. 42, no. 2, pp. 435–441. ISSN 0021-8669.

Himmelskamp, H. (1947). *Profile Investigations on a Rotating Airscrew*. ARC-10856. Ministry of Aircraft Production.

ISO 5801 (2007). *ISO 5801:2007: Industrial fans - Performance testing using standardized airways*, vol. 3. International Organization for Standardization.

Jeong, J. and Hussain, F. (1995). On the identification of a vortex. *Journal of Fluid Mechanics*, vol. 285, no. November 2018, pp. 69–94. ISSN 14697645.

Kearfott, B. (1979). An Efficient Degree-Computation Method for a Generalized Method of Bisection. *Numerische Mathematik*, vol. 32, no. 2, pp. 109–127.

Kohli, A. and Frenken, K. (2011 04). Cooling water for energy generation and its impact on national-level water statistics. *aquastat*.

Kopera, M.A. (2011). Direct numerical simulation of turbulent flow over a backward-facing step. In: *Journal of Fluid Mechanics*.

Kröger, D.G. (1998). *Air-cooled heat exchangers and cooling towers : thermal-flow performance evaluation and design*. Stellenbosch University.

Langtry, R.B. and Menter, F.R. (2009). Correlation-Based Transition Modeling for Unstructured Parallelized Computational Fluid Dynamics Codes. *AIAA Journal*, vol. 47, no. 12, pp. 2894–2906.

Launder, B.E. and Sharma, B.I. (1974). Application of the energy-dissipation model of turbulence to the calculation of flow near a spinning disc. *Letters in Heat and Mass Transfer*, vol. 1, no. 2, pp. 131–137. ISSN 0094-4548.
Available at: `http://www.sciencedirect.com/science/article/pii/0094454874901507`

Le Roux, F.N. (2010). *The CFD simulation of an axial flow fan*. Master's thesis, Stellenbosch University.

Stellenbosch University https://scholar.sun.ac.za

Lewis, R.I. (1996). *Turbomachinery performance analysis*. Butterworth-Heinemann.

Lien, F.S. and Leschziner, M.A. (1994). Assessment of turbulence-transport models including non-linear rng eddy-viscosity formulation and second-moment closure for flow over a backward-facing step. *Computers & Fluids*, vol. 23, no. 8, pp. 983–1004. ISSN 0045-7930.

Longhouse, R. (1977). Vortex shedding noise of low tip speed, axial flow fans. *Journal of Sound and Vibration*, vol. 53, no. 1, pp. 25 – 46. ISSN 0022-460X. Available at: `http://www.sciencedirect.com/science/article/pii/0022460X7790092X`

Louw, F.G. (2015). *Investigation of the flow field in the vicinity of an axial flow fan during low flow rates*. Ph.D. thesis, Stellenbosch University.

Louw, F.G., Bruneau, P.R.P., von Backström, T.W. and van der Spuy, S.J. (2012 06). The Design of an Axial Flow Fan for Application in Large Air-Cooled Heat Exchangers. In: *Turbo Expo: Power for Land, Sea, and Air*, vol. Volume 3, pp. 771–785.

Meissner, T.W. (2018). *Numerical Investigation of the Effect of Scaling on the Performance of Large Scale Axial Flow Fans*. Master's thesis, Stellenbosch University.

Menter, F. (1993). Zonal Two Equation k-w Turbulence Models For Aerodynamic Flows. *23rd Fluid Dynamics, Plasmadynamics, and Lasers Conference*, vol. 23.

OpenFOAM Guide (2019). OpenFOAM - The Open Source CFD Toolbox - User Guide v7. Available at: `http://foam.sourceforge.net/docs/Guides-a4/OpenFOAMUserGuide-A4.pdf`

OpenFoamWiki (2015). CheckMesh - OpenFOAMWiki. Available at: `https://openfoamwiki.net/index.php/CheckMesh`

Patankar, S.V. and Spalding, D.B. (1972). A calculation procedure for heat, mass and momentum transfer in three-dimensional parabolic flows. *International Journal of Heat and Mass Transfer*. ISSN 00179310.

Pearson, K. (1895). Note on regression and inheritance in the case of two parents. *Proceedings of the Royal Society of London*, , no. 58, pp. 240–242.

Sahili, A., Zogheib, B. and Barron, R.M. (2013). 3-D Modeling of Axial Fans. *Applied Mathematics*. ISSN 2152-7385.

Shih, T.-h., Zhu, J. and Lumley, J.L. (1993). A Realizable Reynolds Stress Algebraic Equation Model. *Nasa Technical Memorandum*, vol. 16596, pp. 1–34.

Spalart, P.R. and Allmaras, S.R. (1994). One-equation turbulence model for aerodynamic flows. *Recherche aerospatiale*. ISSN 00341223.

Stellenbosch University https://scholar.sun.ac.za

Thiart, G.D. and von Backström, T.W. (1993). Numerical simulation of the flow field near an axial flow fan operating under distorted inflow conditions. *Journal of Wind Engineering and Industrial Aerodynamics*, vol. 45, no. 2, pp. 189–214. ISSN 0167-6105.

Van Der Spuy, S.J. and Von Backström, T.W. (2015). An evaluation of simplified CFD models applied to perimeter fans in air-cooled steam condensers. In: *Proceedings of the Institution of Mechanical Engineers, Part A: Journal of Power and Energy*. ISSN 20412967.

Venter, S. (1990). *The effectiveness of Axial flow fans in A-frame Plenums*. Ph.D. thesis, Stellenbosch University.

Versteeg, H.K. and Malalasekera, W. (2007). *An introduction to computational fluid dynamics : the finite volume method*. 2nd edn. Pearson Education Ltd., Harlow, England. ISBN 9780131274983.

Wallis, R.A. (1983). *Axial Flow Fans and Ducts*. John Wiley and Sons. ISBN 978-0471870869.

Walters, D.K. and Cokljat, D. (2008). A three-equation eddy-viscosity model for reynolds-averaged navier-stokes simulations of transitional flow. *Journal of Fluids Engineering, Transactions of the ASME*. ISSN 00982202.

Wilkinson, M.B. (2017). *The Design of an Axial Flow Fan for Air-Cooled Heat Exchanger Applications*. Master's thesis, Stellenbosch University.

Wilkinson, M.B., Spuy, J.V.D. and Backstrom, T.W.V. (2019). Performance Testing of an Axial Flow Fan Designed for Air-Cooled Heat Exchanger Applications. In: *Turbomachinery Technical Conference and Exposition*.

Winkler, J., Moreau, S. and Carolus, T. (2012). Airfoil trailing-edge blowing: Broadband noise prediction from large-eddy simulation. *AIAA Journal*, vol. 50, no. 2, pp. 294–303. ISSN 0001-1452.

Wolf Dynamics (2017). Mesh generation using blockMesh.
Available at: `http://www.wolfdynamics.com/wiki/meshing_OF_blockmesh.pdf`

Yakhot, V., Orszag, S.A., Thangam, S., Gatski, T.B. and Speziale, C.G. (1992). Development of turbulence models for shear flows by a double expansion technique. *Physics of Fluids A: Fluid Dynamics*, vol. 4, no. 7, pp. 1510–1520.

Zuzul, J. (2017). *Numerical Evaluation of the Performance Curve for the NASA Rotor 67*. Master's thesis, University of Zagreb.

Stellenbosch University https://scholar.sun.ac.za

Appendix A

First Layer Height

An important consideration when modelling turbulence is appropriate wall treatment. This is due to the extremely thin boundary layers present in turbulent flow. In order to model these thin boundary layers accurately, the cells along walls must be very fine. The first layer height of wall bounded cells are non-dimensionlessed with the parameter y^+, defined as

$$y^+ = \frac{u_* \cdot y_1}{\nu} \tag{A.1}$$

where y_1 is the first cell height, ν the kinematic viscosity of the fluid, and u_* the friction velocity, described as

$$u_* = \sqrt{\frac{\tau_w}{\rho}} \tag{A.2}$$

where τ_w is the wall shear stress and ρ the fluid density.

For accurately solving the boundary layer, it is suggested that y^+ should not exceed 2.5 for the k-ω model. This leads to very fine cells being required next to the wall, which increases with an increase in shear stress associated with large velocity differences between the wall and freestream velocity. This is indeed the case for the B2a-fan, as the relative tangential velocity near the blade reaches 60 m/s.

An alternative method of calculating turbulent boundary layers is through use of wall functions. This calculates the flow variables outside of the viscous boundary layer and in the "logarithmic law" region instead. To successfully do this, a y^+ value of at least 30 is required in order to avoid the inertial sublayer, which would require the viscous sub layer to be solved as well. Furthermore, the y^+ value must be lower than 300, past which wall functions' accuracy rapidly diminishes, as this falls outside the entire boundary layer. As a result,

Stellenbosch University https://scholar.sun.ac.za

the smaller one can keep the y^+ value while keeping it out of the inertial sublayer, the better.

The difficulty in using wall functions is maintaining the range of $30 < y^+ < 300$. This is due to the large variation in shear force experienced over walls.

As part of the validation process while testing difference turbulence models, the y^+ value is monitored. The key areas of interest is the hub, blade and shroud, as these are the walls that affect the performance of the fan. These are presented in Table A.1

Table A.1: $y+$ of simulations during turbulence validation

Simulation	Wall	Minimum	Average	Maximum
k-ϵ high Re	Hub	17	70	190
	Blade	11	49	122
	Shroud	24	41	206
k-ω SST high Re	Hub	27	87	176
	Blade	0.35	36	134
	Shroud	23	40	218
k-ω SST low Re	Hub	18	55	100
	Blade	0.045	0.44	1.7
	Shroud	2.8	33	121

It is noted that OpenFOAM calculates a y^* instead of a y^+, which is defined as

$$y^* = \frac{\rho \cdot C_\mu^{0.25} \cdot y_1 \cdot \sqrt{k}}{\mu} \tag{A.3}$$

This closely matches the value of y^+, but makes use of turbulent kinetic energy, k, rather than wall shear.

It can be seen that for the high Reynolds cases, the y^+ on the blade is possibly too small. However, difficulty was experienced in obtaining a y^+ value that completely fulfilled the criteria, due to the large difference in wall speed experienced over the blade. The low Reynolds case mesh was deemed fine enough to fulfil the y^+ requirements on the blade, with the maximum y^+ never exceeding a value of 2.5.

Stellenbosch University https://scholar.sun.ac.za

Appendix B

Mesh Sensitivity Analysis

Mesh sensitivity is conducted as part of the validation study of Chapter 5. The inlet and outlet domain size sensitivity was not required since it has already been performed by Louw (2015) for the same fan in the same domain setup.

B.1 Methodology

In order to assess the sensitivity of the solution to the mesh density, three different meshes are generated for each geometry. These three meshes vary in cell size and the change in results between them will be assessed. It was found that the square hub required an overall coarser mesh in order to achieve stable convergence. The disk hub, on the other hand, required a finer mesh in order to not diverge. It is suspected that this is due to ensuring adequate data transfer between AMI patch zones.

Two metrics are measured in order to evaluate results; total-to-static pressure rise ($\Delta P_{f,s}$) and efficiency (η). For each metric, a curve is fitted using an exponential function as shown in equation B.1

$$U = C \cdot e^{h \cdot a}, \tag{B.1}$$

where U is a metric to be assessed, h is a measure of cell size, and C and a constants to be used for fitting the curve. This allows an estimate of an 'exact solution' given a cell size of 0. Based on this, each mesh density can be compared to this 'exact solution' and an error estimate can be established.

Stellenbosch University https://scholar.sun.ac.za

B.2 Results

Table B.1: Round hub mesh sensitivity

Number of cells	$\Delta p_{f,s}$	Error	η	Error
2.6×10^6	196.82 Pa	4.72 %	66.14 %	2.19 %
*5.5×10^6	188.65 Pa	0.37 %	65.26 %	0.83 %
11.9×10^6	191.69 Pa	1.98 %	65.09 %	0.57 %
Est. exact	187.96 Pa		64.72 %	

Table B.2: Square hub mesh sensitivity

Number of cells	$\Delta p_{f,s}$	Error	η	Error
2.4×10^6	192.83 Pa	2.69 %	66.08 %	2.46 %
4.0×10^6	192.09 Pa	2.30 %	65.58 %	1.68 %
*6.1×10^6	189.26 Pa	0.79 %	65.08 %	0.91 %
Est. exact	187.77 Pa		64.50 %	

Table B.3: Centre disk mesh sensitivity

Number of cells	$\Delta p_{f,s}$	Error	η	Error
*6.7×10^6	178.33 Pa	0.81 %	60.16 %	1.03 %
9.3×10^6	180.19 Pa	1.87 %	60.53 %	1.65 %
13.0×10^6	176.98 Pa	0.05 %	59.71 %	0.27 %
Est. exact	176.89 Pa		59.55 %	

All three configurations made use of at least one mesh with the same cell settings, as represented by an *. This is also the mesh settings that were used for the remaining simulations throughout this thesis. It was found to provide adequate accuracy whilst minimising computational time requirements, and the meshes were consistent between hub configurations. Tables B.1 to B.3 show that the error on these meshes are minimal, especially when compared to alternative meshes. This suggests that the results are not heavily dependent on mesh density.

It is noted that for the same mesh settings, the different hub configurations will require different number of cells due to the mesh around the hub.

For context, the mesh density used in the thesis is shown in Figures B.1 for the round hub.

Stellenbosch University https://scholar.sun.ac.za

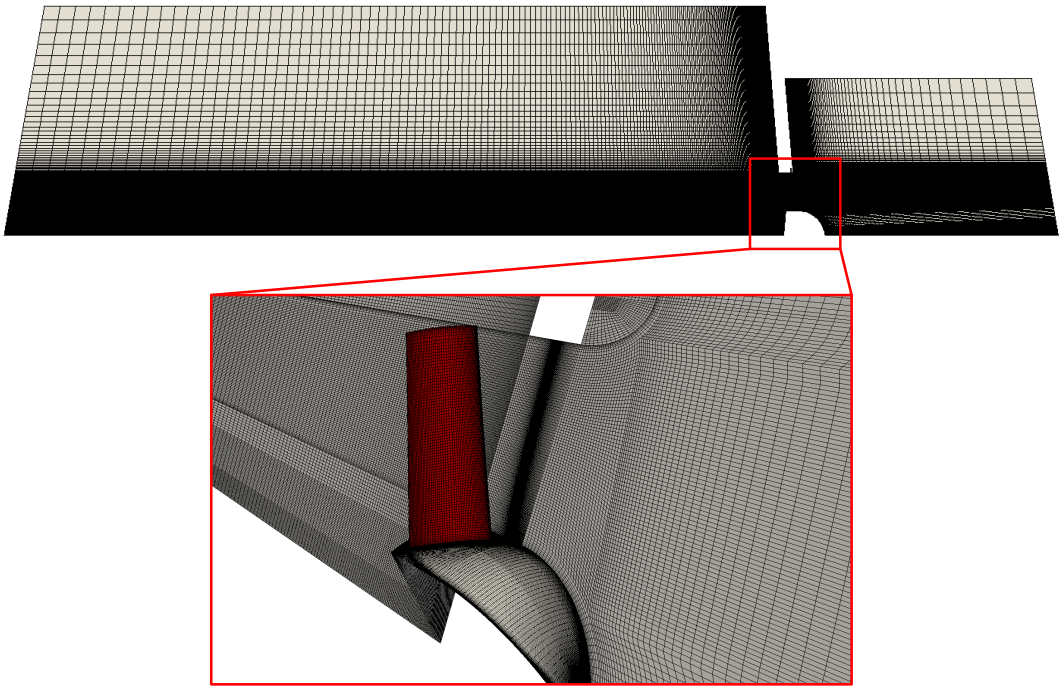

Figure B.1: Medium density mesh for round hub

B.3 Mesh Quality

Mesh quality metrics are defined in Section 3.3.1. These mesh quality metrics are assessed for the meshes used for each geometry, and are summarised in Table B.4. This shows that the attained mesh quality of the round and square hub exceeds the requirements set by OpenFOAM, where a non-orthogonality of $< 70^o$ and skewness of < 4 is specified.

Table B.4: Attained mesh quality

Geometry	Non-orthogonality, maximum (average)	Skewness, maximum
Round hub	58.5^o (13.2^o)	0.9196
Square hub	60.2^o (12.5^o)	0.9196
Centre disk hub	77.4^o (13.1^o)	4.6018

The significantly higher maximum skewness and non-orthoganality of the centre disk hub configuration is due to seven poor quality cells in the internal region of the blade. As the flow here is insignificant, the quality of these cells are deemed unimportant. If this region is not considered, the cell quality metrics align with that of the round hub and square configurations.

Stellenbosch University https://scholar.sun.ac.za

Appendix C

Pearson Correlation and Root Mean Square Difference

The Pearson correlation factor, R_p and root-mean-square difference (RMSD) can be used as measures to determine the difference in two data sets. As such, it is used within this thesis to compare between numerically obtained data, and experimental data obtained by Louw (2015), for blade surface pressure (BSP) comparisons.

C.1 Discretization

Both the RMSD and Pearson correlation requires the comparison of discrete data points. As such, an algorithm is developed that identifies the numerically obtained coefficient of pressure that correlates with the same blade position that the experimental coefficient of pressure was determined at. This is demonstrated in Figure C.1 for the BSP at a height of $S_b = 0.1$ and $\dot{V} = 16$ m$^3/s$.

Stellenbosch University https://scholar.sun.ac.za

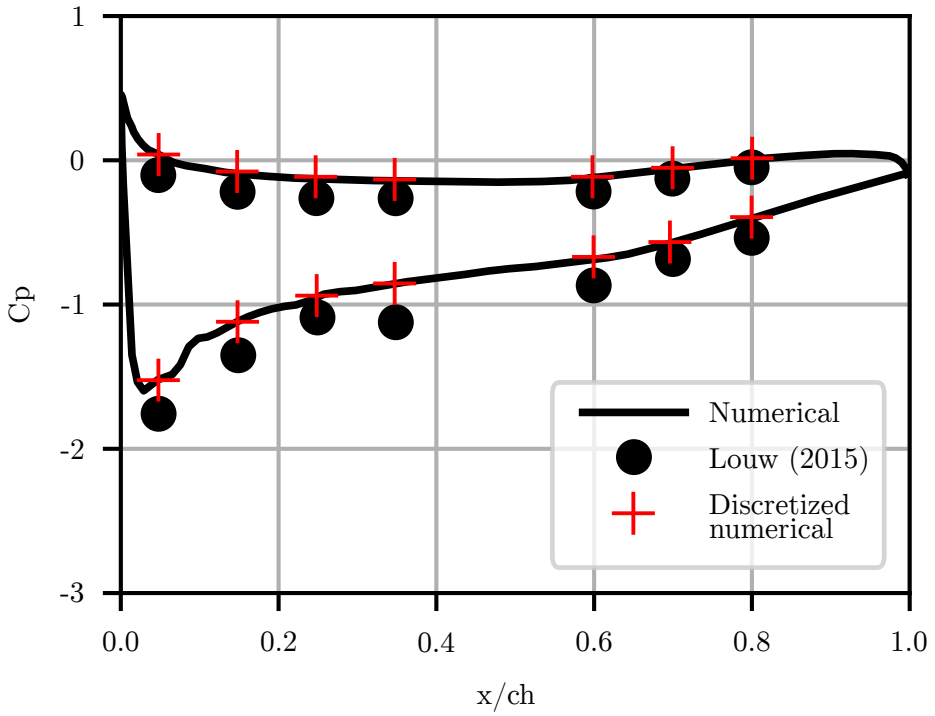

Figure C.1: Discretization of numerical data points

C.2 Root Mean Square Difference

The RMSD is defined as

$$RMSD = \sqrt{\frac{\sum_{n=0}^{N}(Cp_{num,n} - Cp_{exp,n})^2}{N}} \tag{C.1}$$

where N is the total number of discretized points, and Cp_{num} and Cp_{exp} is the numerically and experimentally obtained coefficient of pressures respectively.

The RMSD therefore represents the average difference in the numerical and experimental results.

C.3 Pearson Correlation

The Pearson correlation coefficent is defined as

$$R_p = \frac{\mathrm{cov}(Cp_{num}, Cp_{exp})}{\sigma_{num}\ \sigma_{exp}} \tag{C.2}$$

Stellenbosch University https://scholar.sun.ac.za

where cov is the covariance, and σ_{num} and σ_{exp} the standard deviation of the numerical and experimental data respectively.

R_p represents the scatter of data around a line of best fit. A larger scatter of data represents a poorer correlation between two data sets. In this case the two data sets is that of the numerically and experimentally obtained pressure coefficients. This can be represented on a XY plot as shown in Figure C.2. A

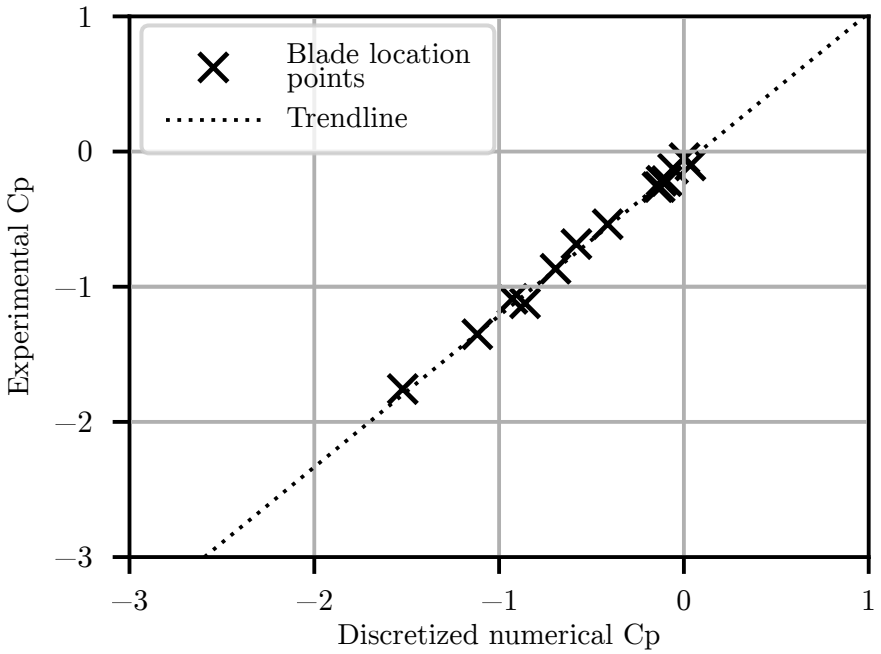

Figure C.2: XY plot of BSP to represent R_p calculation

Pearson correlation coefficient of 1 represents a perfect linear trend between two data sets, while a coefficient of -1 represents a perfect negative correlation. In the case of comparison to experimental data, a Pearson correlation coefficient that tends to unity represents the best correlation.

Stellenbosch University https://scholar.sun.ac.za

Appendix D

Blade Surface Pressure

D.1 BSP Validation At Off-Design Points

During validation, a comparison of blade surface pressure (BSP) between numerical and experimental data was done. Only the $\dot{V} = 16$ m$^3/s$ BSP data was presented in the main body of this thesis, while Figures D.1 to D.4 contains the BSP comparison of all tested volumetric flow rates. It can be seen that the largest error generally occurs near the blade tip, and the error grows with volumetric flow rate. At above design point ($\dot{V} = 19$ m$^3/s$), the largest error is present near the hub. This implies that the deviation between numerical and experimental at above design point flow rate is due to a different reason than for the other flow rates.

Stellenbosch University https://scholar.sun.ac.za

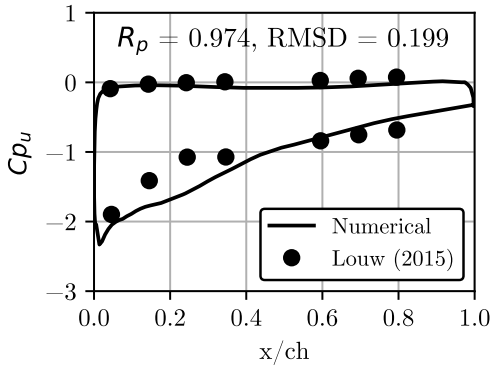

(a) $S_b = 0.1$

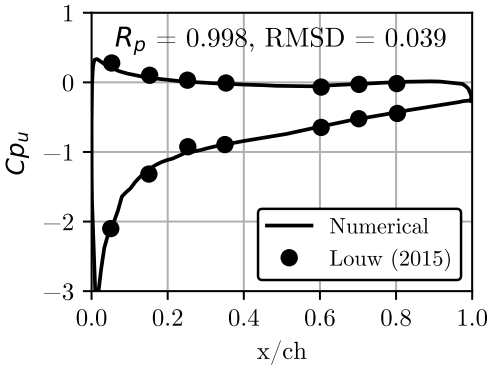

(b) $S_b = 0.3$

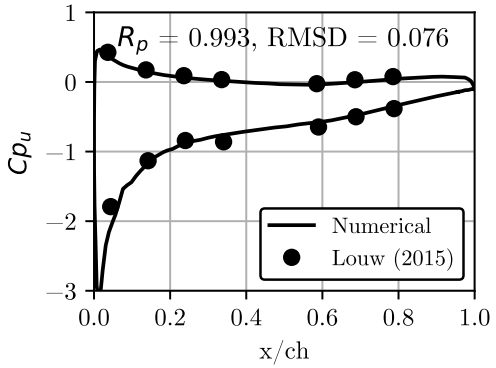

(c) $S_b = 0.5$

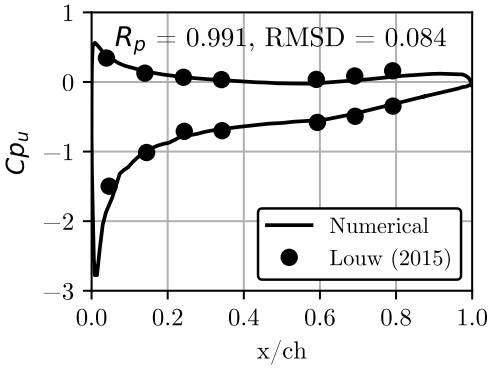

(d) $S_b = 0.7$

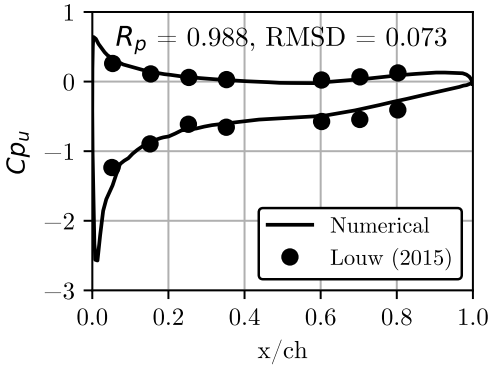

(e) $S_b = 0.9$

Figure D.1: Blade surface pressure at $\dot{V} = 10$ m^3/s at $sb =$ a) 10 %, b) 30 %, c) 50 %, d) 70 %, e) 90 %

Stellenbosch University https://scholar.sun.ac.za

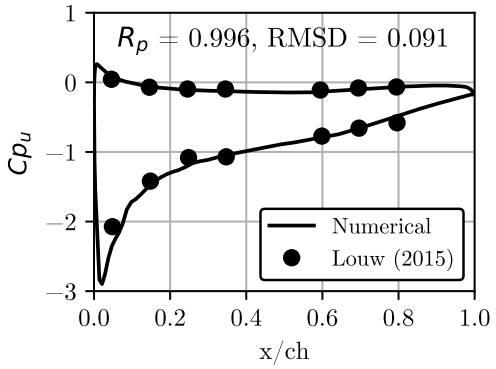

(a) $S_b = 0.1$

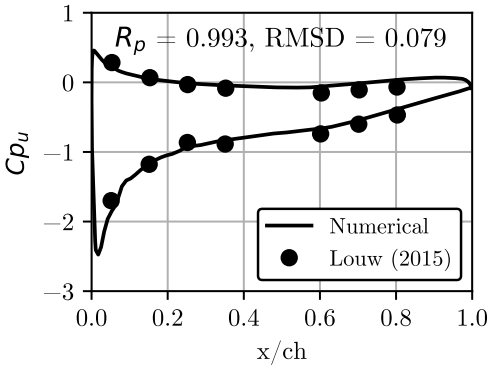

(b) $S_b = 0.3$

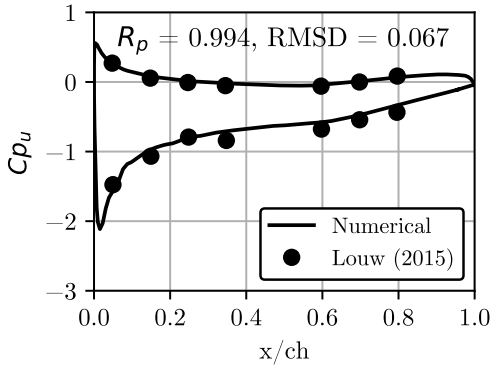

(c) $S_b = 0.5$

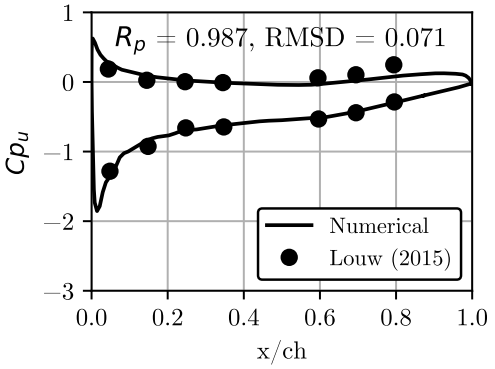

(d) $S_b = 0.7$

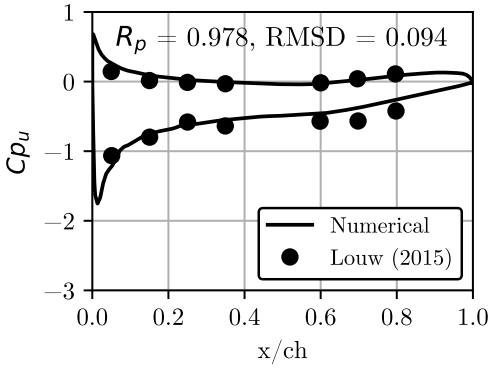

(e) $S_b = 0.9$

Figure D.2: Blade surface pressure at $\dot{V} = 13$ m^3/s at $sb =$ a) 10 %, b) 30 %, c) 50 %, d) 70 %, e) 90 %

Stellenbosch University https://scholar.sun.ac.za

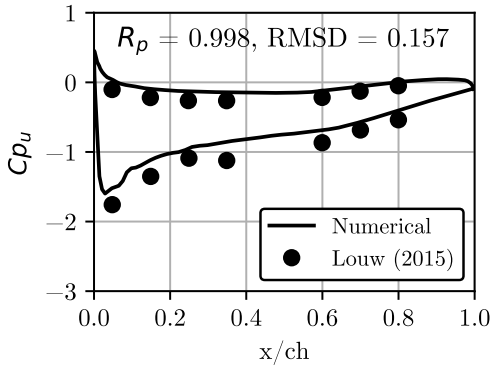

(a) 10 % blade span

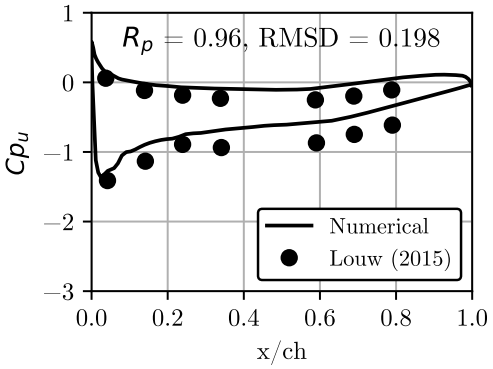

(b) 30 % blade span

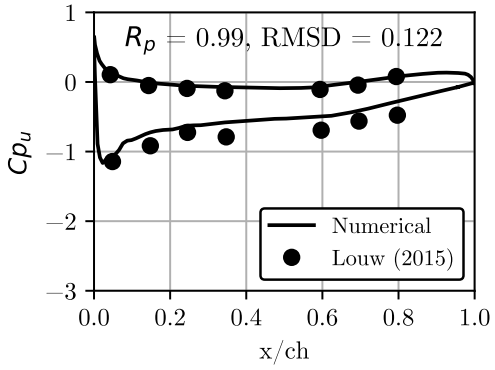

(c) 50 % blade span

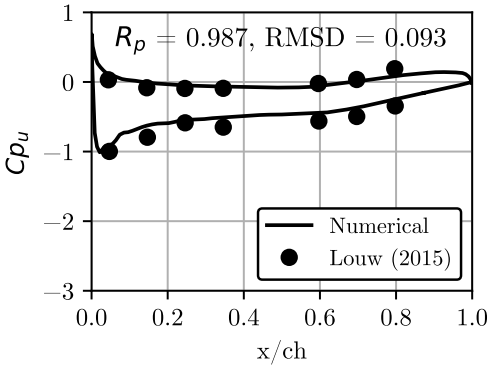

(d) 70 % blade span

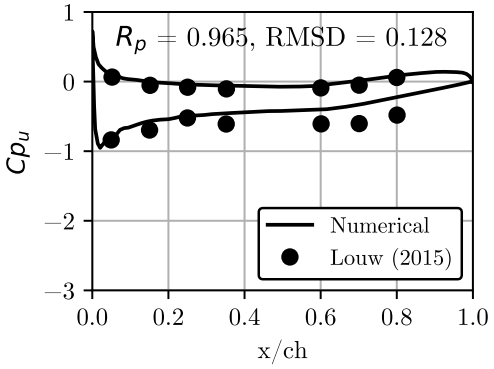

(e) 90 % blade span

Figure D.3: Blade surface pressure at $\dot{V} = 16$ m^3/s at $sb =$ a) 10 %, b) 30 %, c) 50 %, d) 70 %, e) 90 %

Stellenbosch University https://scholar.sun.ac.za

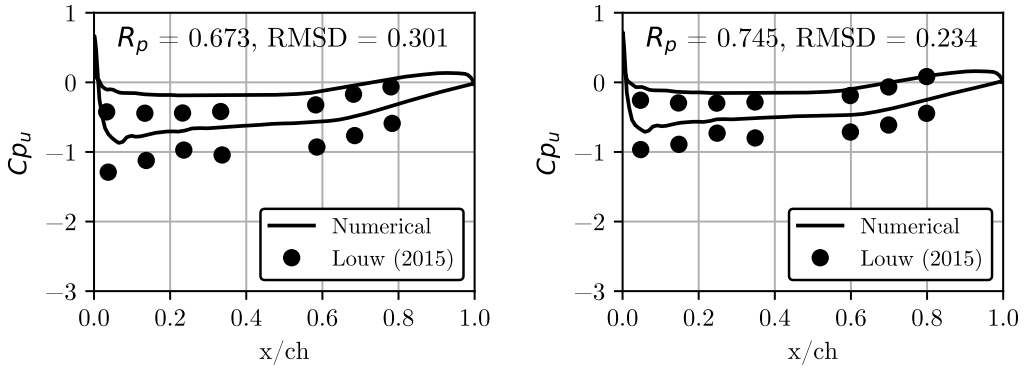

(a) $S_b = 0.1$

(b) $S_b = 0.3$

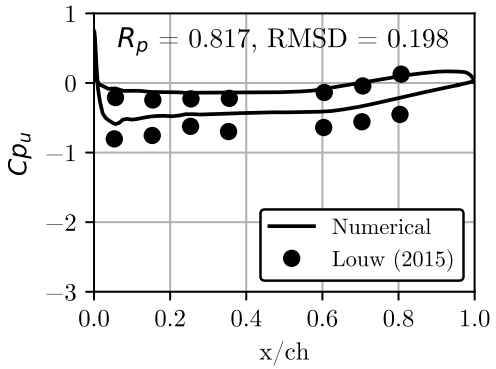

(c) $S_b = 0.5$

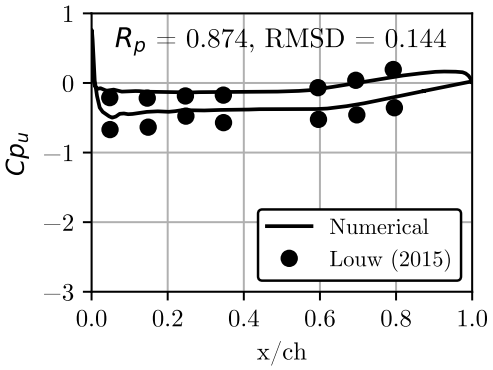

(d) $S_b = 0.7$

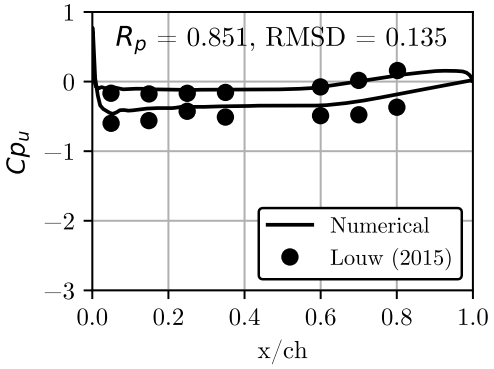

(e) $S_b = 0.9$

Figure D.4: Blade surface pressure at $\dot{V} = 19$ m^3/s at $sb =$ a) 10 %, b) 30 %, c) 50 %, d) 70 %, e) 90 %

Stellenbosch University https://scholar.sun.ac.za

D.2 BSP Comparison

In the review of the BSP of various hubs, only the 10% and 30% span measures were considered in the main body of this thesis. This is due to the relatively minor effect of hub configuration on the BSP at further radial spans. All 5 radial locations for the 4 different volumetric flow rates are shown in Figures D.5 to D.8.

Results obtained from XFoil also illustrate the deviation between predicted two-dimensional blade response and the attained three-dimensional response for the round hub. It can clearly be seen that near the hub, XFoil largely underpredicts the suction side pressure distribution. As span increases, a closer correlation between XFoil and the three-dimensional blade is observed.

Stellenbosch University https://scholar.sun.ac.za

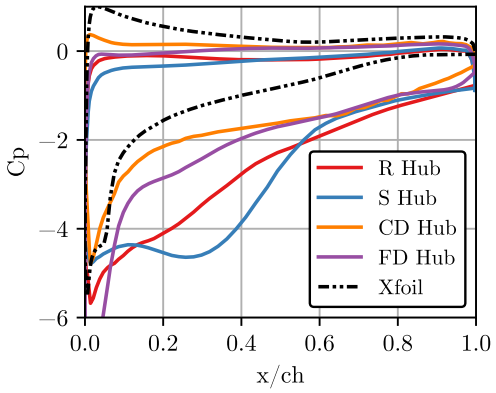

(a) $S_b = 0.1$

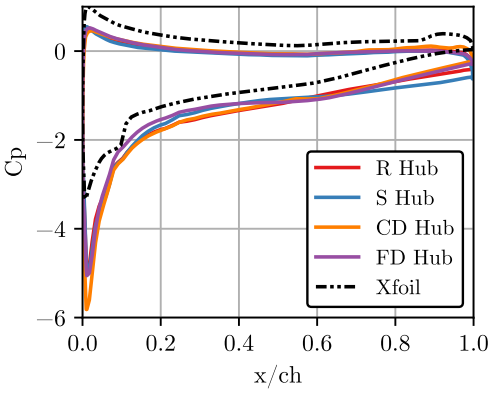

(b) $S_b = 0.3$

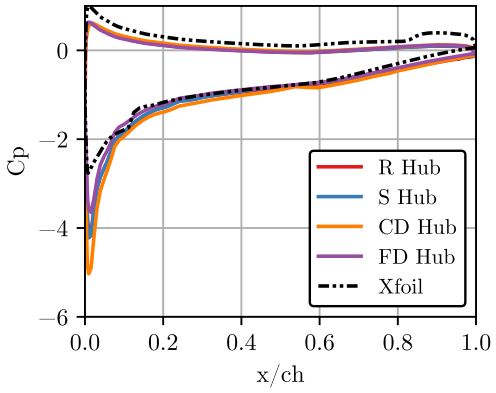

(c) $S_b = 0.5$

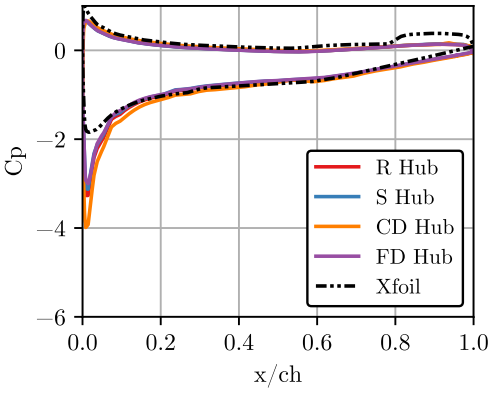

(d) $S_b = 0.7$

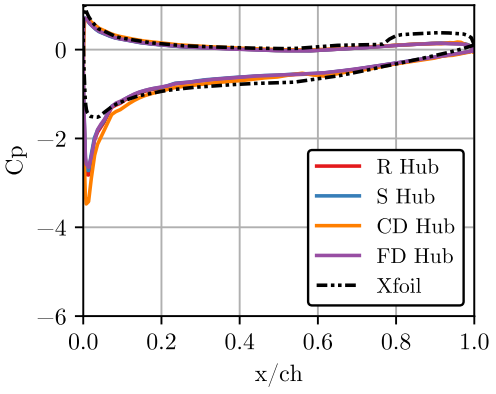

(e) $S_b = 0.9$

Figure D.5: Blade surface pressure at $\dot{V} = 10$ m^3/s at sb = a) 10 %, b) 30 %, c) 50 %, d) 70 %, e) 90 %

Stellenbosch University https://scholar.sun.ac.za

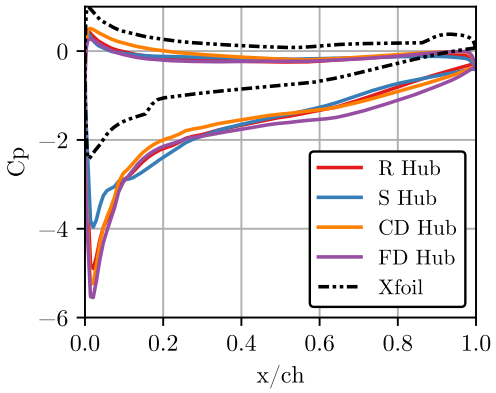

(a) $S_b = 0.1$

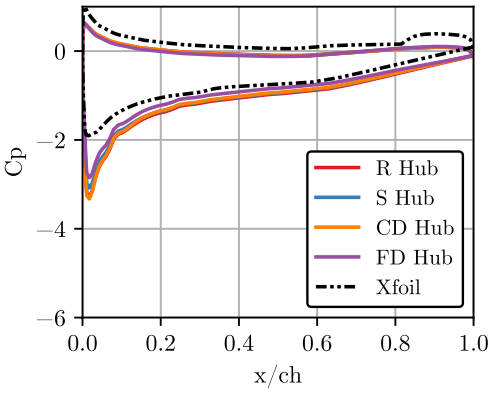

(b) $S_b = 0.3$

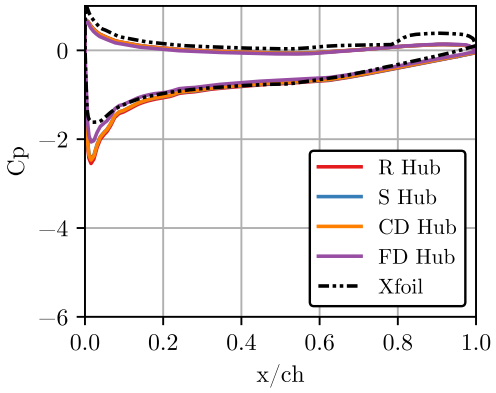

(c) $S_b = 0.5$

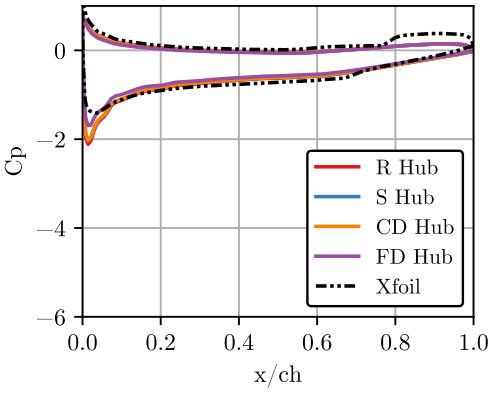

(d) $S_b = 0.7$

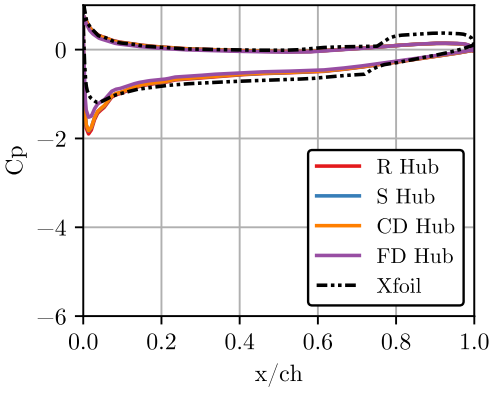

(e) $S_b = 0.9$

Figure D.6: Blade surface pressure at $\dot{V} = 13$ m^3/s at $sb =$ a) 10 %, b) 30 %, c) 50 %, d) 70 %, e) 90 %

Stellenbosch University https://scholar.sun.ac.za

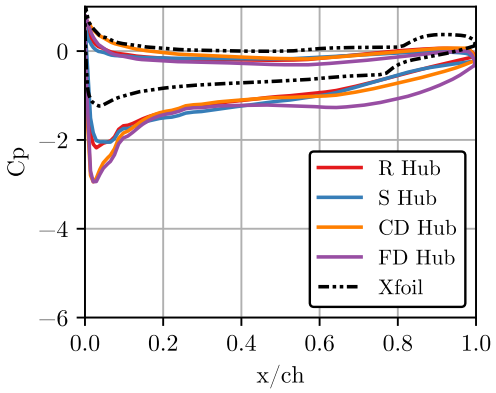

(a) $S_b = 0.1$

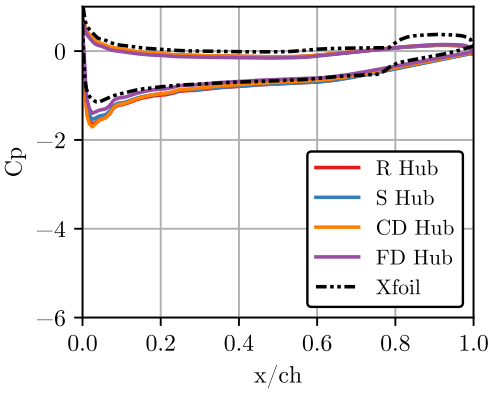

(b) $S_b = 0.3$

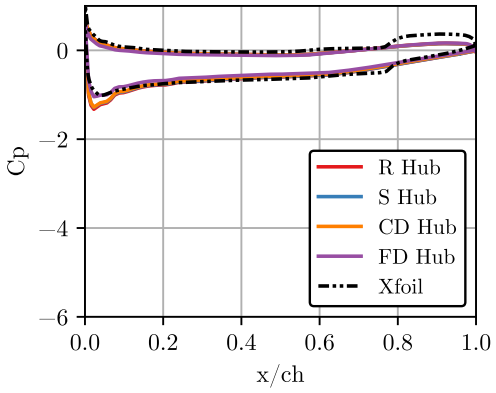

(c) $S_b = 0.5$

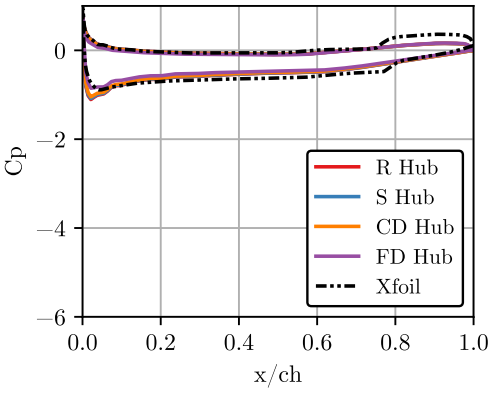

(d) $S_b = 0.7$

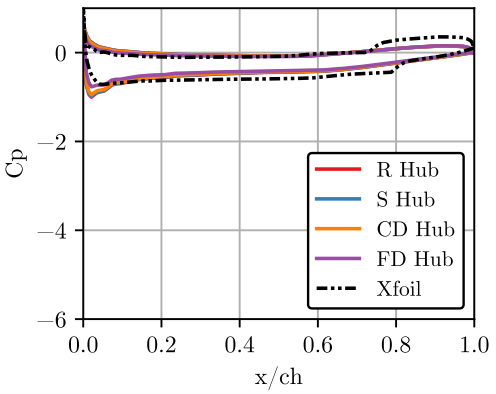

(e) $S_b = 0.9$

Figure D.7: Blade surface pressure at $\dot{V} = 16$ m^3/s at sb = a) 10 %, b) 30 %, c) 50 %, d) 70 %, e) 90 %

Stellenbosch University https://scholar.sun.ac.za

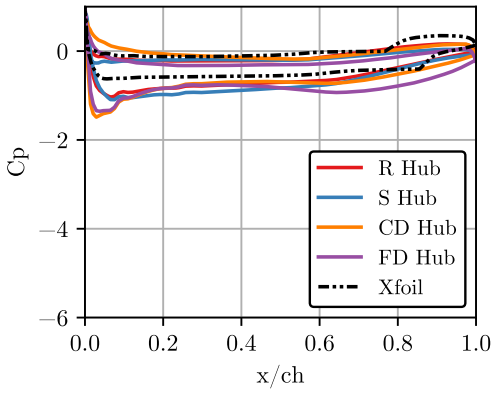

(a) $S_b = 0.1$

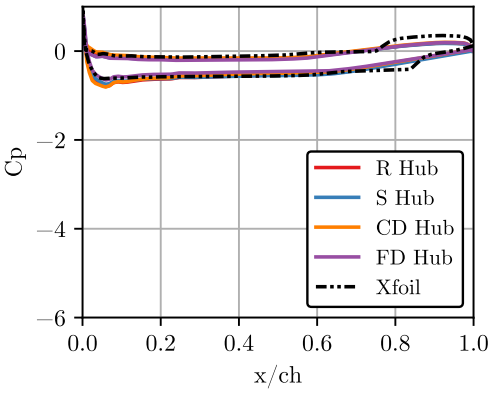

(b) $S_b = 0.3$

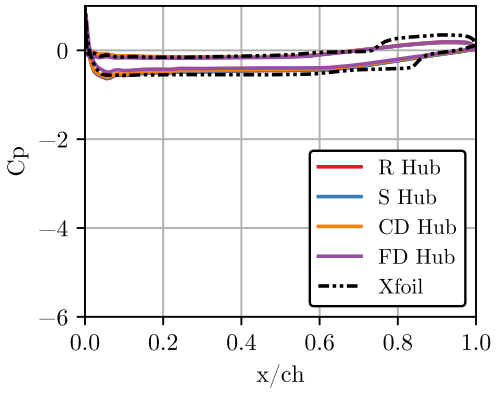

(c) $S_b = 0.5$

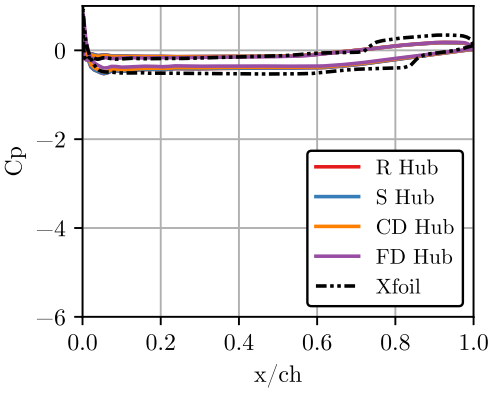

(d) $S_b = 0.7$

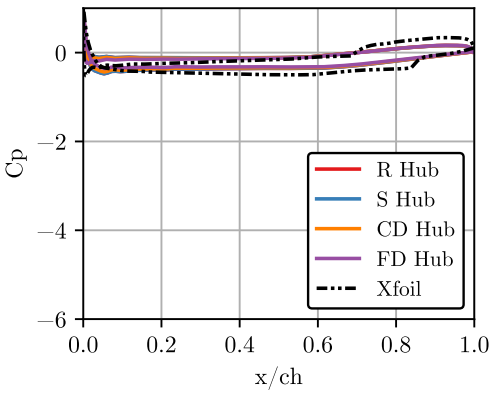

(e) $S_b = 0.9$

Figure D.8: Blade surface pressure at $\dot{V} = 19$ m^3/s at sb = a) 10 %, b) 30 %, c) 50 %, d) 70 %, e) 90 %

Stellenbosch University https://scholar.sun.ac.za

Appendix E

Fan Performance of Various Hub Configurations

Section 6.2 discuss the variation in total-to-static pressure rise, shaft power consumption, and efficiency relative to that of the round hub. This was motivated due to the relatively minor differences in fan performance of different hub configurations. For completeness, Figures E.1 to E.3 show the complete curve of all the tested hub geometries. This more clearly shows the extension of stall margin for the flat plate geometries, as a more linear response is achieved between total-to-static pressure rise and volumetric flow rate.

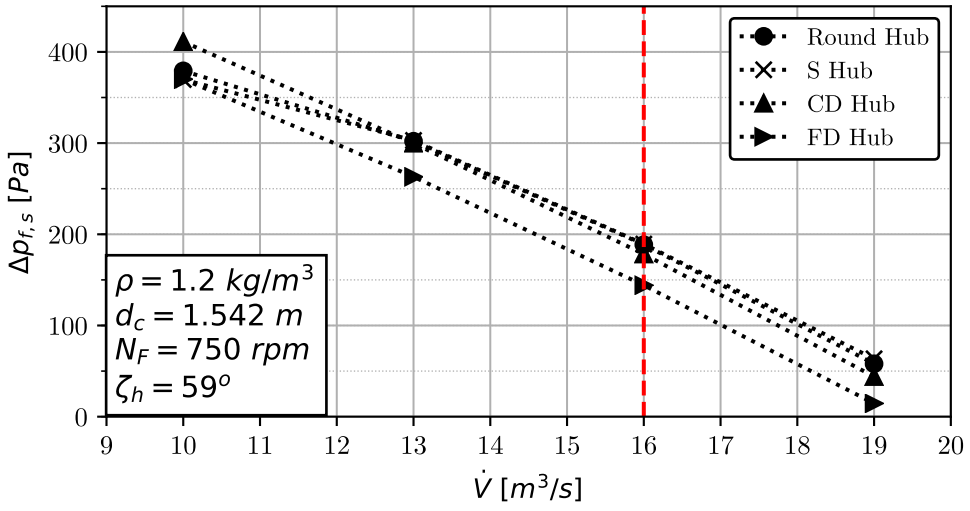

Figure E.1: Total-to-static pressure rise operating curve for all tested hub geometries

Stellenbosch University https://scholar.sun.ac.za

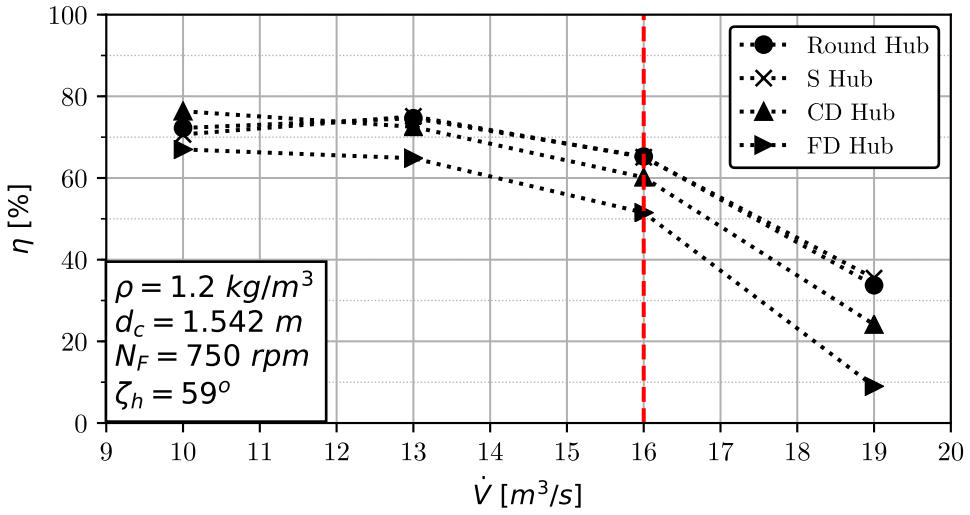

Figure E.2: Efficiency curve for all tested hub geometries

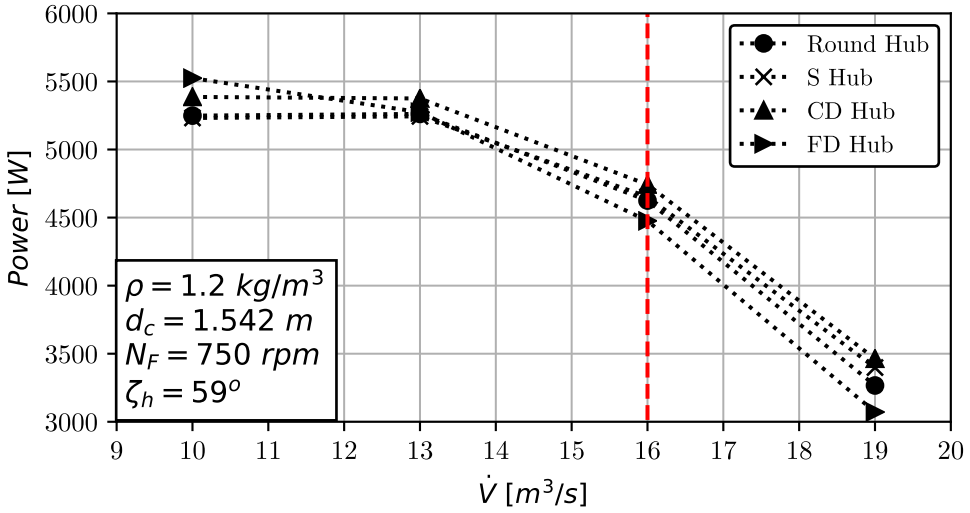

Figure E.3: Fan shaft power consumption curve for all tested hub geometries

Table E.1 presents the numerical values that is illustrated in Figures E.1 to E.3.

Stellenbosch University https://scholar.sun.ac.za

Table E.1: Fan performance values

Hub configuration	Flow rate [m^3/s]	$\Delta p_{f,s}$ [Pa]	P [W]	η [%]
Round hub	10	379	5249	72.2
	13	302	5262	74.6
	16	189	4625	65.3
	19	58.0	3267	33.7
Square hub	10	370	5232	70.7
	13	303	5244	75.1
	16	189	4653	65.1
	19	63.5	3398	35.5
Centre disk hub	10	411	5386	76.3
	13	300	5375	72.5
	16	178	4742	60.2
	19	44.0	3463	24.1
Forward disk hub	10	370	5524	67.0
	13	263	5269	64.8
	16	144	4476	51.5
	19	14.5	3072	9.0

Stellenbosch University https://scholar.sun.ac.za

Appendix F

Meridional Streamlines

Figures F.1 to F.16 illustrate the meridional streamlines near the rotor region for all hub configurations at all evaluated volumetric flow rates. This more clearly shows the large recirculatory vortex that leaks into the round and square hubs at $\dot{V} = 10\ \mathrm{m}^3/s$.

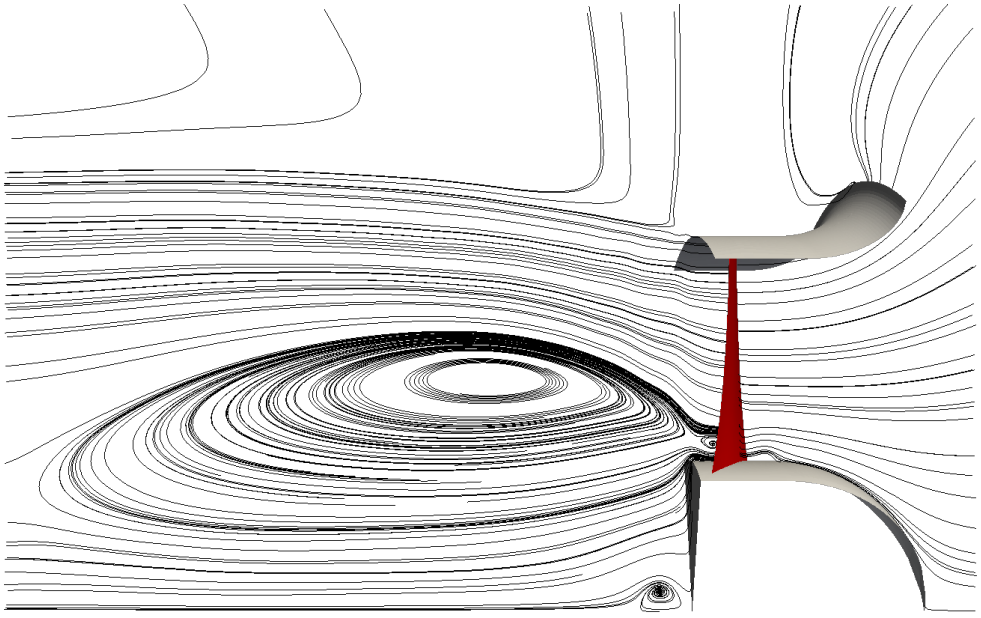

Figure F.1: Meridional streamlines of the round hub at $\dot{V} = 10\ \mathrm{m}^3/s$

Stellenbosch University https://scholar.sun.ac.za

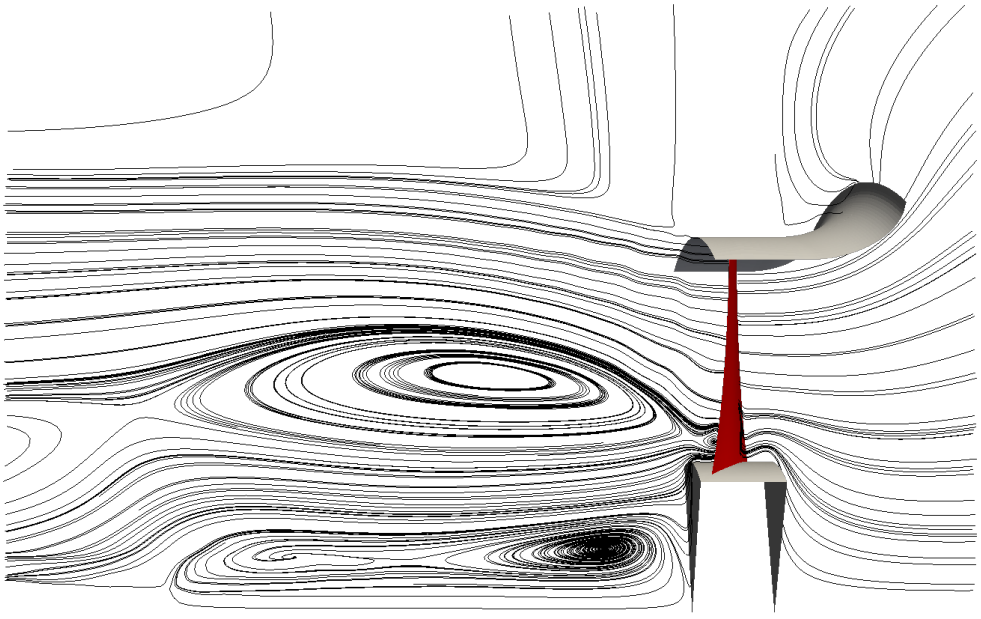

Figure F.2: Meridional streamlines of the square hub at $\dot{V} = 10\ \mathrm{m}^3/s$

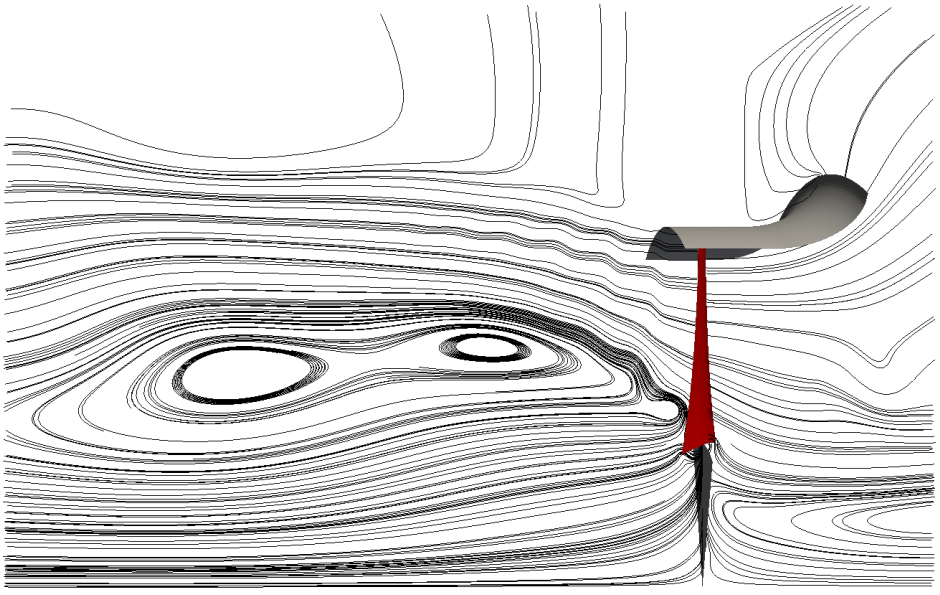

Figure F.3: Meridional streamlines of the centre disk hub at $\dot{V} = 10\ \mathrm{m}^3/s$

Stellenbosch University https://scholar.sun.ac.za

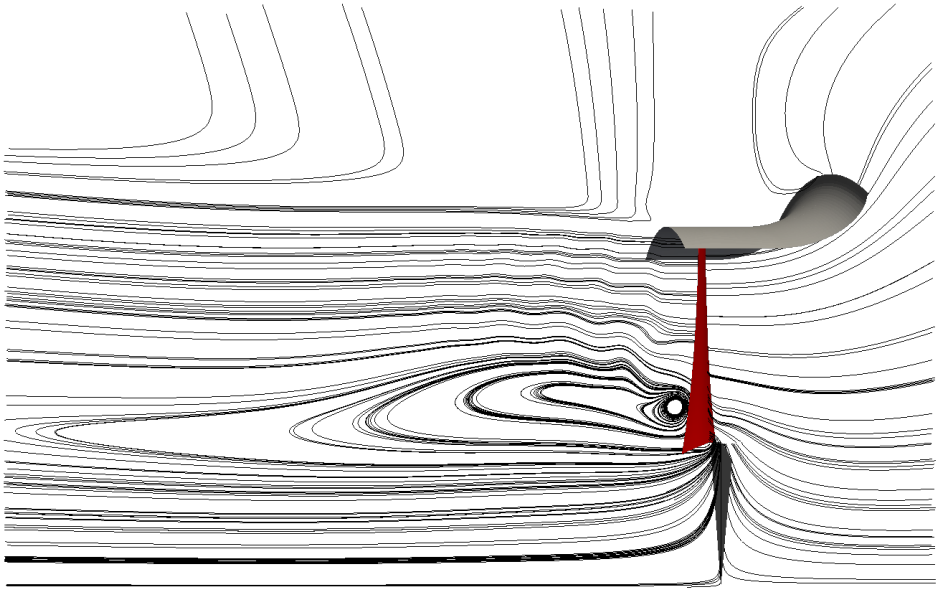

Figure F.4: Meridional streamlines of the forward disk hub at $\dot{V} = 10\ \mathrm{m}^3/s$

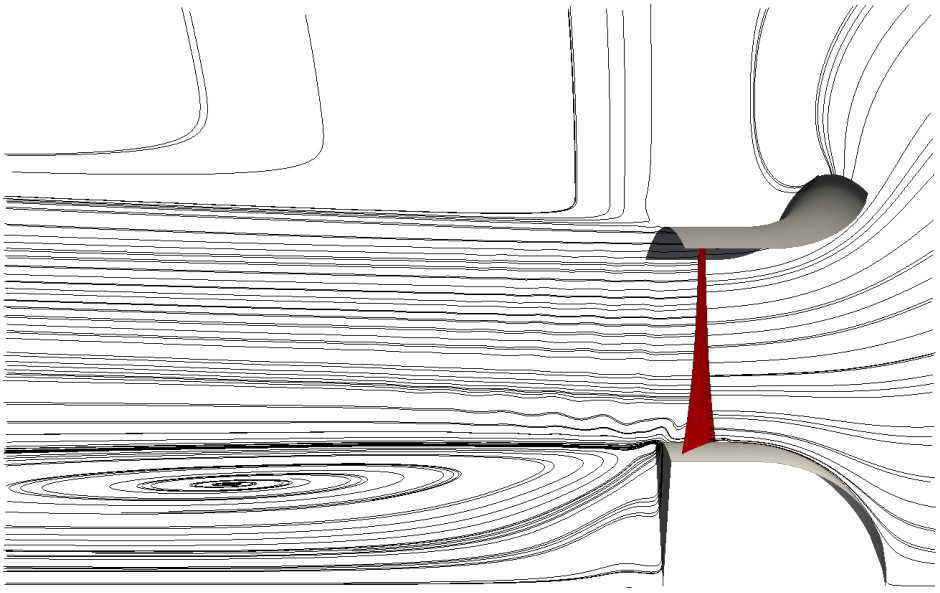

Figure F.5: Meridional streamlines of the round hub at $\dot{V} = 13\ \mathrm{m}^3/s$

Stellenbosch University https://scholar.sun.ac.za

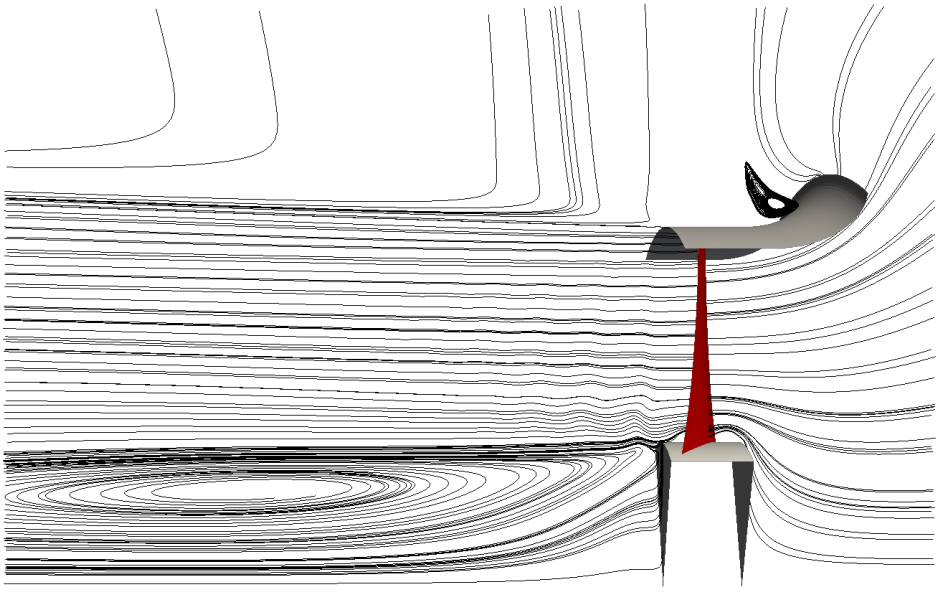

Figure F.6: Meridional streamlines of the square hub at $\dot{V} = 13\ \mathrm{m}^3/s$

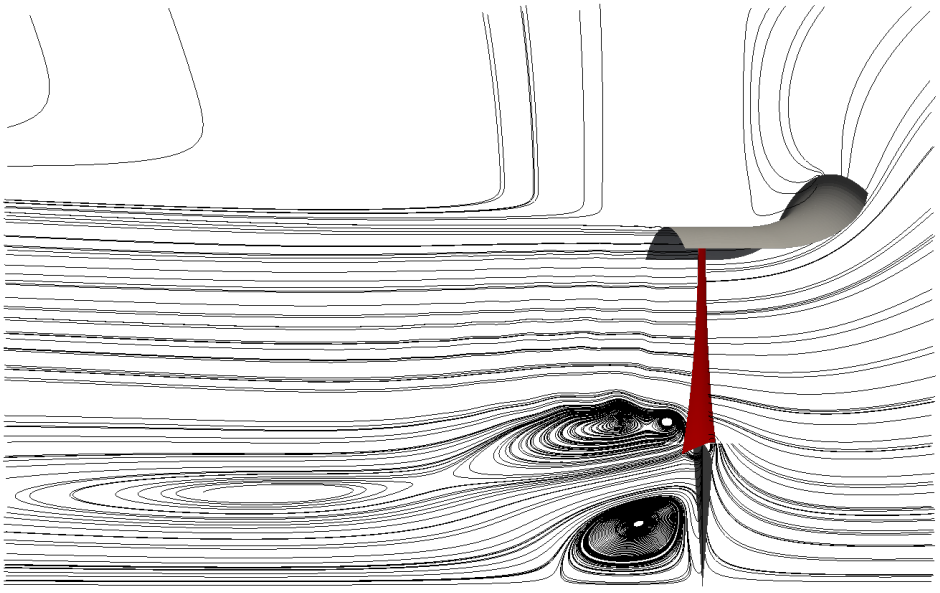

Figure F.7: Meridional streamlines of the centre disk hub at $\dot{V} = 13\ \mathrm{m}^3/s$

Stellenbosch University https://scholar.sun.ac.za

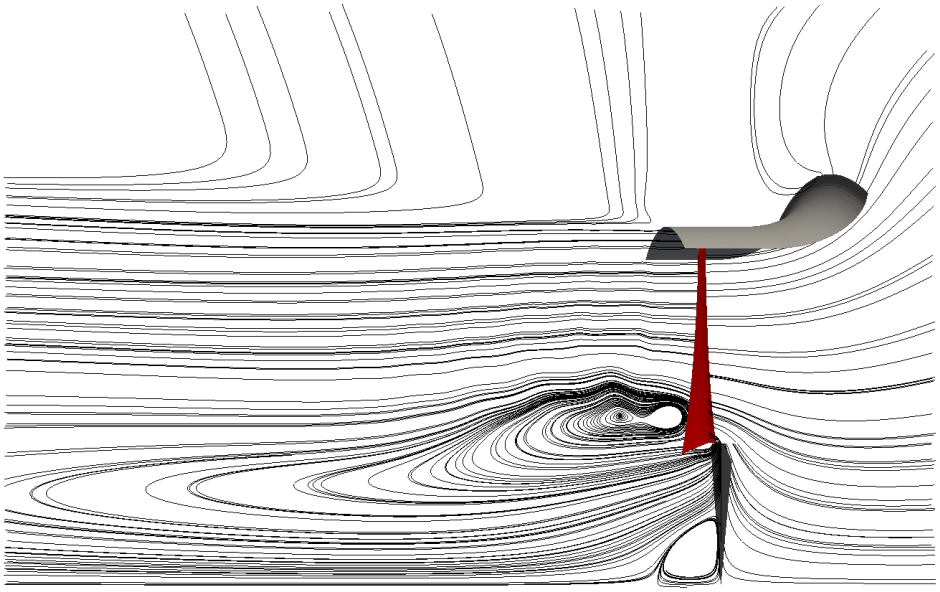

Figure F.8: Meridional streamlines of the forward disk hub at $\dot{V} = 13\ \mathrm{m}^3/s$

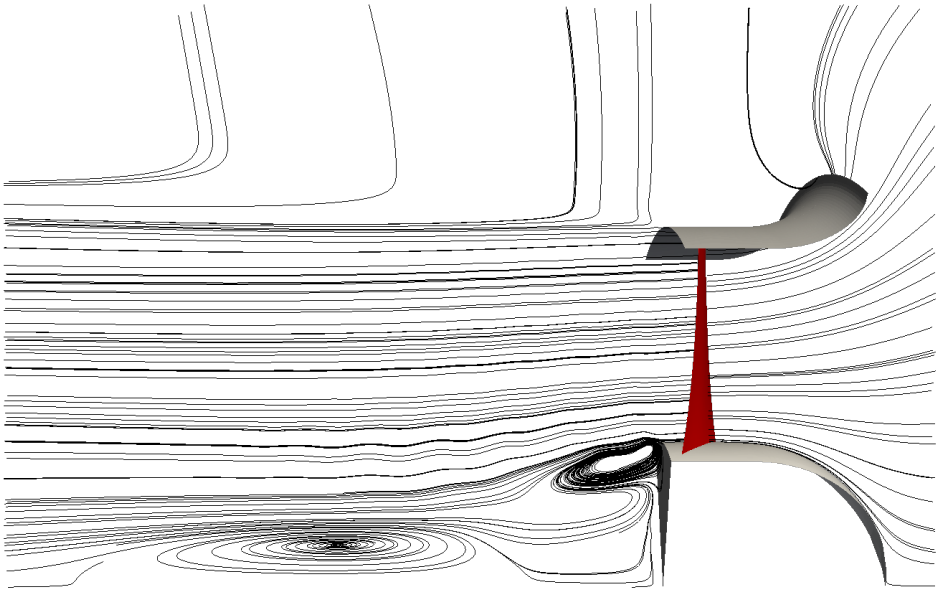

Figure F.9: Meridional streamlines of the round hub at $\dot{V} = 16\ \mathrm{m}^3/s$

Stellenbosch University https://scholar.sun.ac.za

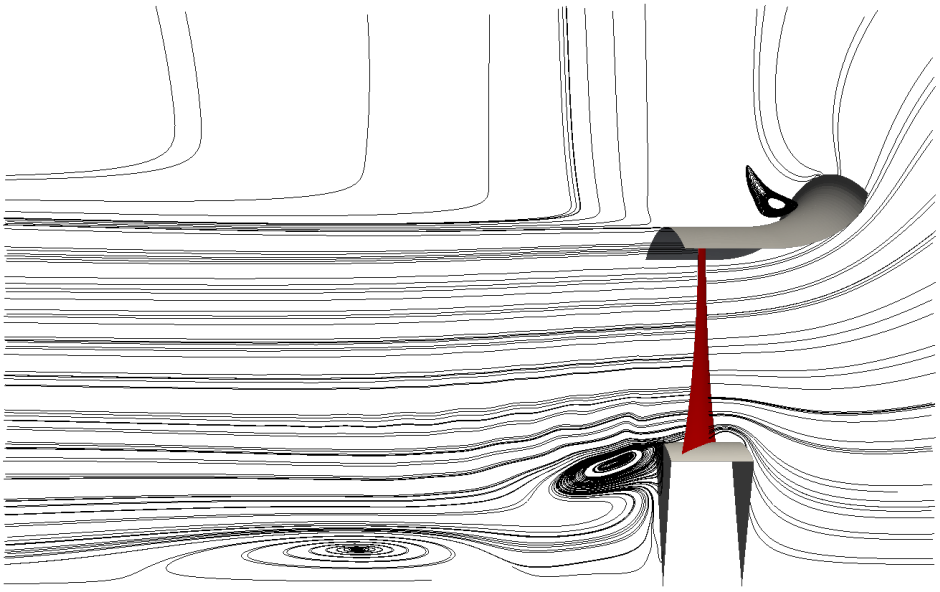

Figure F.10: Meridional streamlines of the square hub at $\dot{V} = 16\ \mathrm{m}^3/s$

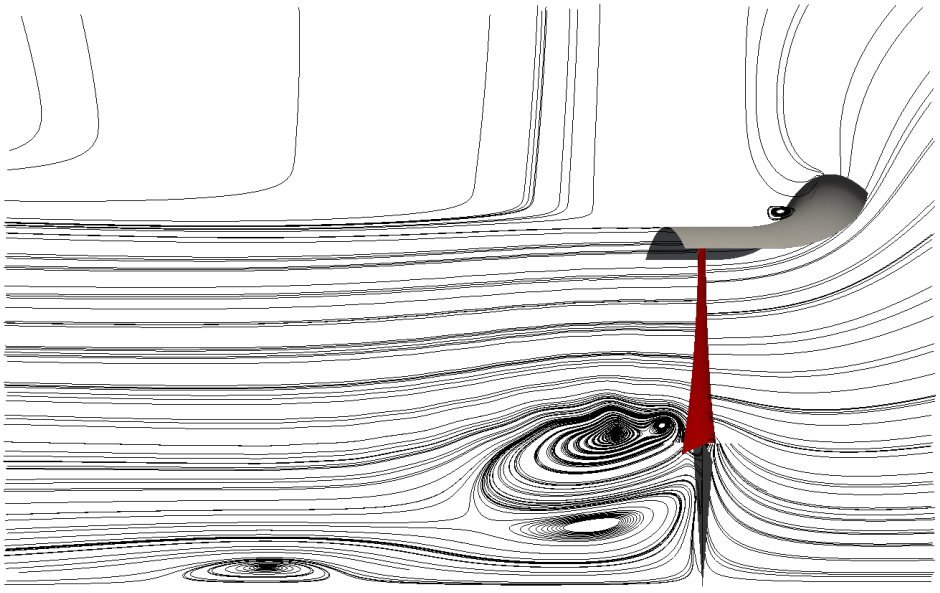

Figure F.11: Meridional streamlines of the centre disk hub at $\dot{V} = 16\ \mathrm{m}^3/s$

Stellenbosch University https://scholar.sun.ac.za

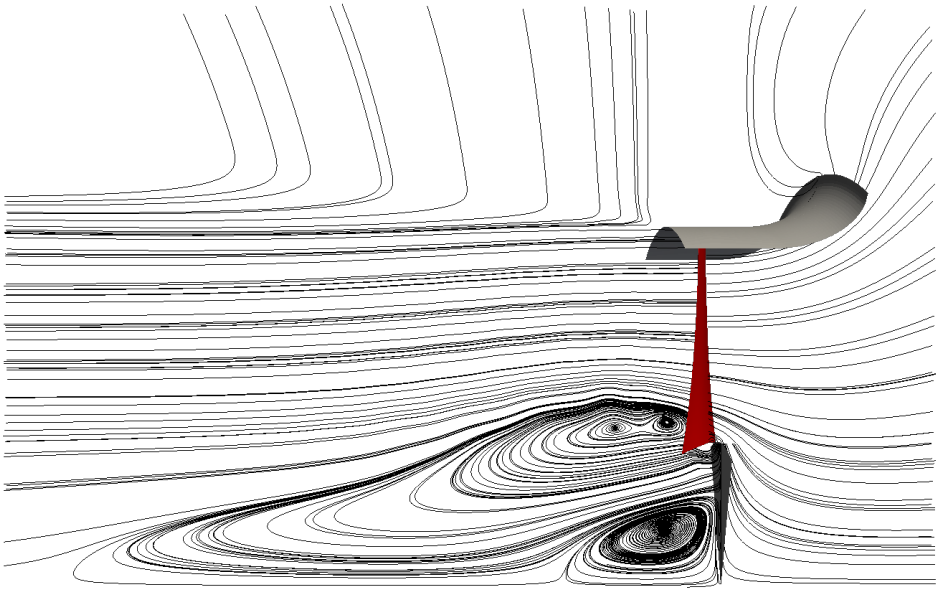

Figure F.12: Meridional streamlines of the forward disk hub at $\dot{V} = 16$ m$^3/s$

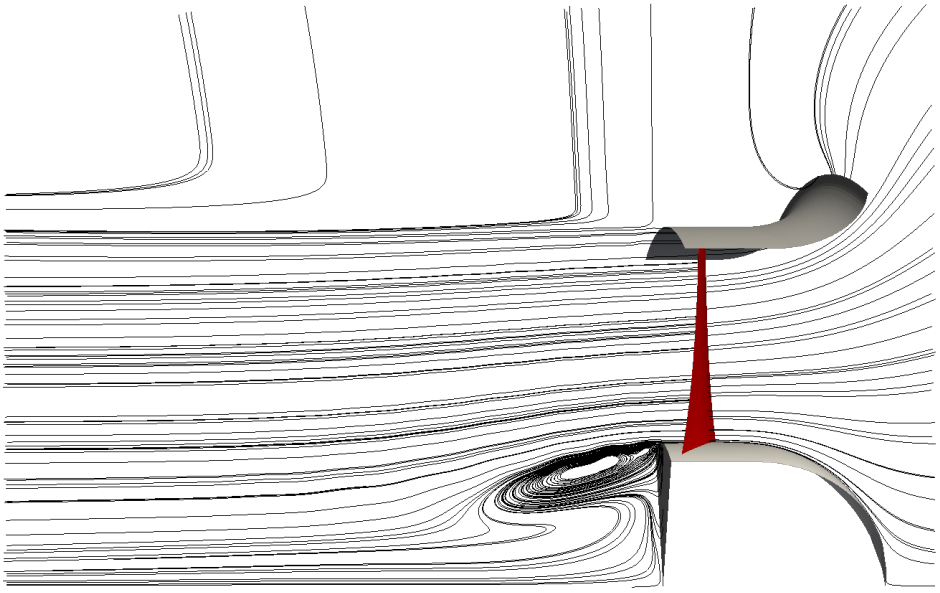

Figure F.13: Meridional streamlines of the round hub at $\dot{V} = 19$ m$^3/s$

Stellenbosch University https://scholar.sun.ac.za

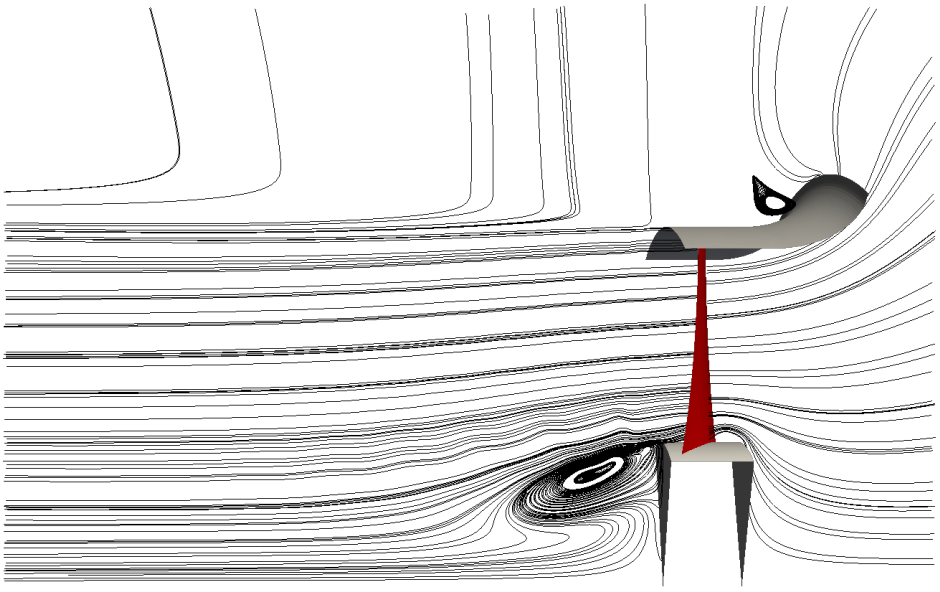

Figure F.14: Meridional streamlines of the square hub at $\dot{V} = 19\ \mathrm{m}^3/s$

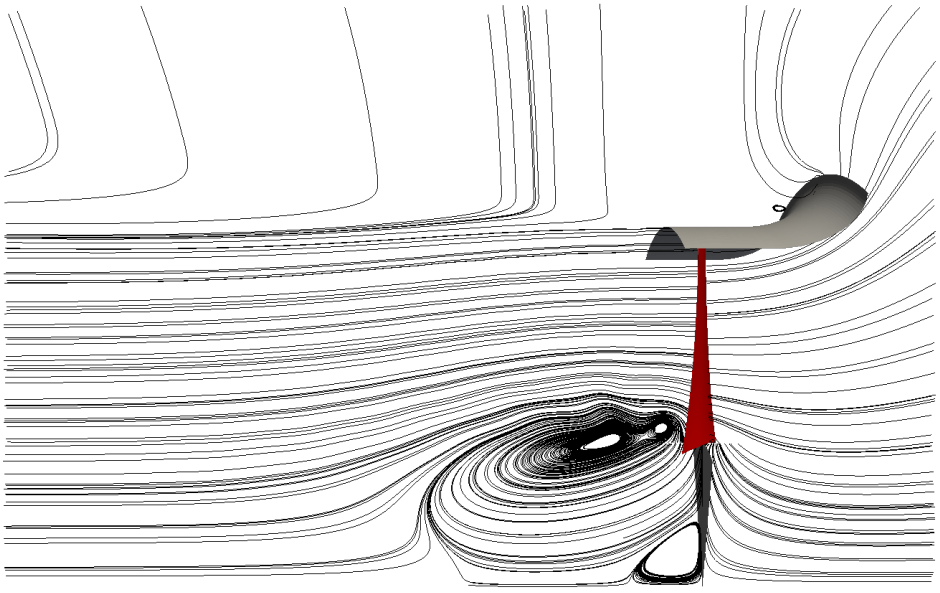

Figure F.15: Meridional streamlines of the centre disk hub at $\dot{V} = 19\ \mathrm{m}^3/s$

Stellenbosch University https://scholar.sun.ac.za

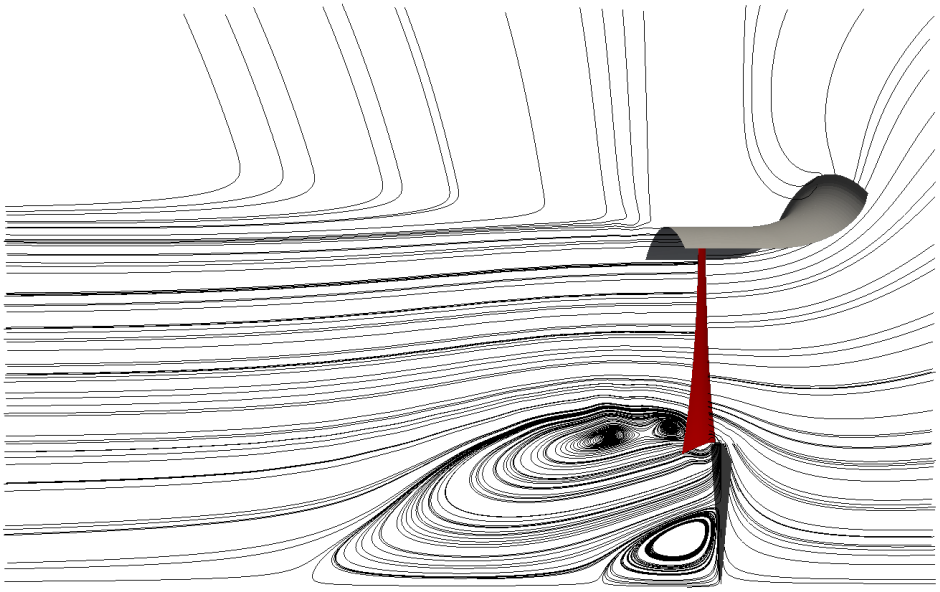

Figure F.16: Meridional streamlines of the forward disk hub at $\dot{V} = 19\ \mathrm{m}^3/s$